UNIVERSITY OF CALIFORNIA,
IRVINE

Designer plasmonic nantennas and coherent Raman scattering at their nanojunctions

DISSERTATION

submitted in partial satisfaction of the requirements
for the degree of

DOCTOR OF PHILOSOPHY

in Chemical and Materials Physics

by

John Houlihan

Dissertation Committee:
Professor Ara Apkarian, Chair
Professor Matt Law
Professor Craig Martens

2021

TABLE OF CONTENTS

LIST OF FIGURES

LIST OF TABLES

ACKNOWLEDGMENTS

I would first like to thank my advisor Professor V. Ara Apkarian for providing me the opportunity and support to develop as a scientist and optical engineer. The skill set I acquired while working in Professor Apkarian's lab has led to my successful transition to industry as a Biomedical Optics Engineer for a rapidly developing silicon photonics company. I also want to thank my committee members Professors Matt Law and Craig Martens for their guidance and advice throughout my studies.

I would like to give special thanks to the colleagues who were influential to my success. A small list includes: Dr. Mayukh Banik, Dr. Kevin Crampton, Dr. John Kenison, and William Harris.

Lastly, I want to acknowledge the support of the National Science Foundation funded Center for Chemistry at the Space-Time Limit (CaSTL) for providing the funding for my research (Award: CHE-1414466).

CURRICULUM VITAE

John Houlihan

EDUCATION

Doctor of Philosophy in Chemical and Materials Physics **2021**
University of California Irvine *Irvine, California*

Master of Science in Chemistry **2021**
University of California Irvine *Irvine, California*

Bachelor of Science in Chemistry **2014**
University of Oregon *Eugene, Oregon*

PROFESSIONAL APPOINTMENTS

Biomedical Optics Engineer **2021–Present**
Rockley Photonics *Irvine, California*

RESEARCH EXPERIENCE

Graduate Research Assistant **2015–2021**
University of California Irvine *Irvine, California*

Undergraduate Research Assistant **2013–2014**
University of Oregon *Eugene, Oregon*

TEACHING EXPERIENCE

Teaching Assistant **2014–2016**
University of California Irvine *Irvine, California*

ORAL PRESENTATIONS

Stimulated Raman Scattering at Plasmonic Nanojunctions using Continuous-Wave Lasers — **May 2019**
Chemistry at the Space-Time Limit

POSTER PRESENTATIONS

Coherent Raman Anti-Stokes Scattering at Plasmonic Nanojunctions — **January 2020**
Pacific Conference on Spectroscopy and Dynamics in San Diego

Stimulated Raman Scattering at Plasmonic Nanojunctions Using Continuous-Wave Lasers — **August 2019**
American Chemical Society National Meeting in San Diego

Controlled Nanomanipulation of Non-Degenerate Plasmon Pairs — **January 2019**
Pacific Conference on Spectroscopy and Dynamics in San Diego

Controlled Nanomanipulation of Non-Degenerate Plasmon Pairs — **June 2018**
CaSTL - NSC Second Annual Symposium at Lake Arrowhead, CA

Controlled Nanomanipulation Using a SEM in-situ Nanorobot — **June 2017**
CaSTL - NSC First Annual Symposium in Jyvaskyla, Finland

Metamolecules by Nanomanipulation — **April 2016**
CaSTL Annual Meeting at Santa Catalina Island, CA

AWARDS

Department of Energy SBIR/STTR Phase I Release 1, $\$256,380$ — **February 2021**
DOE SBIR/STTR Grant Award (Award Number: DE-SC0021604)

CaSTL Grant Contest Third Place, $\$1,000$ — **August 2018**
NSF Chemistry at the Space Time Limit

CaSTL Grant Contest First Place, $\$10,000$ **August 2016**
NSF Chemistry at the Space Time Limit

Organic Chemistry Achievement Award **June 2014**
University of Oregon

ABSTRACT OF THE DISSERTATION

Designer plasmonic nantennas and coherent Raman scattering at their nanojunctions

By

John Houlihan

Doctor of Philosophy in Chemical and Materials Physics

University of California, Irvine, 2021

Professor Ara Apkarian, Chair

Interactions between photons and plasmons have resulted in a hotbed of research activity in the physical sciences, notably through techniques such as white-light and Raman scattering, as evidenced by >10,000 articles published in 2020. In this work, plasmon-mediated linear white-light scattering and nonlinear spontaneous and coherent Raman scattering techniques are explored. In the first part of the thesis, I present studies of white-light scattering from nanostructures assembled using an in-situ scanning electron microscope (SEM)-compatible nano-manipulator robot. I discuss the challenges and derive the limitations of manipulating nano-sized objects using the nanorobot, and address geometry considerations related to white-light scattering from the nanostructures. In the second part of the thesis, I present studies of Raman scattering of bipyridyl ethylene (BPE) trapped at plasmonic nanojunctions, for historical reasons, known as surface-enhanced Raman scattering (SERS). We observe anomalously large anti-Stokes-to-Stokes scattering ratios accompanied by enhancement factors on the order of $10^{11} - 10^{12}$. We show that the effect does not arise from sequential Raman excitation; instead, it results from single-beam coherent anti-Stokes Raman scattering (CARS) where the Stokes plasmon acts as the intracavity stimulating field. I present conventional two-beam surface-enhanced CARS (SE-CARS) measurements on the same system using picosecond lasers, in both frequency and time-domain, and show that the single beam limit can be reached by attenuating the incident extracavity Stokes field.

Chapter 1

Nantenna assembly and white-light scattering spectroscopy

1.1 Successful operation of a SEM in-situ nanomanipulator device

Plasmonic nanostructures have received enormous attention through the years for their nano-scale antenna and sensor application using visible and near-infrared radiation [1–4]. The driving force of these applications is the collective oscillations of the conduction electrons at the metal-dielectric interface, more commonly known as surface plasmons [5, 6]. Fabrication of nanostructures wielding designer plasmonic response has been advanced in recent years through the application of sophisticated tools, such as electron beam lithography (EBL), focused ion beam milling (FIB), and scanning probe techniques to devise precise nanostructure arrays [7]. Among the targeted exciting applications are optical cloaking [8], negative refraction [9], and optical rectification [10].

Scanning probe techniques, such as atomic force microscopy (AFM), has been used to assemble artificial nanostructure building blocks [11]. By utilizing a sharp tip, which is controlled above a sample surface with sub-nanometer precision, plasmonic nanostructures with properties not available in natural materials can be assembled. An illustrative example of how plasmonic response can be controlled through nano-assembly is the manipulation of four gold particles into a nanoring exhibiting a magnetic based Fano resonance [12]. However, the application of a scanning probe technique for manipulating nanoscale objects with real-time visualization of the construction, has been limited.

In this chapter, I demonstrate the use of a commercial nanorobotic platform, the Kleindiek Prober Shuttle (PS8), to position nanometer-sized particles arbitrarily on a surface. By specializing to gold nanoparticles with 75 nm radius dry mounted on an indium tin oxide (ITO) substrate, I show controlled manipulation of individual particles to construct assemblies with nanometer precision in interparticle spacing. The success and limitations of such manipulations is dictated by the competing forces between the particle, tip, and ITO planar substrate, as expanded below.

A scanning electron microscope (SEM) compatible nanorobot manufactured by Kleindiek (Prober Shuttle, PS8) is implemented to manipulate and position nanoparticles with nanometric precision in order to tune their optical response. The nanorobot, which can be regarded as a scanning probe mechanical force manipulator, allows assembly of plasmonic structures by controlled manipulation of nanoparticles while visualizing the process in real-time by the SEM. The use of the nanorobot is illustrated by positioning $\sim$75 nm gold particles into arbitrary arrangements on a surface. The scattering spectra from sphere-triangle prism assemblies is then recorded using dark-field micro-spectroscopy and compared to results from FDTD simulations.

1.1.1 Optical characterization

The plasmonic response of individual nanoparticle assemblies is characterized through optical microscopy. To do so the assemblies must be spaced far enough apart to resolve optical signature from individual structures. The starting point is a planar substrate with well-dispersed units, with interparticle spacing convenient for the manipulations. With a combination of diffraction limited calculations and experimental trial and error, having nanostructures spaced apart by $4 - 6$ μm gives confidence that the optical signature comes from the desired nanostructure alone. We rely on wide-field darkfield microscopy and scattering spectroscopy to measure plasmonic resonances of the assembled nanostructures.

Figure 1.1 shows an effective spacing of nanostructures. The electron micrograph in Figure 1.1a, shows neighboring particles spaced $\sim$4 μm apart horizontally, and $\sim$6 μm apart vertically. The horizontal spacing is sufficient to isolate the targeted particles by closing the spectrometer slit, without sacrificing light collection efficiency from the particle under investigation. Figure 1.1b and 1.1c show the darkfield image gathered by the CCD with the spectrometer slited fully open and closed, respectively. The slit width is approximately 200 μm and the CCD images are recorded with the grating set at zero-order (acting as a mirror). With the grating set to first order, the dispersed light (spectra) of six vertically displaced particles is recorded simultaneously, Figure 1.1d.

To ensure particles are close enough together for swift manipulation but far enough apart for spectrally resolved individual particle spectra, the following protocol is used. ITO coated glass substrates are sonicated in acetone and isopropyl alcohol and dried with a stream of nitrogen gas to remove any impurities from the surface. Afterwards, the substrate is oxygen plasma cleaned at a base pressure of 1 mbar for 15 minutes to remove organic impurities and to provide a hydrophilic surface. A hydrophilic surface is needed because the aqueous particle solution needs to be adequately monodispersed on the surface. A hydrophobic surface

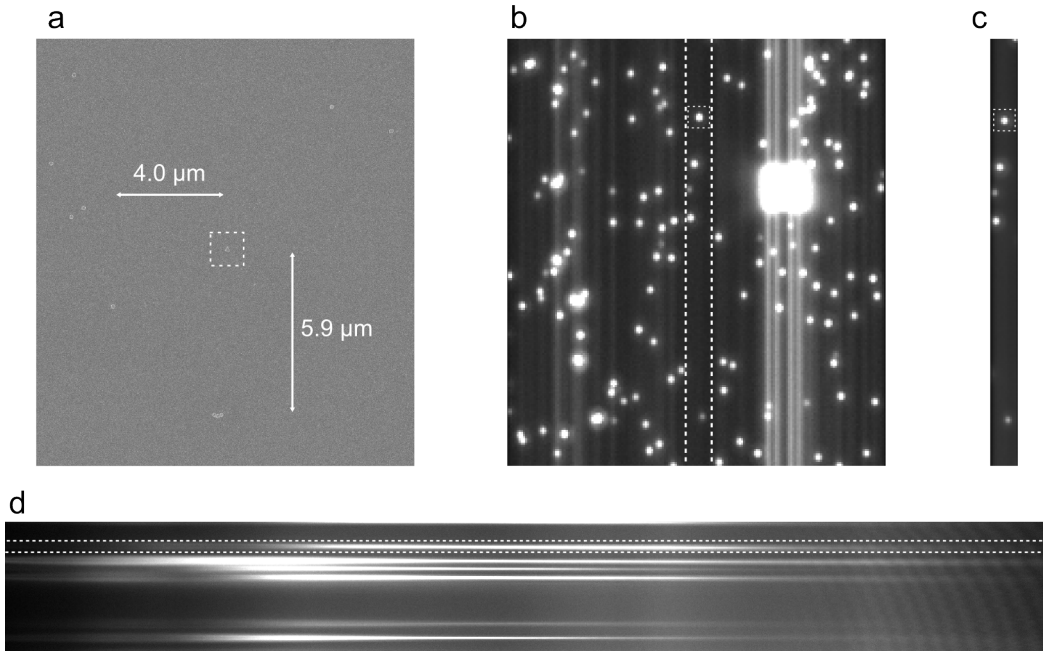

Figure 1.1: Optimal spacing for individual nanostructure scattering spectroscopy. a) Electron micrograph with the particle of interest bounded by a dashed square. b) Optical darkfield image recorded using the spectrometer CCD. The same particle of interest is bounded by a dashed square. Closing the spectrometer slit blocks the light from the unwanted particles. The dashed vertical lines delineate the image of the vertical slit. c) Image through the closed slit isolates the section bounded by the vertical lines in b. d) The dispersed image of the same section (c), with horizontal spectral axis. The spectrum of the targeted particle is obtained by integrating over the CCD pixels that lie between the dotted lines.

induces clumping of the nanoparticles, and most of the particles form a ring in the watermark left after evaporation of beading water. The particles are dispersed onto a substrate using a spin-coater and spun until dried. The sample is then placed in a vacuum container until nanomanipulation or optical characterization is required.

1.1.2 The Kleindiek nanoprobe station

Manipulation of micro- and nanoscale objects under real-time SEM visualization has received attention over the years [13, 14], but the devices required a dedicated SEM because of their substantial size. For nanomanipulation to become the standard fabrication technique, a device must be compact and portable so that one may use it in a community SEM. The Kleindiek Prober Shuttle (PS8), Figure 1.2a, is designed for such an application. The slim design of the PS8 allows it to be used with any commercial SEM. It is constructed with a non-magnetic materials, to allow its use in SEMs equipped with a magnetic immersion lens.

The PS8 is equipped with four probes capable of ∼10 nm up-and-down motion and better than 1 nm side-to-side motion. The manipulators and sub-stage also provide three in-plane translational degrees of freedom controlled with piezo-electric motors capable of 0.5 nm in-plane resolution. Manipulators accept both 0.25 and 0.5 mm wire, etched to form an ultra-sharp tip. The manipulators and sub-stage offer both fine and coarse motion allowing for fine tip positioning in a large field of view. The SEM chosen to accommodate the nanorobot is FEI's Magellan model with secondary electron imaging and a sample height clearance of 15 mm. The nanorobot is perfect for a SEM chamber with limited space, as the device is only 10 mm tall with a radius of 70 mm. The SEM is specified to have ∼0.5 nm resolution at 30 kV. In practice, manipulations are performed under frame rates of 10 Hz, and the real-time video resolution is limited to an imaging resolution of 2 nm. Several papers using the device for electrical characterization have been published [15, 16], but there have yet to

be any demonstrating nanomanipulation capabilities of the device. In this work, we employ the nanorobot for manipulation of gold nanoparticles using in-house, electrochemically etched tungsten tips [17].

The real-time visualization of the fabrication process gives the nanorobot significant advantage over AFM manipulation. It can be operated using both course and fine motion, allowing the user to assemble structures both rapidly and in a large region of interest. A second benefit of the system is there are no static structures, meaning the user can re-manipulate structures having already been manipulated before. This is a significant advantage to lithographic techniques, where the structure is determined by its template. The elimination of templates drastically reduces the fabrication time commitment, as designing a proper template requires a significant amount of time. Using the nanorobot, designer plasmonic antennas and sensors can be fabricated using nanoscale particles. Assemblies like linear and ring-shaped oligomers, as well as split-ring resonator type structures, can be fabricated with speed and high-controllability. It is also relatively easy to incorporate non-spherical particles such as triangular prisms, decahedrons, and nanocubes.

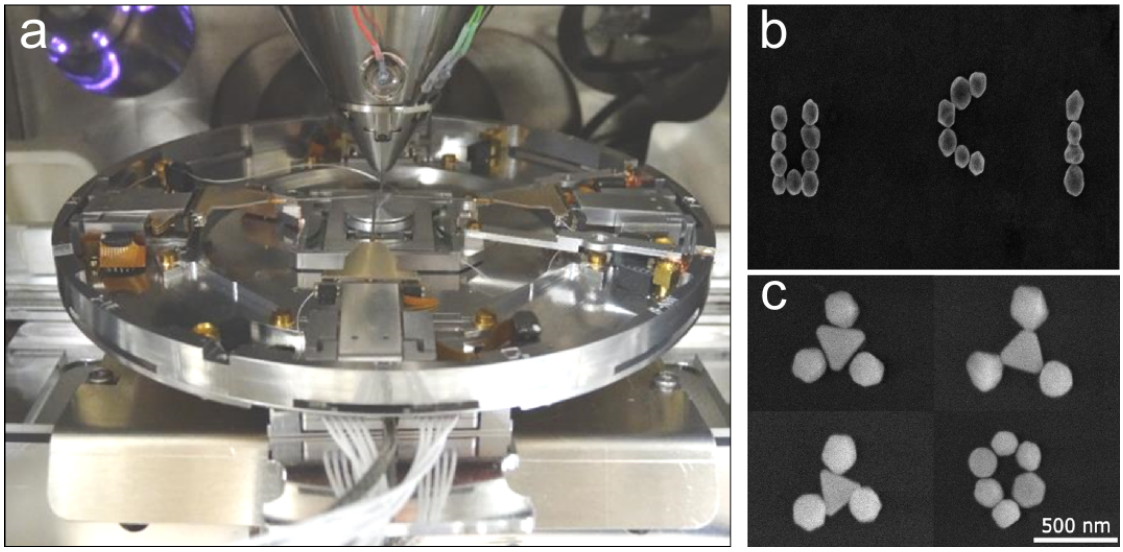

Figure 1.2: Kleindiek Nano Prober PS8 and nanostructures fabricated using the device. a) The PS8 nanorobot in a FEI Magellan SEM chamber. b) Fabricated UC Irvine logo, and c) complex nanostructures incorporating spheroids, triangular prisms, and decahedrons.

1.1.3 Practical considerations

To use the prober effectively, one must be aware of geometric considerations: the tungsten tip radius of curvature (ROC), cone angle, and angle of incidence with respect to the surface, as illustrated in Figure 1.3. The apex is the first part of the tip to touch the surface and it should not block the electron beam from striking the nanoparticle. The angle of incidence is limited by the clearance provided by the SEM pole piece. Figure 1.3a displays the manipulation geometry for an ideal tip to be used for nanomanipulation.

When either of the aforementioned parameters are out of the acceptable range, several issues arise leading to unsuccessful manipulations. First, you do not want the tip to be so large that it covers the nanoparticle you want to reposition, Figure1.3b. A tip with too large radius of curvature will cover the nanoparticle and will prevent the primary electrons from the beam to reach the nanoparticle. Secondly, the cone angle for the tip cannot be too large. The desire is to have the absolute apex of the tip to be the part that touches the surface. With a cone angle too large, the apex of the tip will not be the lowest part of the tip and will cover the particle rather than re-position it, Figure1.3c. Finally, the angle of incidence with respect to the surface for the tip is of great importance. Due to the small clearance provided by high resolution electron microscopes (EM), the tip cannot have too large an angle of incidence. This leads to the tip touching the substrate surface but the probe holder will be too high and will crash into the EM pole piece, Figure1.3d.

Durable sharp tips that can be easily etched, is essential for productivity. A sharp tip for manipulation is defined as a tip with a radius of curvature smaller than the particle radius being manipulated. A hard metal will also yield a tip durable enough to use multiple times. Lastly, the user needs a tip capable of being stored in atmospheric conditions. Tungsten provides these characteristics while also benefiting from a long shelf life. One tungsten tip can be used for multiple manipulations and only becomes unusable after it is crashed into the

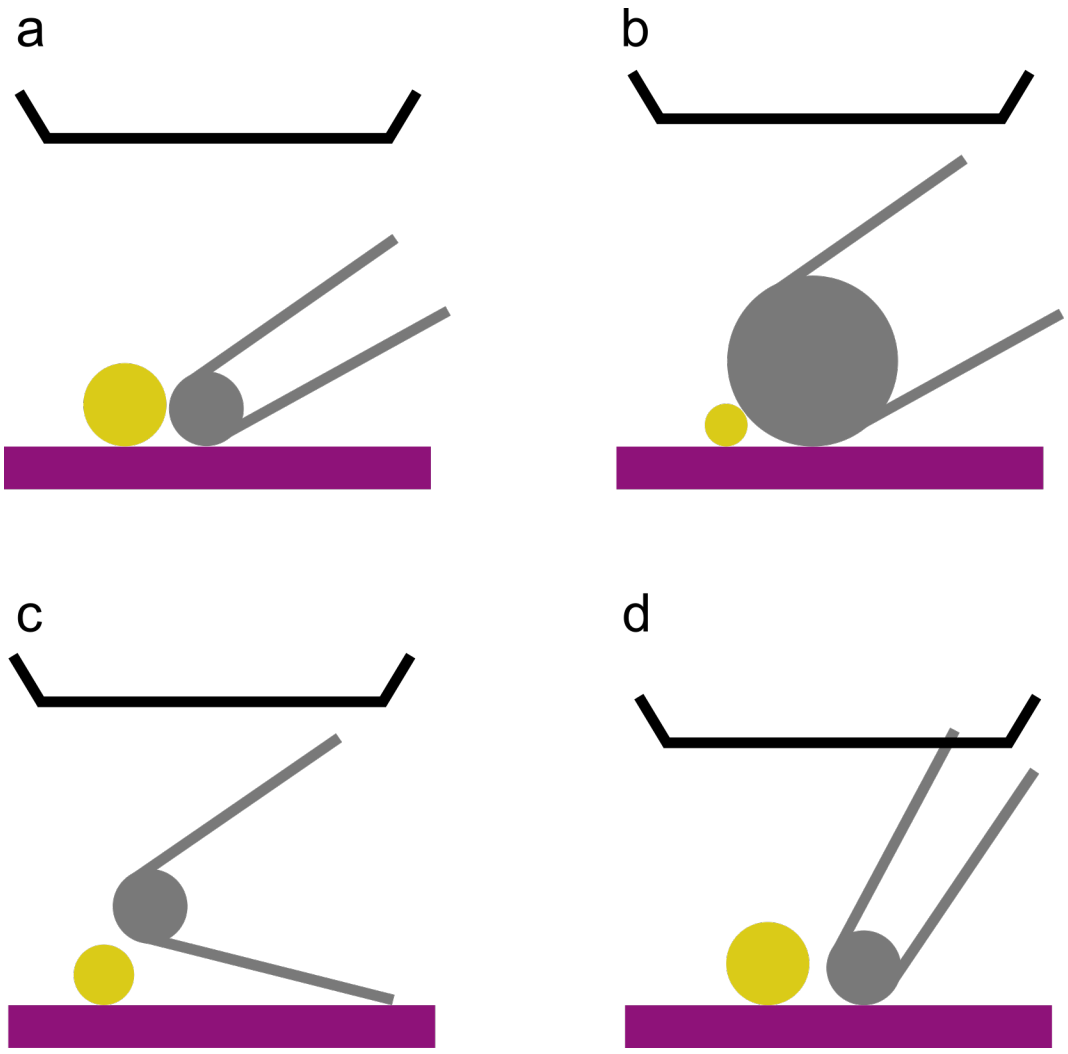

Figure 1.3: A cartoon showing examples of an ideal tip and problematic tips. a) An ideal tip to be used for nanomanipulation. The tip has a radius of curvature, cone angle, and angle of incidence for a successful manipulation. Examples of undesirable tips due to b) too large radius of curvature with respect to the particle's radius, c) too large of a cone angle keeping the apex from reaching the surface, and d) too large angle of incidence causing the probe to crash into the SEM pole piece.

surface. In between each manipulation the tip was kept at atmospheric conditions. Tungsten carries a native oxide layer which does not interfere with the manipulation considerations.

Tungsten wire is electrochemically etched by a two-step process using 0.9 M KOH as the etchant, allowing for reproducible tip apices sufficient for nanomanipulation. The first step involves static etching where tungsten wire, acting as one electrode, is suspended in the etchant surrounded by a platinum wire loop, acting as the counter electrode. A 15 V_{pp} alternating current (AC) field is applied to the two electrodes, and the tungsten wire is etched until bubbling ceases, providing the desired conical shape. The second step employs a fully automated closed loop laminar flow system to deliver the etchant to a moving platinum loop. A 5 V direct current (DC) bias is applied between the cathode (platinum loop) and the anode (tungsten wire), and a neck is formed from repeated passes of the platinum loop over the tungsten wire. The etching is disrupted, after the tungsten wire is decapitated, by removing the bias between the electrodes. Ultimately yielding tungsten tips with reproducible ROCs of $30 - 50$ nm.

The nanoparticle sample was kept in a vacuum when not actively in use, but spent time in atmospheric conditions when optical microscopy and spectroscopy experiments were performed. The same nanoparticle sample was also used over greater than a four month period. The cleanliness of sample and tip can be assessed by the absence of excess stiction, as long as the Hamaker forces are kept below the theoretical limits.

Gold nanoparticles work very well for nanomanipulation with tungsten tips, under the electron beam. Although a relatively soft metal, gold nanoparticles do not show obvious deformations under manipulation. To ease the manipulation process, the sample can be air plasma cleaned using the electron microscope. A benefit of gold is that its optical properties do not noticeably alter from the air plasma cleaning. Before and after scattering spectra of two gold nanoparticles were taken to show the air plasma cleaning did not adversely alter the dark field scattering spectrum, Figure 1.4. The observed variations in scattering intensity,

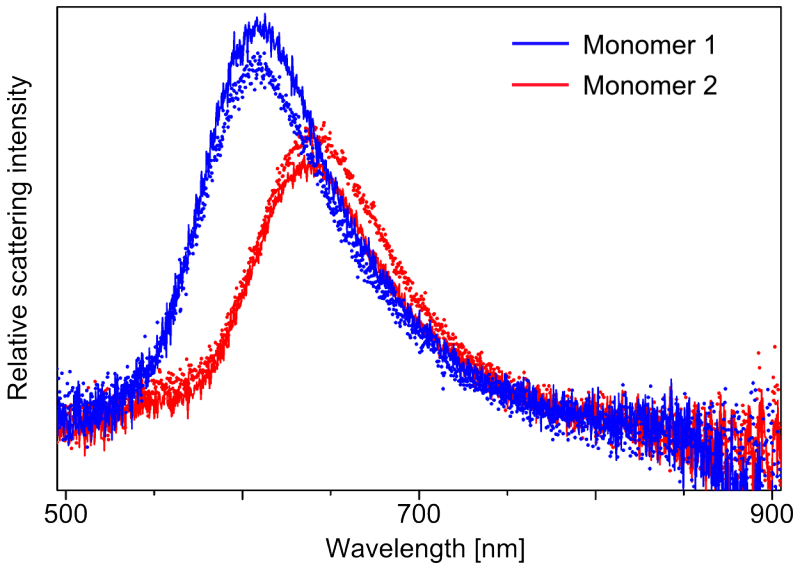

Figure 1.4: Experimental scattering spectra for two gold monomers before (solid lines) and after (discrete points) air plasma cleaning using the FEI Magellan SEM sample cleaning routine.

increase on some and decrease on others, is attributed to the limited reproducibility in the optical alignment in repeated measurements. The more important consideration is that the resonance maximum does not shift before and after plasma cleaning.

A large difficulty in nanomanipulation is sample drift. Popular ways to adhere SEM samples is by using double sided copper or carbon tape. These tapes do not securely adhere the sample to the SEM stub, leading to sample drift on the order of about 25 nm per minute. When working at large magnifications, the drift makes it difficult to accurately place a nanoparticle with respect to another. The solution to sample drift is to use colloidal carbon paste. If the carbon paste is allowed to dry for more than five hours, no sample drift is recognizable at magnifications of 500,000x. A securely adhered sample allows better image quality and lends to faster nanostructure fabrication.

Key to successful manipulation is safely landing the tungsten probe. Unlike AFM, there is no electrical or mechanical feedback preventing the tip from crashing into the surface. The feedback is provided to the operator by the real-time SEM images. A specific protocol is

implemented for the highest success rate of safely landing the tip to the surface. First, by focusing the electron beam at the surface the user can use the SEM software to determine its distance from the pole piece. The user can do the same by focusing onto the apex of the tip to determine its distance from the pole piece. From the two distance values, the user can calculate the distance between the apex and the surface. Second, the user can lower the tip a predetermined amount of course steps. After this is achieved, the distance between the pole piece and apex can be determined, and now the user has calibration between number of course steps and total distance traveled. Using this knowledge, the user can safely lower the tip close to the surface using the course motor. When the user is a couple microns from the surface, the fine motion piezoelectric motor should be used. If trying to land the tip using the course motor, the force exerted will be too great and will bend the tip upwards as it makes contact with the surface.

The next part of the landing protocol utilizes the fine motion from the piezoelectric motor. The main challenge to landing using the piezo motor is the limited range in motion offered by the piezo crystal. It is very rare to land the tip to the specific region of interest within the range provided by the piezo. To circumvent this issue, one can nearly land the tip by lowering it to a lower part of the sample. The user can tilt the sample slightly by gluing it to the SEM stub at one corner of the sample. After nearly landing at the lower part of the sample, the tip may be raised by extending the piezo motor to its top-most position. The sample may then be place back to the desired region of interest and the tip can be safely landed before reaching the bottom part of the piezo motion. Ideally, the piezo is at the mid-point of its total motion range and all of the manipulation can be performed quickly and efficiently.

To demonstrate the considerations, gold nanoparticles are arranged into a single file with inter-particle gaps that follow the Fibonacci sequence, Figure 1.5. A patch of gold particles randomly dispersed on the ITO surface is chosen for manipulation, Figure 1.5a and 1.5b; then seven chosen spheres are positioned one at a time to complete the Fibonacci sequence,

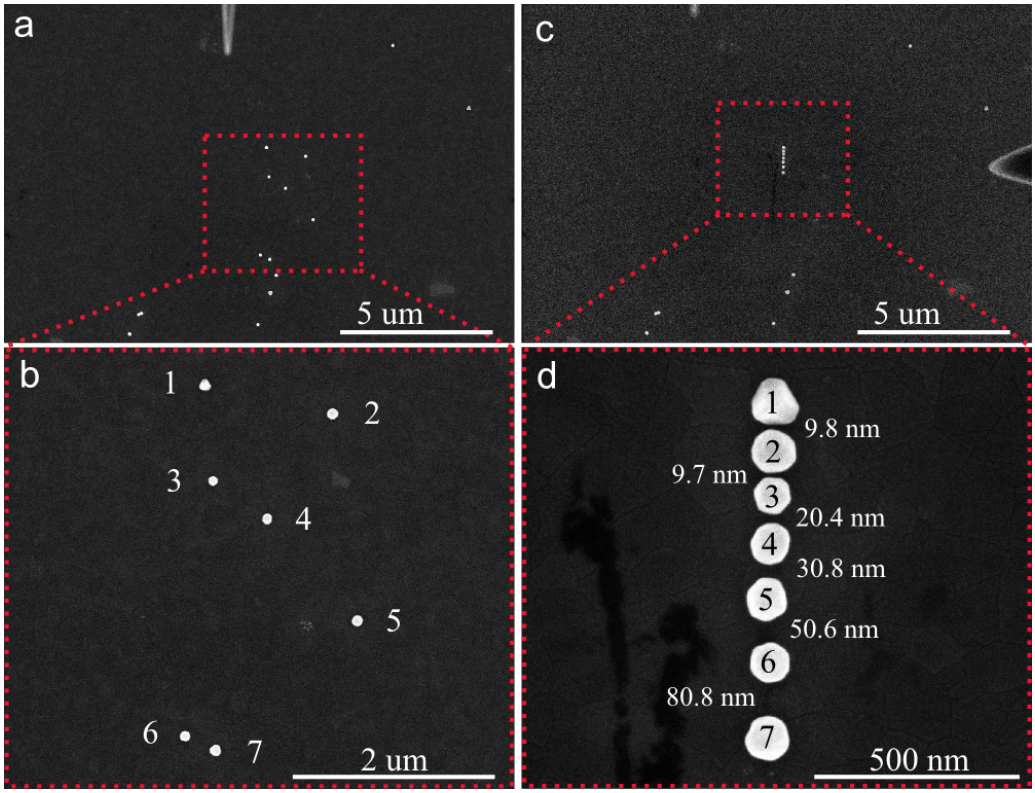

Figure 1.5: Controlled manipulation of gold nanoparticles into a Fibonacci sequence. a) Region of interest (ROI) before manipulation and b) a magnified picture with the particles of interest (POI) numbered. c) ROI after manipulation and d) the Fibonacci sequence with the POI numbered for comparison.

Figure 1.5c and 1.5d. The intent was for the first (smallest) gap to be 10 nm, and the six-gap sequence to terminate at 80 nm. The precise measurements after completing the arrangements are shown in Figure 1.5d. The errors in the gaps range from 1% to 3%, with a mean of 2%. More significant is the attainable absolute errors in placement, which can be seen in the smaller gaps to reach 0.2 nm, in agreement with the manufacturer's quoted resolution of 0.25 nm. Such control at large gap distances provides opportunities for assembling structures with tunable far-field radiation patterns, such as the Fibonnaci chain, which should act as a directional antennas and optical filters. The demonstrated precision in positioning of particle competes with the feature resolution attained in state-of-the-art techniques such as photolithography patterning, with the additional advantage of adjustability based on feedback, invaluable for prototyping.

In summary, an explanation and demonstration of a successful nanomanipulation has been discussed for the Kleindiek Prober Shuttle (PS8). The precision and accuracy were displayed by spacing gold nanoparticles into a pre-determined Fibonacci sequence using a tungsten tip. Controlled manipulation is essential for nanodevices, which are highly dependent on gap distance between component particles. A few technical issues to improve the success rate and accuracy for positioning gold nanoparticles were discussed. Included in the discussion is a productive protocol for landing the tungsten tip to the surface without damage. Also, the proper way to adhere the sample to the nanoprober stage using carbon paste was described. Using carbon paste eliminates sample drift on the time-scales needed for complete manipulation, while also maximizing the real-time image resolution allowing for more precise placement of the nanoparticle. Finally, an effective sample preparation was discussed for easy transition from manipulation into dark field scattering spectroscopy. By using the recommended nanoparticle solution concentration and substrate preparation, particles will be spaced close enough for quick manipulation and far enough for single nanostructure light scattering and spectroscopy.

1.2 Hamaker forces between a surface, tip, and nanoparticle

The nanomanipulation of particles is controlled by the competition of cohesive forces between particle-substrate and particle-tip interfaces. The study of nanoscopic interactions has a rich history, summarized in a prior micro-manipulation report [13]. They identify three sources of interaction between sub-macro systems. Two of the sources require an electric charge to be present, leading to electrostatic, Coulomb and Image forces. The third type of force is the close-range, attractive van der Waals force. Although the SEM in-situ nanomanipulation platform is grounded, insulating particles may develop charge, otherwise the dominant

interaction between neutral particles is due to van der Waals forces. Included in the van der Waals interaction is the Keesom-orientation, Debye-induction and London dispersion terms. The Keesom and Debye terms are due to dipole-dipole and dipole-induced dipole interactions, respectively. The requirement for these two forces is for the material to have a permanent dipole moment. Tungsten, gold, and ITO do not have net dipole moments, and the interactions between them can be described using London dispersion forces solely.

The dispersion force arises from an instantaneous dipole generated from the positions of the electrons with respect to the nucleus in an atom. Due to the polarizability of atoms, the instantaneous dipole induces a dipole in a neighboring atom leading to an attractive interaction between the two. The following relation was derived using quantum mechanical perturbation theory [18] to describe the interaction between dissimilar atoms,

$$U(r) = -\frac{1}{(4\pi\varepsilon_0)^2}\frac{3\alpha_{01}\alpha_{02}}{2r^6}\frac{h\nu_1\nu_2}{\nu_1+\nu_2} = -\frac{1}{(4\pi\varepsilon_0)^2}\frac{3\alpha_{01}\alpha_{02}}{2r^6}\frac{I_1 I_2}{I_1+I_2} \tag{1.1}$$

where $I_{1,2}$ are the first ionization energies of atoms 1 and 2. Equation 1.1 applies for atoms in vacuum; which in the following, will be corrected for interactions in a dielectric medium.

Hamaker described the van der Waals force between extended bodies by the pairwise sum of the van der Waals potential, to give expressions for the force between spheres and sphere and plane [19], ignoring the dielectric of the intervening medium. The geometries and expressions are given in Figure 1.6, where A is the Hamaker constant. In extended systems, the dielectric plays the role of polarization. For spheres of dielectric ε_1 and ε_2 separated by a medium of dielectric ε_3, McLachlan's generalized theory of van der Waals forces was developed. The theory includes the embedding material and the possibility of multiple absorption resonances. This was accomplished by replacing the atomic polarizability with the excess polarizability [20] which inherently incorporates the frequency dependent dielectric function for both the atom and medium. McLachlan's theory gives the following relation for the interaction potential

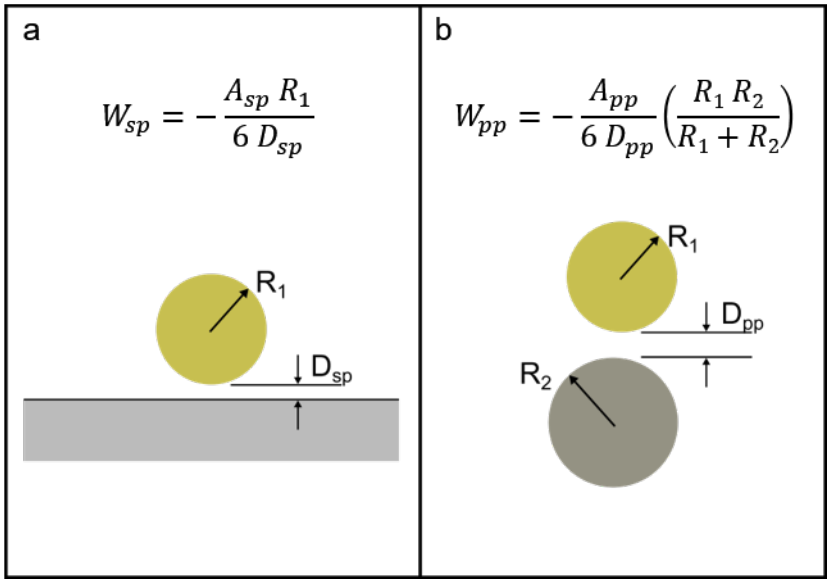

Figure 1.6: Potential for a) surface-particle (sp) and b) particle-particle interaction (pp). The potentials are dictated by the radii (R), gap spacing (D), and the Hamaker coefficient (A).

[21],

$$U(r) = -\frac{3a_1^3a_2^3}{r^6} * \left[kT\left(\frac{\varepsilon_1-\varepsilon_3}{\varepsilon_1+2\varepsilon_3}\right)\left(\frac{\varepsilon_2-\varepsilon_3}{\varepsilon_2+2\varepsilon_3}\right) + \frac{h}{\pi}\int_0^\infty \left(\frac{\varepsilon_1(i\nu)-\varepsilon_3(i\nu)}{\varepsilon_1(i\nu)+2\varepsilon_3(i\nu)}\right)\left(\frac{\varepsilon_2(i\nu)-\varepsilon_3(i\nu)}{\varepsilon_2(i\nu)+2\varepsilon_3(i\nu)}\right)d\nu\right] \tag{1.2}$$

where $a_{1,2}$ are the radii for small spherical interacting particles. The first term in the expression is the entropic, zero-frequency contribution of Keesom and Debye forces. The second term is the frequency dependent dispersion term.

A more rigorous quantum treatment of the same is given by the Lifshitz theory, allowing dispersion forces between macroscopic objects to be computed from their bulk dielectric properties and the geometry of the interacting system [22]. This leads to replacing the characterisitic Hamaker constant, used in the theory of van der Waals interactions between macroscopic bodies [19], by a frequency dependent Hamaker coefficient determined by the material dielectric properties, Equation 1.3. Generally, the Hamaker coefficient (A) is

expressed using,

$$A \approx \frac{3}{4}kT\left(\frac{\varepsilon_1-\varepsilon_3}{\varepsilon_1+\varepsilon_3}\right)\left(\frac{\varepsilon_2-\varepsilon_3}{\varepsilon_2+\varepsilon_3}\right)+\frac{3h}{4\pi}\int_{\xi_1}^{\infty}\left(\frac{\varepsilon_1(i\xi)-\varepsilon_3(i\xi)}{\varepsilon_1(i\xi)+\varepsilon_3(i\xi)}\right)\left(\frac{\varepsilon_2(i\xi)-\varepsilon_3(i\xi)}{\varepsilon_2(i\xi)+\varepsilon_3(i\xi)}\right)d\xi \quad (1.3)$$

One may notice the Hamaker coefficient, which carries units of energy, is the macroscopic analogy to McLachlan's theory for the interaction between atoms in a dielectric medium. Similar to McLachlan, the Hamaker coefficient is almost entirely determined by the frequency dependent dispersion term. From the geometry of the interacting system and the Hamaker coefficient, the attractive or repulsive force between macroscopic particles and surfaces can be calculated.

1.2.1 Preferential adhesion of a gold nanoparticle to an ITO surface

After a considerable amount of time using the nanorobot, two extreme regimes are realized for the manipulation of particles. Depending on the radius of curvature (ROC) for the tip, the particle of interest may preferentially stick to the ITO substrate or the tungsten tip. If the particle adhesion strength to the tip is greater than the substrate, then the particle may be picked up but not placed back on the substrate. If the adhesion of the particle to the substrate is greater, then the particle can be pushed to a desired location but cannot be picked up.

For now, the regime where the particle preferentially sticks to the surface rather than the tip is of interest. In this regime, the least amount of expertise and technique is required, as the operator can simply push particles into their desired position. This condition holds when the force attracting the gold nanosphere to the ITO surface is greater than the force attracting the nanosphere to the tungsten tip $F_{sp} \geq F_{pp}$. From the equations provided in Figure 1.6, when $D_{sp} = D_{pp}$ (gold nanosphere in contact with ITO and tungsten tip), a condition between the Hamaker coefficients and radii of the gold nanosphere (R_1) and tungsten tip (R_2) is obtained.

The gold particle will preferentially stick to the ITO surface, rather than the tungsten tip, if

$$R_2 \leq \frac{A_{sp}}{A_{pp} - A_{sp}} R_1 \tag{1.4}$$

Accordingly, the desired working regime can be predicted once one knows the values for the Hamaker coefficients A_{sp} and A_{pp}. To determine the Hamaker coefficients, Equation 1.3 is calculated for two distinct three media systems. The two distinct systems are gold interacting with ITO and gold interacting with tungsten and both systems are interacting across vacuum.

As mentioned, the chosen tungsten tip ROC is determined when we have solved for the desired Hamaker coefficients. To do so one may use the method of fitting to spectral data to extract the necessary parameters for determining $\varepsilon(i\xi)$ for all materials involved [23]. By the Lorentz model, any linear dielectric response can be described as the sum of damped harmonic oscillators in the form of,

$$\varepsilon(\omega) = 1 + \sum_j \frac{f_j}{\omega_j^2 - \omega^2 - i\omega g_j} \tag{1.5}$$

and when evaluated at imaginary frequencies ($\omega = i\xi$),

$$\varepsilon(i\xi) = 1 + \sum_j \frac{f_j}{\omega_j^2 + \xi^2 + g_j \xi} \tag{1.6}$$

where the summation term is the damped-oscillator form for a dielectric. When Equation 1.6 is determined for each material of interest, the Hamaker coefficient is calculated using Equation 1.3.

To determine f_j, ω_j, and g_j, the imaginary dielectric response from published experimental data is fitted to the following Lorentzian distribution,

$$\varepsilon''(\omega) = 2n(\omega)k(\omega) = \sum_j \frac{\omega g_j f_j}{\left(\omega_j^2 - \omega^2\right)^2 + \omega^2 g_j^2} \tag{1.7}$$

Table 1.1: Gold fitted parameter values using fitted experimental imaginary dielectric results.

resonance	f_j	g_j	w_j
1	31.2	1.28	3.94
2	13.8	1.64	7.32
3	807.7	29.7	11.6
4	44.7	2.24	19.8
5	30.9	2.79	29.0
6	76.3	12.7	39.4
7	495.8	40.1	63.1

Table 1.2: Tungsten fitted parameter values using fitted experimental imaginary dielectric results.

resonance	f_j	g_j	w_j
1	66.4	1.15	2.71
2	20.73	0.41	3.91
3	35.1	0.87	5.04
4	33.5	2.26	7.01
5	169.4	6.16	11.0
6	132.8	8.14	16.8
7	3.78	0.91	22.9

where $n(\omega)$ and $k(\omega)$ are the frequency dependent refractive index and extinction coefficient for the material of interest. The imaginary dielectric is calculated for both gold and tungsten using complex refractive index results derived from reflection electron energy-loss spectroscopy [24]. This set of experimental data was chosen because both gold and tungsten results were obtained from the same experimental apparatus. The set of data also offered the chance to fit the experimental results over the same frequency range for both metals. Figure 1.7 shows the experimental data (black dots) and resulting fit (red line) using a sum of Lorentzian functions, Equation 1.7.

The previous relations work well for materials with well reported complex refractive index results with resonances that can be fit. For materials, such as ITO, with no resonances in the reported dielectric results, an alternative approach must be taken. This approach results in using a simpler form for the dielectric response. For a dielectric medium, like ITO, with one

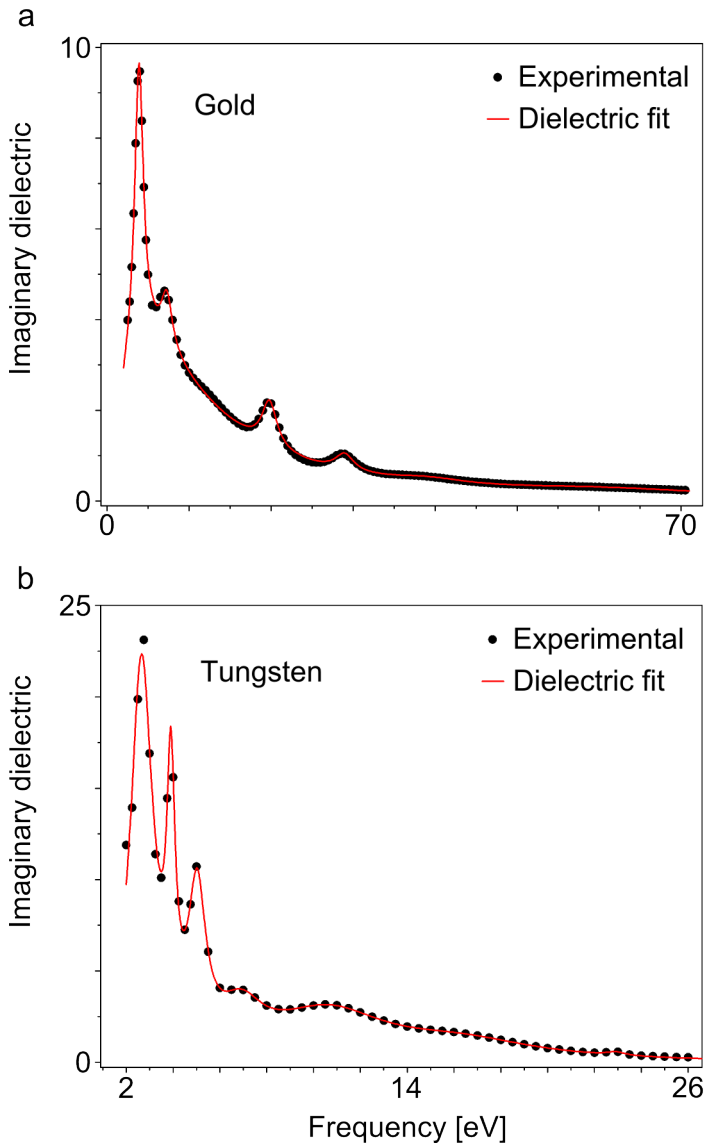

Figure 1.7: Imaginary dielectric experimental (black dots) and fit (red line) for a) gold and b) tungsten. The experimental imaginary dielectric for both gold and tungsten is calculated from complex refractive index results derived from electron energy-loss spectroscopy.

Interaction	Hamaker coefficient (zJ)
Gold/Gold	313
Gold/Tungsten	293
Gold/ITO	118

Table 1.3: Calculated values for the Hamaker coefficients A for the gold, tungsten, and ITO system. The calculation is performed considering three media interaction geometry. Two of the media are represented by the material in the left column. The third medium for each system is taken as vacuum.

strong electronic absorption peak at frequency ν_e, the dielectric permittivity at frequencies ν is described using [21],

$$\varepsilon(\nu) = 1 + \frac{n^2 - 1}{1 - (\nu/\nu_e)^2} \tag{1.8}$$

and when evaluated at imaginary frequencies,

$$\varepsilon(i\nu) = 1 + \frac{n^2 - 1}{1 + (\nu/\nu_e)^2} \tag{1.9}$$

The refractive index n is evaluated using values in the visible spectrum because electronic transitions occur in the UV and visible part of the electromagnetic spectrum. The refractive index value $n = 1.87$ is chosen from the average refractive index in the wavelength region of 400 to 700 nm [25] and ν_e is determined from the band gap for ITO and is 4.2 eV [26].

Once the fitted parameters are determined from Equation 1.7, they are inserted into Equation 1.6. After forming Equation 1.6 for the three media involved in the interaction, they are plugged into Equation 1.3 to find the Hamaker coeffcient for the interaction. Finally, from the Hamaker coefficient, the forces between two spheres and a sphere and planar surface can be calculated. There are three Hamaker coefficients needed to be calculated when modeling the nanomanipulation forces. The three coefficients are for gold-gold, gold-tungsten, and gold-ITO interactions. Using Equation 1.3, the calculated Hamaker coefficients are presented in Table 1.3. The Hamaker coefficient obtained for the gold-gold interaction calculated using its experimentally obtained dielectric data agrees well with previously reported values [23].

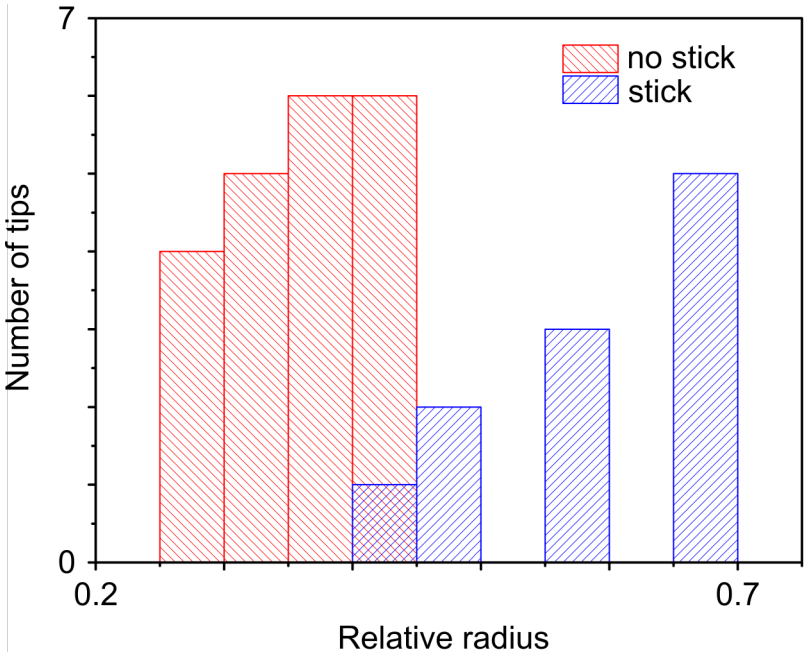

Figure 1.8: Histogram showing the relative radius r needed for the gold sphere to remain preferentially adhered to the ITO surface over the tungsten tip. The red bars (no stick) means the gold sphere remain adheres to the ITO surface and the blue bars (stick) means the gold sphere becomes adhered to the tungsten tip.

Now that the Hamaker coefficients are known for the system of interest, the tungsten tip ROC needed for preferential adhesion of the gold nanosphere to the ITO surface is determined. The Hamaker analysis leads to $R_2 < 1.5R_1$ as the condition for the nanosphere to preferentially adhere to the surface. The radius of the gold nanosphere is typically 75 nm meaning a tungsten tip with ROC less than 112 nm will prevent stiction between the particle and tip. This condition for the tungsten tip ROC is easily realized for the in-house tungsten tip electrochemical etching apparatus.

Equation 1.4 is rearranged to show at which experimental values of the ratio r preferential stiction of the gold nanosphere to tungsten tip occurs.

$$\frac{A_{sp}}{A_{pp}} \geq \frac{R_2}{R_1 + R_2} = r \tag{1.10}$$

Experimentally, a histogram for $R_2/(R_1 + R_2)$ (denoted r) versus tip-particle pair number is used to determine the working threshold. A soft threshold is observed for r ranging from 0.4-0.45. This range corresponds to the overlap between red and blue regions in Figure 1.8. The relationship provides the threshold radius of curvature (R_2) for a tungsten tip ensuring preferential stiction of the gold nanosphere to the ITO substrate over the tungsten tip. A small discrepancy exists between the experimental and computed thresholds. From the Hamaker analysis, one would expect a threshold at 0.40. This threshold value is determined from the ratio of Hamaker coefficients for the surface-particle ($A_{sp} = 118$ zJ) and the particle-particle ($A_{pp} = 293$ zJ) interactions, Table 1.3. A soft threshold is expected because the gold and tungsten particles are not spherical, but faceted. When a nanoparticle with a large facet interacts with the surface, the force between the two will be greater. This is because the large facet starts to mimic a surface rather than a sphere, and the interaction between two planar surfaces is greater than the interaction between a sphere and a planar surface.

1.2.2 Transferring a gold particle from the tip to a particle

An observation made is the ability to transfer a gold nanoparticle stuck to the tungsten tip to a second gold nanoparticle. This condition first arises when the force between the gold particle and tungsten tip is stronger than the force between the gold particle and the ITO substrate. The phenomena of transferring the particle is most commonly observed when using tungsten tips near the threshold radius for stiction. If the gold particle is brought into contact with a second particle using the tip, the particle transfers from the tip to the second particle. From these results, one may assume this is because a gold particle in contact with a second gold particle has a greater attraction than a gold particle in contact with a tungsten tip (i.e. a tungsten particle). To see if this is in-fact the case, a Hamaker analysis is performed. After performing the calculations, the results show the gold particle should remain adhered to the tungsten particle, mainly due to the larger size of the tungsten particle with respect to

Interaction	$R1/R2$	Hamaker force (nN)
Gold/Gold	75nm/75nm	-21.76
Gold/Tungsten	75nm/75nm	-20.41
Gold/Tungsten	75nm/90nm	-22.26

Table 1.4: Calculated values for the Hamaker forces gold-gold and gold-tungsten interactions. The third medium for each interaction is vacuum and the distance between spheres is taken as 0.3 nm.

gold particle. This result suggests the ITO surface plays a large part in transferring the gold particle to the second gold particle. A simple force analysis shows the combined force of the gold particle-particle and gold particle-ITO surface interactions dominate the gold-tungsten particle-particle interaction.

This effect can be rationalized using the previously mentioned Hamaker analysis. For the Hamaker analysis, contact is defined as a gap distance between particles of 0.3 nm. This is a well-known value for an approximate distance for a metal-metal bond. Using the relation from Figure 1.6b, the force between two spheres is calculated using $F_{pp} = -(\partial W_{pp}/\partial D_{pp})$ yielding,

$$F_{pp} = -\frac{A_{pp}}{6D_{pp}^2}\frac{R_1 R_2}{R_1 + R_2} \tag{1.11}$$

From the Hamaker coefficient A for a three media interaction, the forces for a gold-gold particle-particle interaction and a gold-tungsten particle-tip interaction can be calculated and used to explain why the gold particle transfers from the tip to a second particle. Using the Hamaker coefficients from Table 1.3 and Equation 1.11, the calculated interaction forces are displayed in Table 1.4. The initial calculations suggest at a tungsten tip ROC of 90 nm the force between gold and tungsten becomes greater than the force between gold and gold. Experimental observations show a gold particle can be transferred to a second gold particle using tungsten tips with ROCs larger than 90 nm. Considering this observation, the calculations need to be adapted to yield more experimentally accurate results.

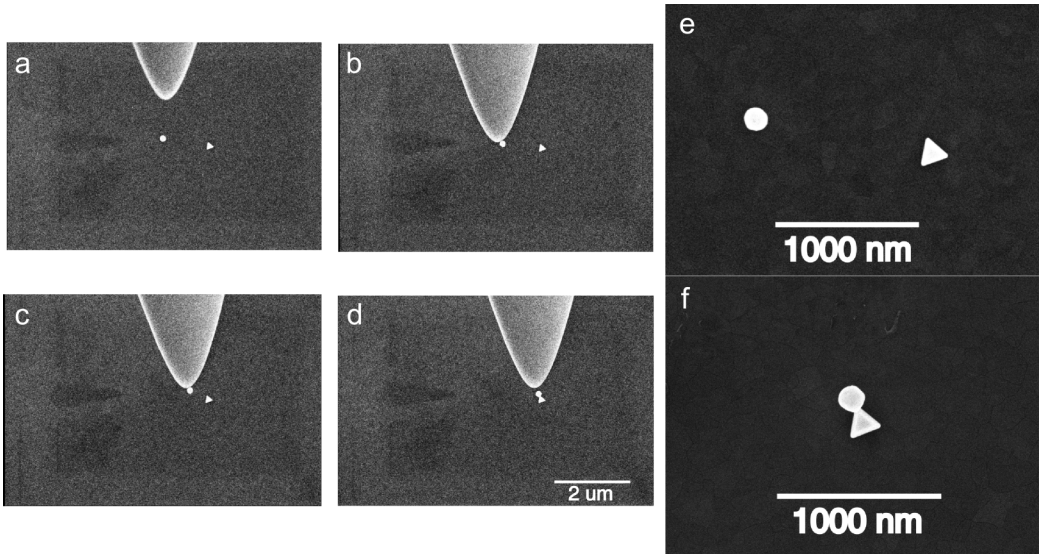

Figure 1.9: Using a tungsten tip to transfer an adhered gold nanosphere to a neighboring nanoprism. a-d) Sequential images showing the transfer of the nanosphere from the tip to the nanoprism. e) Before and f) after images of the nanoparticle pair.

Interaction	$R1/R2$	Hamaker force (nN)
Gold/Gold	75nm/75nm	-16.17
Gold/Tungsten	75nm/90nm	-14.88
Gold/Tungsten	75nm/110nm	-16.22

Table 1.5: Calculated values for the Hamaker forces gold-gold and gold-tungsten interactions using the adjusted distances between spheres.

From Equation 1.11, it is clear to see the calculated force is greatly influenced by the distance between particles D_{pp}. The adjusted distance between spheres is approximated using the sum of atomic radii for gold and tungsten. For the calculations, atomic radii of 1.74 Å and 1.93 Å are used for gold and tungsten, respectively [27]. The values for distance between spheres is now 0.348 nm and 0.367 nm for the gold-gold and gold-tungsten interactions, respectively. The updated Hamaker force values are displayed in Table 1.5. From the results, the gold-tungsten interaction starts to be greater than the gold-gold interaction for a tungsten particle of radius 110 nm.

1.2.3 Manipulating silica coated gold nanoparticles

Many plasmonically-enhanced Raman papers utilize silica coated gold nanoparticles because of their long-term stability [28–30], therefore attempts to manipulate the silica coated particles were made. The manipulation process introduces new complications not experienced when manipulating the bare gold nanoparticles. The phenomena observed was the near immediate stiction of silica coated particles to the tungsten tip. The Hamaker force analysis is performed for a similar system as compared to the previous system. The difference here is the replacement of a gold nanoparticle with a silica nanoparticle. A silica particle, rather than a silica coated gold particle, is used mainly for the ease of the calculation. This approximation to the actual system is justified due to the relatively large thickness of the silica coating compared to the distance between the silica sphere and tungsten tip. The thickness of the silica coating is approximately 40 nm while the distance between the silica and tungsten is less than one nm; therefore, the forces between tungsten and gold can be neglected.

In attempts to manipulate the silica-coated gold nanoparticles, a silicon wafer with a one micron thick layer of fused silica was used as the substrate. Using Equations 1.3 and 1.4, the expected tip radius for preferential stiction of the silica particles to the tungsten tip is calculated. Experimental observations show for small tungsten ROCs ($\sim 20 - 30$ nm), the silica coated particle sticks to the tip over the surface. To calculate the Hamaker coefficient for a system containing silica, Equations 1.8 and 1.9 are used by taking the average value for the refractive index for silica in the wavelength range of $405.5 - 705.6$ nm, n = 1.461 [31], and 9.3 eV is used for the bandgap [32]. From the Lifshitz analysis, a Hamaker coefficient ratio of 0.45 is calculated for the silica, tungsten, and ITO system. The ratio is determined from the surface-particle ($A_{sp} = 52.45$ zJ) and particle-particle ($A_{pp} = 115.78$ zJ) Hamaker coefficients, Table 1.6. The computed value is too small to be experimentally accurate and the system must be further analyzed to obtain a proper description of the system.

Interaction	Hamaker coefficient (zJ)
Silica/Tungsten	115.78
Silica/ITO	52.45
Silica/Silica	48.92

Table 1.6: Calculated values for the Hamaker coefficients (A) for the silica, tungsten, and ITO system. The calculation is performed considering three media interaction geometry. Two of the media are represented by the material in the left column. The third medium for each system is taken as vacuum.

1.2.4 Charge-induced dipole interaction of silica particles

Silica is an insulator, as such it can be expected to accumulate charge during imaging with the raster scanned focused electron beam. This is supported by the observation of repulsion between silica coated particle – it is possible to push one by another while maintaining a gap between them, and in some cases, the repulsion leads to a Coulomb explosion (am I right, or was it just snapping). Charge induced dipole forces can dominate over van der Waals forces, because of their softer dependence on distance. For a pair of atoms, the interaction potential is given as [21],

$$U(r) = -\frac{1}{(4\pi\varepsilon_0)^2}\frac{\alpha z^2 e^2}{2\varepsilon^2 r^4} \tag{1.12}$$

where z is the charge number, e is the charge of an electron, ε is the permittivity of the homogeneous medium in which the two atoms are embedded, and α is the polarizability of tungsten. Using $\varepsilon = n^2$, index $n = 1.461$ in the visible regime for silica [31], and the atomic polarizability (α) reported in Table 1.7, the induction and dispersion potentials are compared, Equations 1.12 and 1.1.

London's analysis also leads to an expression for the interaction potential between two dissimilar atoms, Equation 1.1. The two equations for the interaction potential between atoms only contains the attractive part. To calculate the potential, one needs to know the electronic polarizability of the atom (α_0) and first ionization potential (I) for each of the dissimilar atoms. The first ionization energy is the energy to remove one electron from the

Element	Atomic polarizability (10^{-24} cm^3)	Ionization energy (eV)
Gold	5.8	9.22
Tungsten	11.1	7.98
Silica	3.72	11.6

Table 1.7: Tabulated values from the CRC 80th edition handbook for the atomic and molecular polarizabilities. Tabulated values [33] for the ionization energies for use with calculating London dispersion forces. The ionization energy for silica is the value experimentally recorded for silicon monooxide [34].

atom of interest [33], or equivalently, the energy of an electron in the first Bohr radius, and is equal to the energy needed to ionize the atom [21]. At frequencies $\sim$1 THz, molecular dipoles do not respond fast enough to the electric field and the total polarizability (α) is equivalent to the electronic polarizability (α_0) [21]. UV, visible, and NIR frequencies ($200 - 800$ nm) range from about $375 - 1500$ THz.

Using Equations 1.12 and 1.1 and the values from Table 1.7, calculations can be performed to show the attractive force as a function of interaction type and spacing between particles. Figure 1.10 shows the comparison between the force curves for the two types of interactions. Clearly, the ion-induced dipole is stronger than the dispersion force at small distances. The comparison gives insight into why the silica-coated gold nanoparticle sticks to the tungsten tip more strongly than a bare gold nanoparticle. The ion-induced dipole attractive force is great enough that when the tungsten tip ROC is comparable to the silica-coated particle, the two are effectively guaranteed to adhere to one another. This contrasts with the two idealized particles interacting with one another purely through dispersion forces. This type of interaction is small enough that the interaction between the nanoparticle and surface is strong enough to compete with the force between the nanoparticle and tungsten tip.

A few remarks should be made about the ion-induced model to describe the silica-gold ion-particle interaction. First, it is assumed the interaction between a charge and neutral silica particle with the ITO surface is constant for both cases. This is not a theoretically proper assumption to make but experimentally evidence suggests the silica-coated gold and

bare gold particles are interacting with the ITO surface with similar force magnitude. This statement is made because it is not obvious the silica-coated particle is adhered more strongly to the surface than the bare particle during the manipulation process. During manipulation, by SEM imaging, it seems the force exerted by the mechanical driven tip to displace the particle is not any greater for the coated or bare particle. As a contrast, an attempt to displace the silica-coated gold particle while adhered to a silicon nitride surface resulted in a failure to move the particle from its position. During manipulation it is clear a larger force was applied to the coated particle by the tungsten tip but the particle was not uprooted from its location. The force applied becomes so great the tungsten tip slips from the coated particle with the particle remaining in its site.

Regarding the distance dependence of the dispersion ($1/r^7$) and induction force ($1/r^5$), there is a distance where the two intersect. Figure 1.10 shows the two interaction types assuming a charge of $z = 1$. Shown in the graph, the two curves cross near $r_c = 0.5$ nm. It is easy to see that the cross point (r_c) is inversely proportional to the charge, $r_c \propto 1/z$, as such, r_c becomes subatomic for $z > 2$, therefore the induction force dominates at all distances. The silica particles with dimensions of $\sim$100 nm, can accommodate many charges. As such, once charged, their interaction with the tip will be dominated by the Coulombic attraction between the effective charge on silica and its image in the metallic tip. In this regard, the force between charged particle and substrate becomes a critical consideration. If the substrate is conductive, as in ITO, then the magnitude of the image charge is determined by the dielectric. If insulating, then it can develop counter charge and immobilize the charged silica particle through the screened Coulomb potential between the charges across the particle-substrate interface. Indeed, these two behaviors are observed for silica on ITO versus silicon nitride.

A couple remarks can be said about this change in interaction strength. First, the distance between the charged silica sphere and tungsten tip when in contact is approximately 0.6 nm or more. Second, if the contact distance is a more expected value, about 0.3 nm, then the

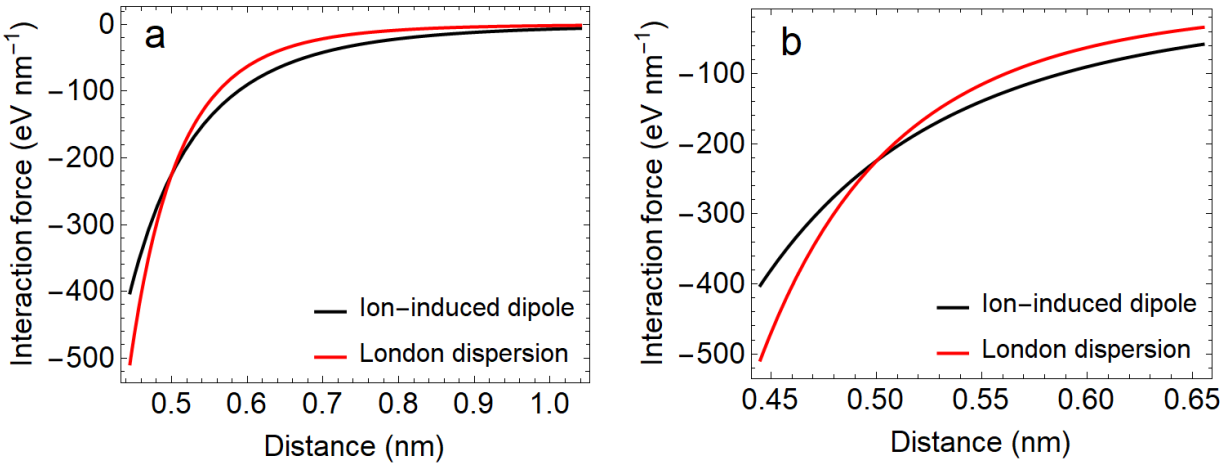

Figure 1.10: Force curves for silica and gold particles interacting by ion-induced dipole or London dispersion forces. For the ion-induced dipole interaction, the silica particle is assumed to have a charge $z = 1$.

charge on the silica sphere is greater than $z = 1$. Overall, it is expected the interaction type between the silica-coated gold nanoparticle and tungsten tip is more accurate described by an ion-induced dipole interaction. For this reason, more nanomanipulation was performed using the bare gold nanoparticles rather than the coated ones.

In summary, the predominant interactions at play during nanomanipulation while the sample is illuminated with an electron beam are either London dispersion or ion-induced dipole forces. The interaction type is dependent on the conductivity of the particles under consideration. For conductive particles, the interaction between the grounded substrate and tungsten tip is a result of competing, instantaneous attractive forces between the particle, tip, and substrate. The system is modeled using a Hamaker force analysis where the particle and tip are described as interacting spheres of dissimilar radii and the substrate is depicted as an infinite plane. Experimental observations such as conductive particles adhering to tips and fastened particles being transferred to neighboring particles is understood through the analysis. The Hamaker force helps shed insight into the interactions as work during the manipulation of conductive nanoparticles.

For conductive particles coated with an insulative material, dispersion forces alone do not accurately model the observed interactions. Due to the insulating layer, the primary electrons from the microscope's electron gun accumulate on the surface causing the particle to become charged. The electric field from the charge induces a dipole in the conductive tungsten tip leading to a stronger interaction when compared to pure dispersion forces. Clarifying the varying interactions observed during nanomanipulation will aids in the understanding of the nanoworld. This understanding will be of great consequence in the fields of nanocircuitry and optical metamaterials.

1.3 Controllable manipulation of gold nanoparticles

1.3.1 Dark field micro-spectrometer

Scattering spectra from plasmonic nanostructures are imaged and characterized using a home built dark field micro-spectrometer. An upright microscope (Zeiss Axioskop) coupled to a spectrometer (Princeton Instruments SP150) and back-illuminated EMCCD (ProEM eXcelon3) in a reflection geometry is used to record scattering spectra. Using unpolarized white light from a 100 W tungsten halogen lamp to illuminate the sample. The scattered light can be collected with or without a broadband polarizer as an analyzer. Scanning electron micrographs are taken using a SEM (FEI Magellan 400 XHR) for comparison to dark field images to ensure accurate spectroscopic characterization of fabricated structures.

The FDTD simulations were done by using a commercial software (Lumerical FDTD solutions). The total-field scattered field (TFSF) source was employed in the simulations of all the geometries and the plane wave was injected normally from the top of the nanostructures. A detector was placed outside the TFSF source to measure the scattering cross sections and a

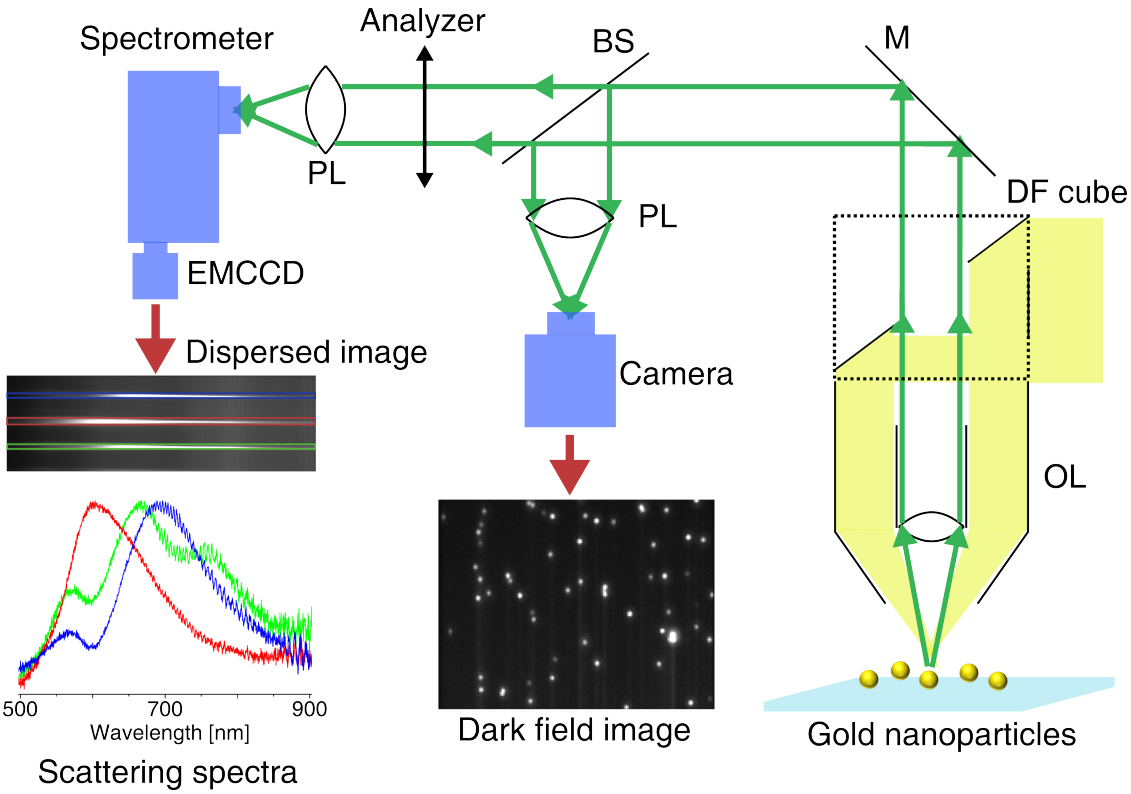

Figure 1.11: Dark field spectro-microscopy for measuring the plasmon resonance of individual particles and small clusters. Incident radiation (yellow) is focused at oblique angles using a dark-field (DF) reflector cube and DF objective (OL). Scattering radiation (green) is collected and focused into a spectrometer using a positive lens (PL), with the dispersed image/spectrum being collected using a CCD. The system also offers polarization-resolved detection by placing a polarizer in the collection path.

perfectly matched layer (PML) was used as the boundaries to absorb the scattered light and reduce the probable interference with the reflected light off the boundaries.

Starting at the turn of the century, single metallic nanoparticle scattering spectroscopy has received enormous attention for its ability to probe the localized surface plasmon (LSP) resonance of the particle [35–37]. In this work, we employ an upright microscope with dark field (DF) optics, and a tungsten halogen lamp, for the excitation of the localized surface plasmon resonance (LSPR) for gold. Projecting the image plane of the microscope onto the slit of a high throughput spectrometer allows for the detection of the LSPR, with the signal being detected by a charge-coupled device (CCD) detector. Altogether, a spectral

range of ∼500 nm can be detected at exposure times of around one second. Collecting scattered light from individual particles is simplified by superimposing DF images onto high-resolution SEM images, ensuring signal from the particle of interest is the only light passing through the spectrometer slit. We have implemented ex-situ dark field (DF) micro-spectroscopy to characterize the scattering spectra of the assembled structures for comparison with simulations. We employ an epi-illuminated geometry with a DF objective and a tungsten halogen (W-halogen) lamp as the light source.

1.3.2 Coupling a sphere to a triangular prism

To highlight the strength of the nanomanipulator we perform a gap dependent study on a sphere coupled to a triangular prism. This study will show the ability of the nanomanipulator to position nanoparticle to within 2 nm with 1 nm steps with high accuracy and precision. Secondly, we show how one can model nano-assemblies using finite-difference time-domain simulations to reproduce the experimental results. Transpiring from the comparisons, is that subtle structural details control the optical response of plasmonic junctions.

Using the nanomanipulator, it is possible to accurately place a sphere next to a triangular prism in a coupling regime with 1 nm increments to a gap spacing of 2 nm, Figure 1.12. To facilitate the study, several pairs of particles are used. This provides the ability to show how particles of different size and shape can change the scattering spectrum. To anticipate the resulting scattering spectrum for the coupled pairs, we performed finite-difference time-domain (FDTD) simulations using Lumerical. We start by modeling the pair using an ideal sphere and triangular prism with rounded vertices, Figure 1.13, emulating the shape seen in the top-down view of the SEM images.

Both the experimental and simulated scattering spectra show two plasmon resonances for both long axis and short axis detection, Figure 1.14. The two resonances can be assigned

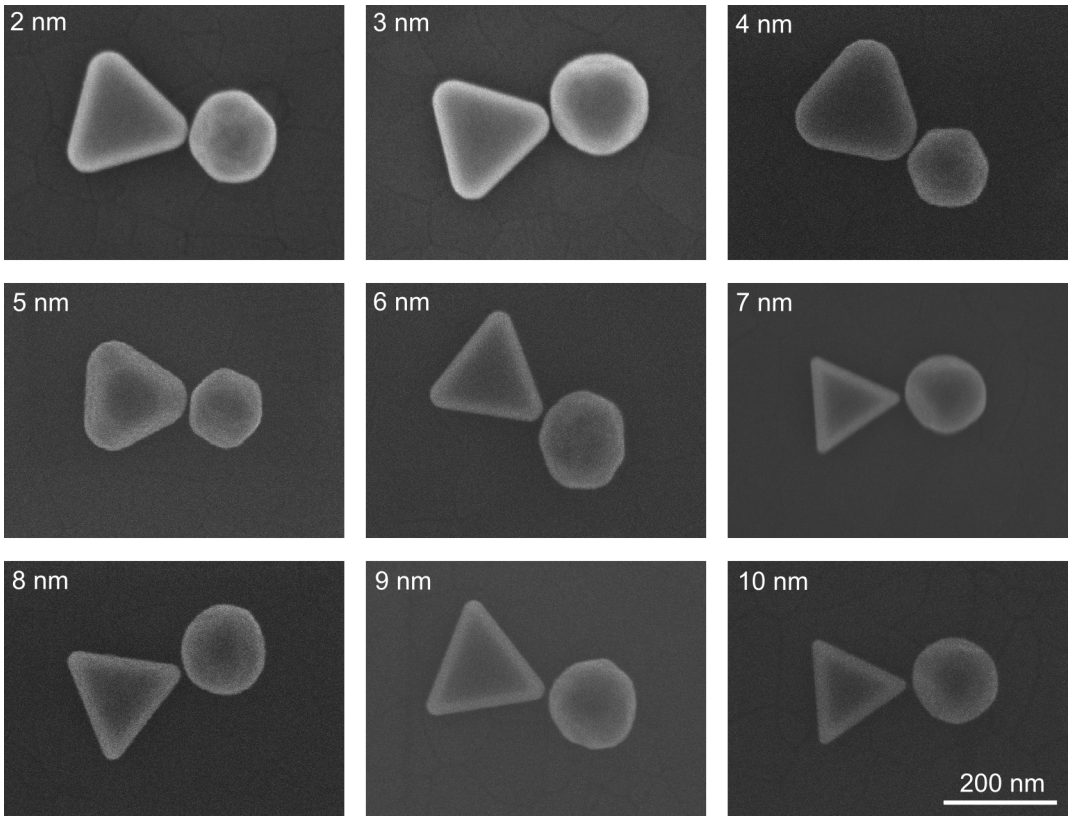

Figure 1.12: Controlled manipulation of TPS pairs with edge-to-edge distances ranging from 2 to 10 nm. The scale bar on the bottom right image is for all images. The figure shows the nanomanipulator's accuracy to place particles to gap sizes as small as can be resolved by the electron microscope.

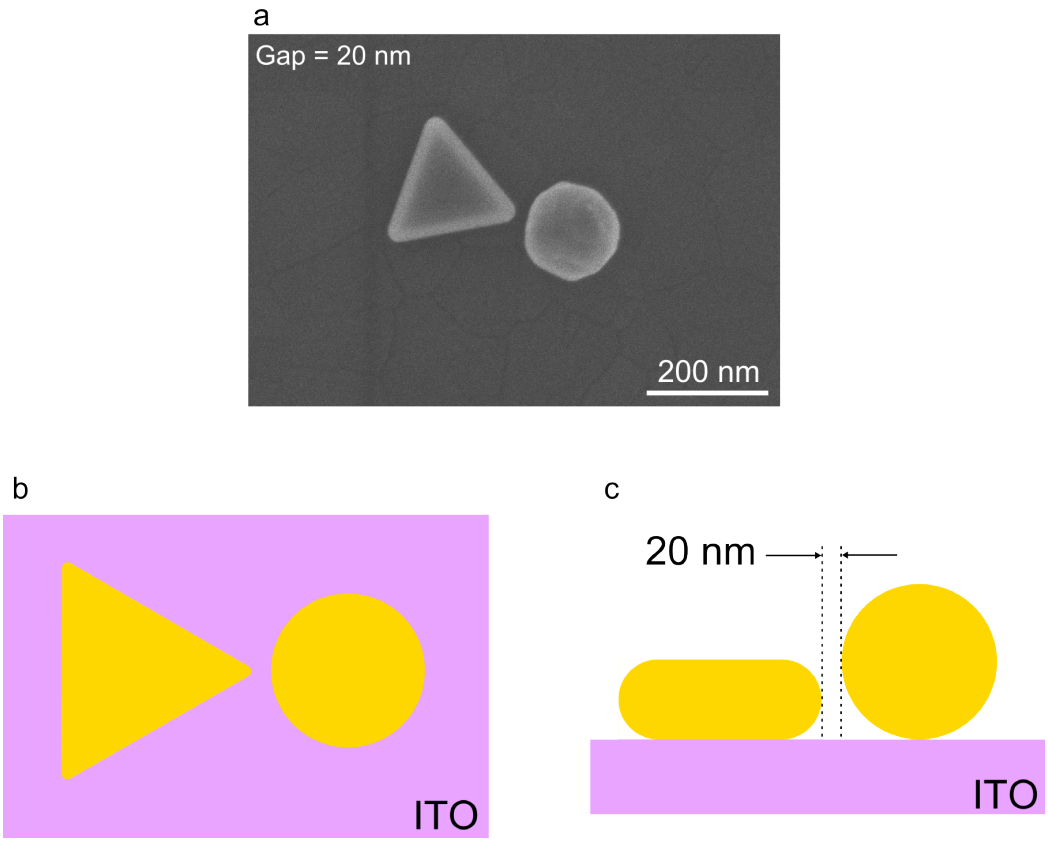

Figure 1.13: Image and cartoons highlighting the geometry used for the FDTD simulations. a) High resolution SEM image of the TPS pair with an edge-to-edge gap distance of 20 nm. b) A cartoon showing a top-down view for the object simulated using FDTD and c) a side-view cartoon showing the same pair. The FDTD simulation approximates the pair as a perfect sphere and a triangular prsim with sharp edges and vertices with a fixed radius of curvature determined from the SEM image.

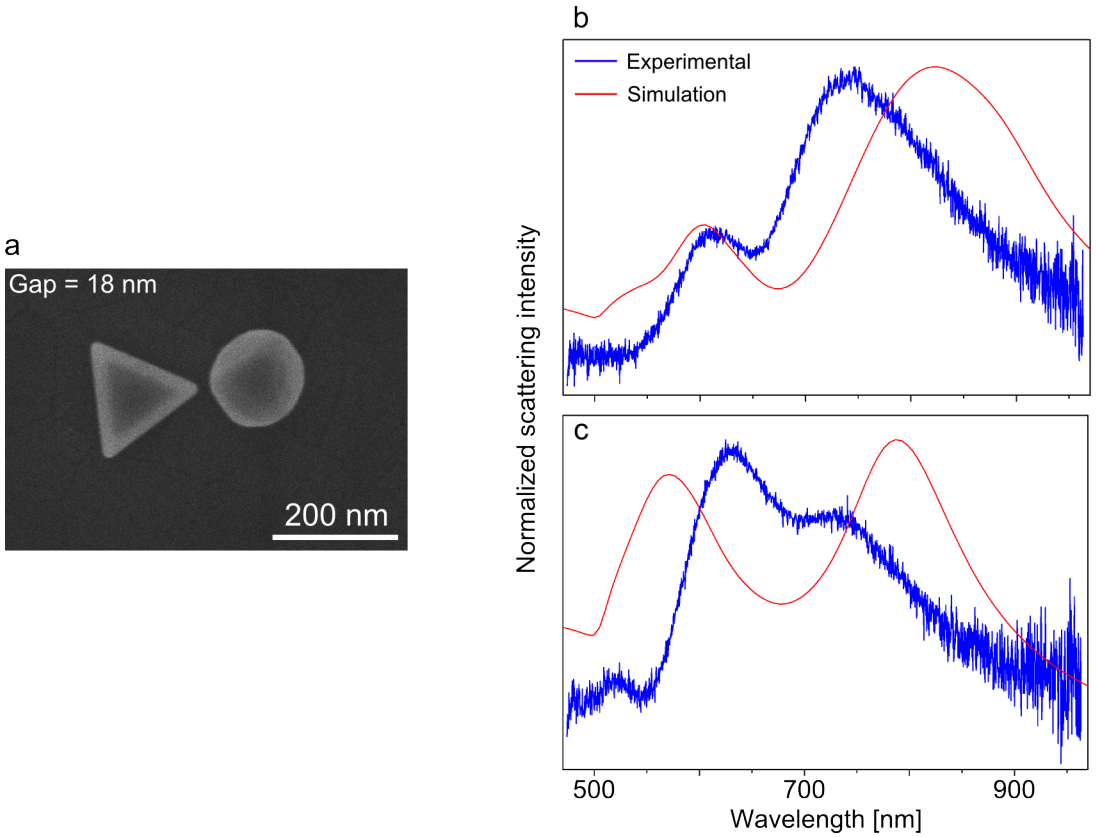

Figure 1.14: Long and short axis experimental scattering spectra (blue) and FDTD scattering cross section simulations (red) for a coupled triangular prism-shere (TPS) particle pair. a) High resolution SEM image of the TPS pair with an edge-to-edge gap distance of 18 nm. b) Experimental versus simulation scattering spectra along the long axis of the TPS pair and c) the same spectra along the pair's short axis.

to the asymmetric and symmetric coupled modes of the triangle-sphere pair, in accordance with several studies on coupled plasmonic particles [38–40]. We note the appearance of two plasmon modes when observing the short axis scattering spectrum. The second plasmon mode near 800 nm is present, where it would not show for a two-sphere system. The mode is present for the degenerate dipole system because the interacting dipoles still retain a net dipole moment.

Measurements and simulations are carried out by varying the junction gap. The general trends of the simulation match the experimental observations. For the long axis detection, as the gap is made smaller, both plasmon modes red shift. Much like the two-sphere case, as

the gap size shrinks the symmetric mode energy shift is greater than the asymmetric mode. This is due to the strong coupling and formation of a gap plasmon mode for the long axis. For the short axis, the modes also shift but with less energy shift than the long axis. This is because the plasmon modes do not strongly couple and no gap plasmon is formed.

Aside from the qualitative agreement between the experiment and simulation, there are discrepancies in the quantitative reproduction of the plasmonic resonances. The predicted asymmetric mode is higher in energy than in the experiment. A consideration, motivated by the SEM images, is to incorporate a larger interaction area between the sphere and substrate. This is done by considering the bottom of the sphere to be faceted rather than perfectly round. As can be seen in Figure 1.15, the dipolar resonance of the sphere red shifts as the contact area with the substrate is increased. Also, the edges of real triangular prisms are beveled, as can be seen in the top-down SEM images. The simulations illustrated in Figure 1.16 show that beveling of the edges leads to a blue shift in the dominant dipolar resonance.

Edges of real prisms are beveled, as can be seen by the contrast switching in the top-down images. The top and bottom bevel on the edges need not be symmetric, and they make different contributions to the resonance. Simulations are performed for a TPS pair consisting of a beveled prism and a flat-bottomed sphere, for the three different bevel geometries illustrated in Figure 1.17. The lower, middle, and upper bevels in Figure 1.17 are at distances of 25, 40, and 55 nm from the ITO surface, respectively, and the simulated triangular prism has a total height of 80 nm. From the simulations, a significant shift in the dipole resonance when excited along the long axis is observed, Figure 1.17b. As the bevel height increases (i.e. as the bevel is made further from the ITO surface) a blue shift in the dipole resonance is observed.

When looking at the cross-sectional view for the prism, it is apparent that the bevel has a radius of curvature (ROC), Figure 1.18a. This curvature will be called the bevel ROC. For the TPS pair excited along the long axis, a significant shift in the dipole plasmon resonance

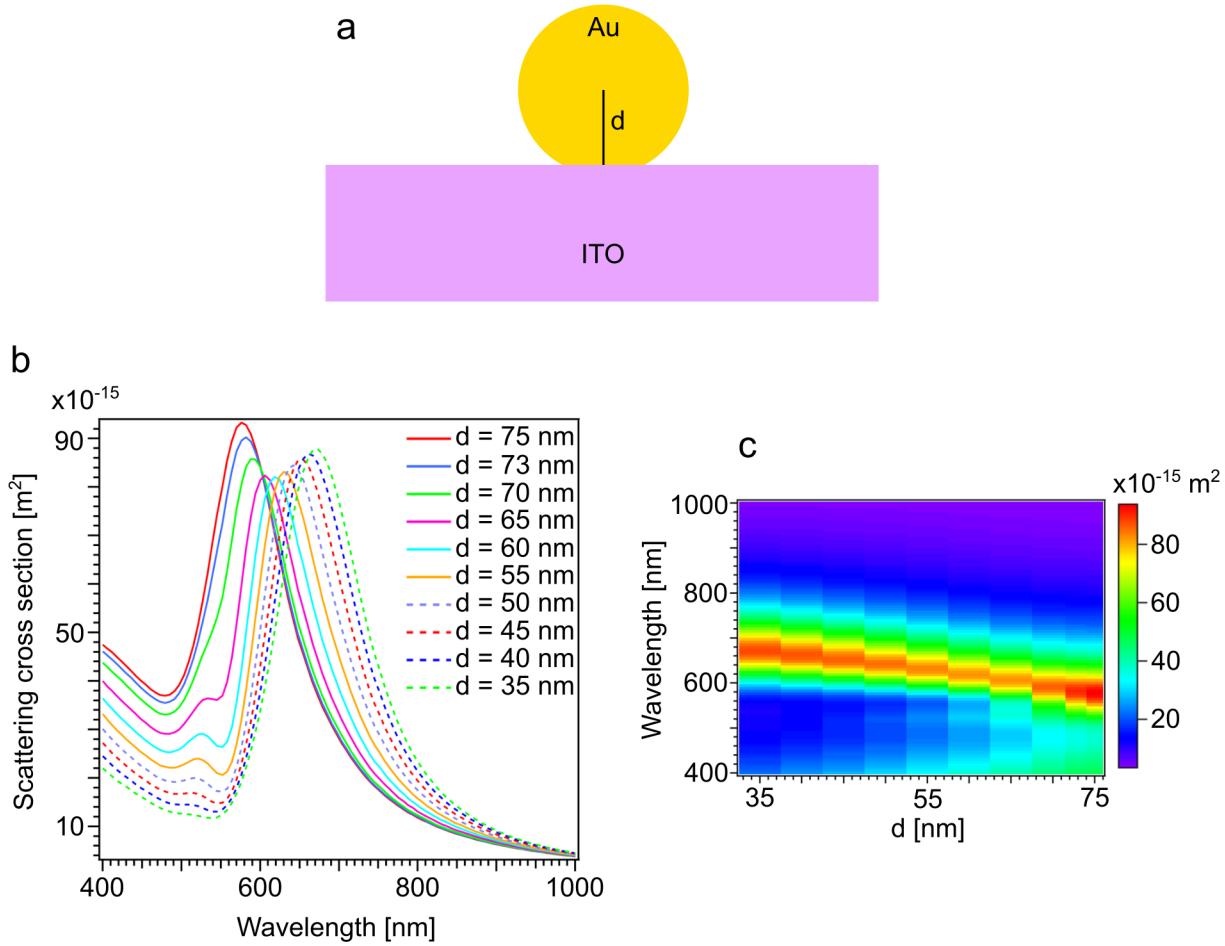

Figure 1.15: Scattering cross section plasmon shift for a bottom faceted gold sphere on an ITO surface. a) Cartoon for a bottom faceted gold sphere on an ITO surface. d is the distance from the center of the sphere to the ITO surface. b) Scattering cross section spectrum showing a red-shift in the plasmon resonance as d becomes smaller. This corresponds to the bottom facet becoming larger meaning more of the sphere is making contact with the ITO surface. c) Image plot showing the red-shifted plasmon resonance as the bottom facet is made longer.

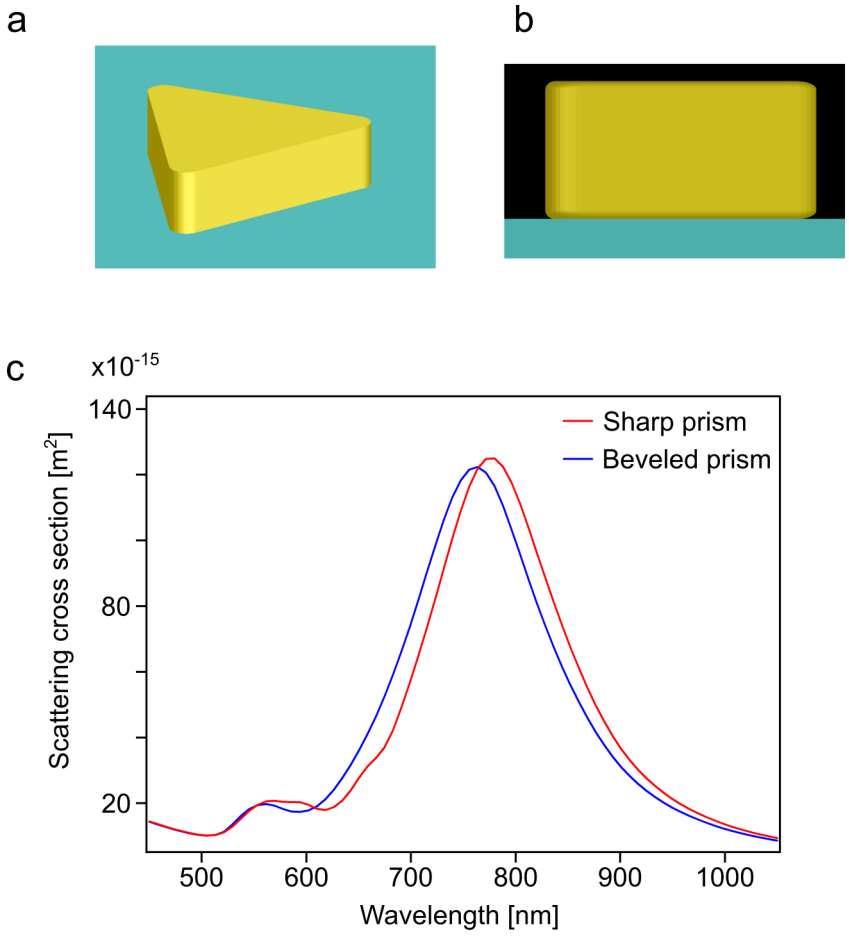

Figure 1.16: Scattering cross section plasmon shift for a sharp edged and beveled gold triangular nanoprism on an ITO surface. a) Cartoon for a sharp edged and b) a beveled nanoprism. The beveled prism cartoon is a cross-sectional image of the nanoprism highlighting the beveled edges. c) Scattering cross section spectrum showing a blue-shift in the plasmon resonance for the beveled nanoprism.

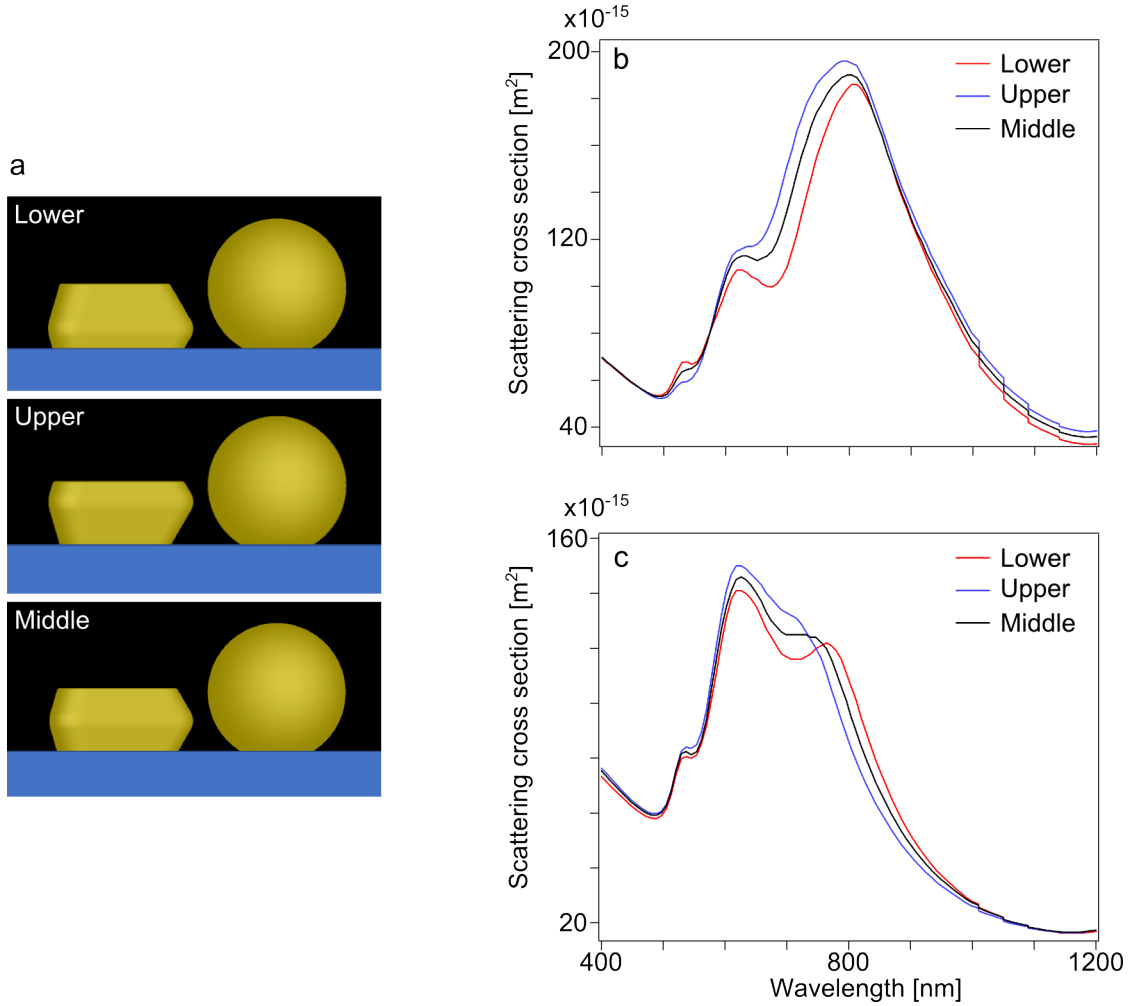

Figure 1.17: Scattering cross section plasmon shift for a sharp edged and beveled gold triangular nanoprism on an ITO surface. a) Cartoon for a sharp edged and b) a beveled nanoprism. The beveled prism cartoon is a cross-sectional image of the nanoprism highlighting the beveled edges. c) Scattering cross section spectrum showing a blue-shift in the plasmon resonance for the beveled nanoprism.

is observed when varying the bevel ROC. As the bevel is decreased from infinity to 0 nm, a blue shift in the dipole resonance is observed, Figure 1.18b. When the pair is excited along the short axis, the long wavelength resonance also shifts when varying the bevel ROC. As the bevel decreases, the resonance blue shifts. The lower wavelength plasmon resonance does not significantly alter for excitation along either the long or short axis.

A note worth making is the change in edge-to-edge distance (gap distance) between particles when varying the bevel ROC. For a bevel ROC of infinity, the gap distance for the pair is 18 nm. This corresponds with the measured gap distance taken from the top-down SEM image of the pair. As seen in Figure 1.18a, as the bevel ROC is taken to the extreme of 0 nm, the gap distance changes to larger values. For this particular pair, the gap distance becomes about 22 nm. When looking at the results for the two extremes, bevel ROC infinity and 0 nm, the shift in plasmon resonance goes from 849 to 812 nm, respectively. This 37 nm shift is too large to be from the change in gap distance alone. From simulations for the same TPS pair, changing the gap distance from approximately $18 - 23$ nm only produces a plasmon shift of $\sim$8 nm. This shows varying the bevel ROC shifts the resonance more significantly that the gap distance. This holds for pairs spaced by at least 18 nm. It is well known particle pairs spaced by $\sim 1 - 2$ nm can have large plasmon shifts when varying the gap distance by fractions of a nanometer. For the pairs with bevel ROCs ranging from $0 - 20$ nm, changes in gap distance are on the order of fractions of a nanometer, and will not produce a significant shift in the plasmon resonance at gap distances of 22 nm. This means as the bevel ROC varies from $0 - 20$ nm, the shift in resonance is attributed to the bevel ROC and not the small change in gap distance.

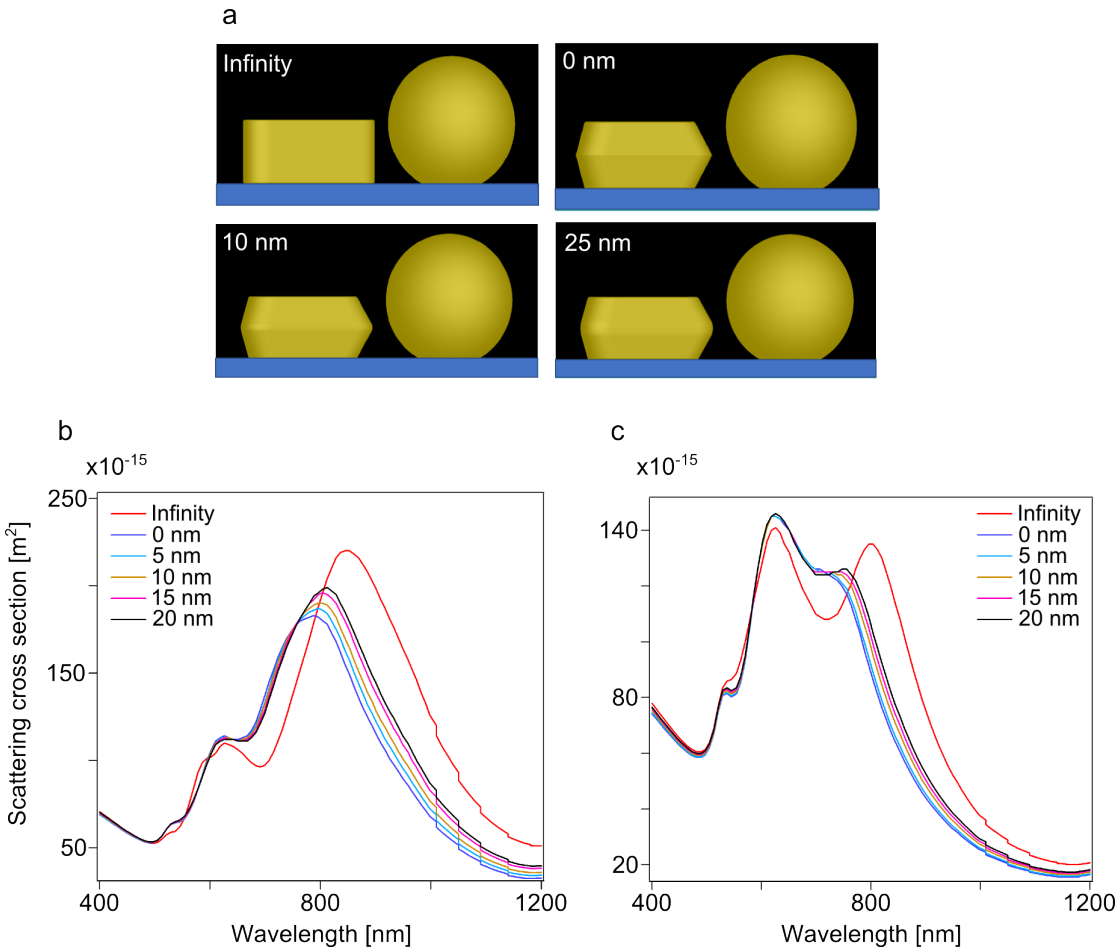

Figure 1.18: Scattering cross section plasmon resonance dependence on the radius of curvature of the bevel, also known as the bevel ROC. a) Cartoon showing the cross-section for the TPS pair. The cartoon highlights the change in radius of curvature at the vertex. b) Scattering cross section spectra when the pair is excited along the long axis and c) the short axis for radius of curvature ranging from 0 nm to infinity.

After the experimentally accurate pair geometry was determined, a gap dependence simulation for the scattering cross section was performed and was compared to experimentally collected scattering spectra. According to the simulations, the two resonances under investigation red-shift as the gap distance decreases when the pair is excited along the long axis, Figure 1.19a. When exciting the pair along the short axis, the higher energy resonance blue shifts as the gap distance is made smaller, Figure 1.19b.

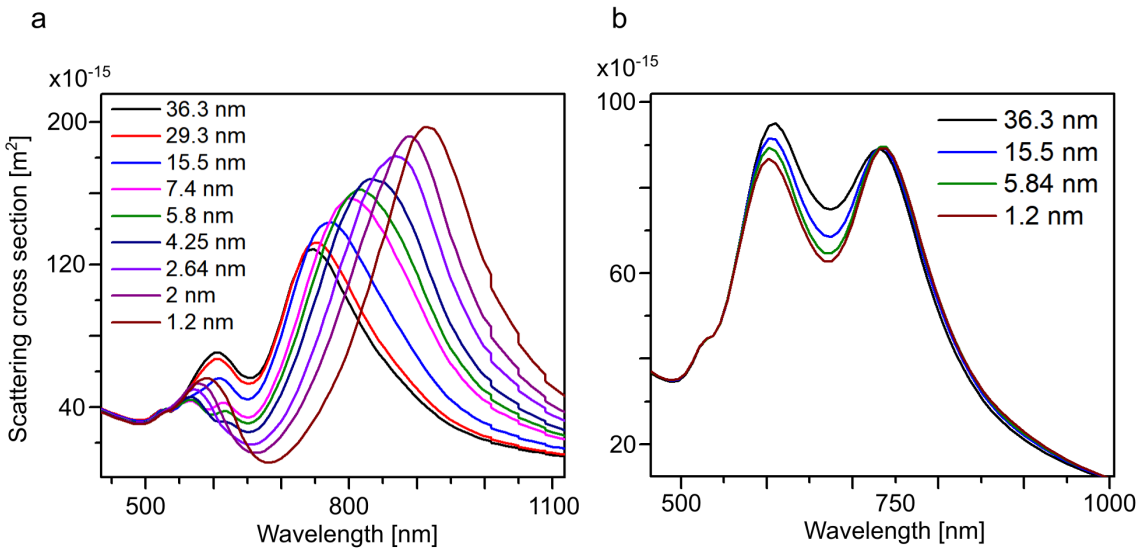

Figure 1.19: Simulated long and short axis scattering cross section plasmon shift for a TPS pair composed from a flat-bottom sphere and beveled triangular prism on a 120 nm ITO substrate. a) Scattering cross section spectra for a TPS pair excited along the long axis and b) for the pair excited along the short axis for edge-to-edge gap distances ranging from 1.2 to 36.3 nm. From the plots it's noted the stronger coupling for the pair when excited along the long axis, as evidenced by the large long wavelength plasmon shift.

When fitting the experimental data, the results qualitatively agree with the simulations. Unfortunately, as the gap distance becomes smaller, the long wavelength resonance shifts to the near-infrared (NIR) and is not detectable by the silicon CCD. The experimental results are still comparable to simulation results for gap sizes down to 5 nm. Although the experimental results cannot be directly compared to simulation results for smaller gap sizes, the simulation results are still analyzed to explain the plasmon shifts. The experimental and simulated results were obtained for several TPS pairs. As expected, no two TPS pairs are the same. For an ideal sphere, the particle is defined by its radius. The ideal triangular prism is defined by a few parameters. The first descriptor for the prism is the side length. Although the vertices for the triangular prism have a finite radius of curvature, the side length is determined by fitting the prism to an equilateral triangle. The side length is taken from the fitted equilateral triangle. The second descriptor is the aforementioned vertex radius of curvature.

Gap dependent simulations were performed for four experimentally determined TPS pairs. The simulated results show the absolute frequency shift of the long axis dipole mode is highly dependent on the geometry of the pair, Figure 1.20a. To gain some insight into how the geometry affects the gap-dependent plasmon shift for the TPS pair, we calculate a relative plasmon shift and plot it against the gap distance divided by the interparticle distance. This is the TPS analogy to the plasmon ruler equation for nano-sphere pairs [41]. The geometry of each pair is described by the individual particle frequencies and the distance between their centers. To calculate the relative frequency shift, one first starts with the coupled dipole resonance for the TPS pair, ω. Next, ω_{avg} is calculated by summing together the individual sphere and prism resonances and dividing by two. The relative frequency shift is then calculated using $(\omega - \omega_{avg})/\omega_{avg}$. The interparticle distance for the TPS pair is calculated from the distance between the centroid of the two particles. Determining the centroid for the sphere is straight forward using the top-down SEM image. The centroid for the triangular prism is determined by fitting the SEM image with an equilateral triangle, and then the centroid is determined by calculating the centroid for an equilateral triangle. Finally, the relative frequency shift is plotted versus the gap distance normalized to the interparticle distance and is shown in Figure 1.20b. From the plot, the results for individual pairs now fit nicely onto one curve.

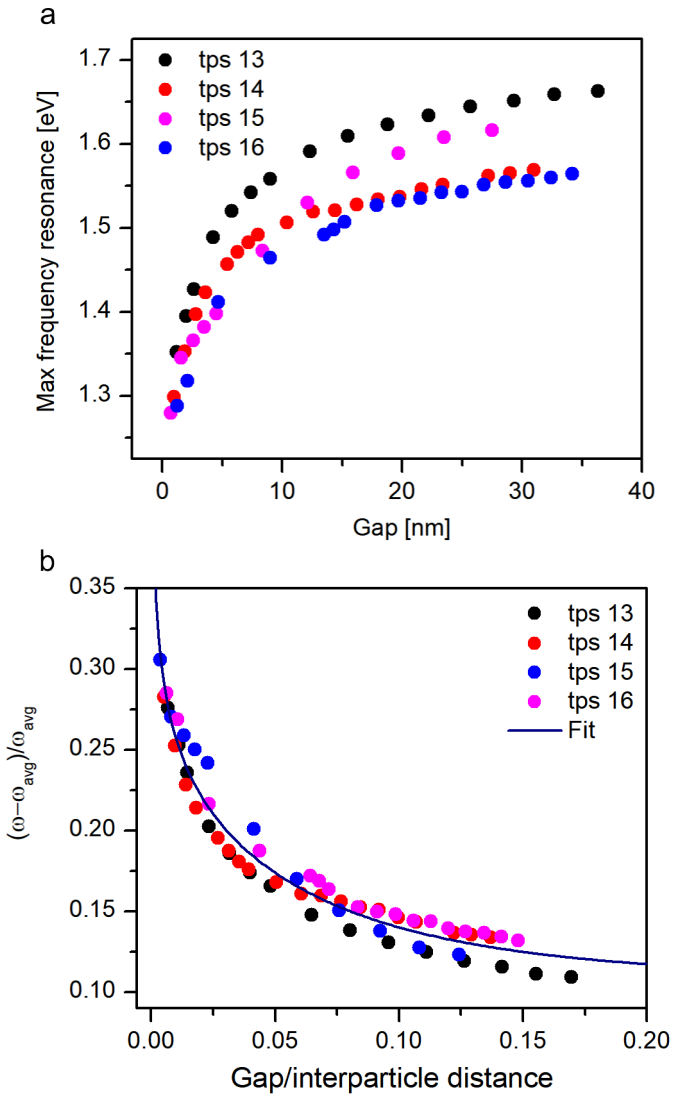

Figure 1.20: Multiple TPS pair long axis gap-dependent dipole frequency shift for FDTD simulations. a) Absolute and b) relative long axis dipole frequency shift for gap ranging from 1-40 nm. From the plots it's noted the absolute frequency shift is highly dependent on the pair's geometry. Considering the relative shift, by correcting for the geometry by incorporating the individual resonances and interparticle distance, much better agreement between individual pairs is observed.

Chapter 2

Anti-Stokes to Stokes ratios using plasmonic nantennas

Surface-enhanced Raman scattering (SERS) has been the topic of considerable research since its discovery nearly fifty years ago [42–44]. Despite the lengthy and storied history of SERS, its mechanistic details remain the subject of scrutiny and deliberation. The novelty of SERS comes from the enhanced electromagnetic (EM) fields at plasmonic nanostructures, which boost the feeble Raman effect by as much as 14 orders of magnitude, eventually reaching single molecule sensitivity [45–47]. With the advances made in plasmonics in recent years, it has become increasingly clear that atomistic detail matters in the description of surface plasmons and their mediation in the Raman response of molecules. The prototypical SERS measurements consisting of a Raman reporter introduced at the junction of two gold nanospheres [48], or a sphere on a mirror [49], has produced surprising results, in what has become known as the anomalous anti-Stokes-to-Stokes (AS-to-S) ratios.

A significant body of work has been dedicated to resolve the anomaly, such as treatments of SERS as cavity optomechanics, since it suggests a fundamental piece of the SERS puzzle

is missing. This chapter is dedicated to documenting the anomaly through systematic measurements and providing its satisfactory resolution. We will show that the anomaly can be assigned to single-beam coherent anti-Stokes Raman scattering (SB-CARS), driven by two pump photons present in the plasmonic junction. While this process dominates under picosecond (ps) pulsed laser excitation, due to the high peak powers, it persists in continuous-wave (cw) laser excitation in the single photon regime, due to the Poisson distribution of photons in a coherent source. It therefore does not involve strong fields, other than the enhanced field of single photons confined in a plasmonic nanojunction.

Early studies into SERS AS-to-S ratios attributed the enhanced ratios to a combination of laser intensity dependent temperature change and nonlinear optical pumping from the ground to excited vibrational state (vibrational pumping) [50–53]. Pioneering work in the anomalous AS-to-S field investigated several situations which could lead to atypical anti-Stokes (AS) scattering. The list includes vibrational pumping, plasmon resonance effects, and local heating. An early report focusing on vibrational pumping was made by Kneipp, et al [50], where they studied a system composed of either crystal violet (CV) or rhodamine 6G (R6G) in a colloidal silver aqueous solution. A cw Ti:sapphire laser (830 nm) was used to illuminate the system at relatively large average powers ($10 - 150$ mW). When sweeping the input intensity ($4 \cdot 10^{23} - 5 \cdot 10^{24}$ photons $\mathrm{cm}^{-2}\,\mathrm{s}^{-1}$), the authors observed nonlinear AS scattering and attributed the effect to vibrational pumping. Early works also suggested AS cross section enhancement due to the plasmonic resonance profile [54]. The works focused on ensemble-like responses and typically consisted of exciting a solution of functionalized SERS particles at relatively high average laser intensities.

A well-received article on anomalous AS-to-S ratios focused on temperature effects [52], and highlights multiple temperature considerations and sources. They consider the local environment temperature T_{env} (substrate plus ambient surrounding the sample), room temperature T_{room}, the metal nanoparticle temperature T_{met}, and the vibrational temperature of the

molecule T_{mol}. Ultimately, the study focused on collecting AS-to-S ratios as a function of the substrate temperature. Their goal was to investigate how the ratios change as a function of T over a range of about $125 - 350$ K. Through the investigation they provided insight into contributions due to heating and resonance effects. The sample was composed from a film of silver nanoparticles dispersed onto a silicon substrate, where the measurement was effectively an ensemble measurement of the total amount of hotspots fitted into the focused beam area. Also, five or more measurements were collected at many locations to average over the sample. The group used cw beams at 633 and 514 nm and used relatively large average intensities ($9 \cdot 10^{22}$ and $9 \cdot 10^{24}$ photons $\text{cm}^{-2}\,\text{s}^{-1}$).

2.1 Background

To start, Raman scattering obeys a transition rate described by Fermi's golden rule and is given by:

$$W = \frac{2\pi}{\hbar}\rho_0\left(\hbar\omega_s\right) N_i \left|\langle E_s\chi_{\nu'}\right| \alpha \left|\chi_\nu E_i\rangle\right|^2 \tag{2.1}$$

where N_i is the initial state occupation probability and $\rho_0\left(\hbar\omega_s\right)$ is the vacuum density of photon states. Raman spectroscopy has a long been associated with molecular temperature because AS and Stokes intensities are proportional to the populations of their respective initial vibrational states, which are thermally dictated. In general, thermally populated vibrational states obey Bose-Einstein statistics, but are simplified to the Boltzmann distribution because k_BT is low in comparison to vibrational energies. Implementation of the temperature sensitive technique is challenging when considering SERS because of the complex AS-to-S ratio, ρ. The contributions to ρ are described by Equation 2.2,

$$\rho = \frac{R_{AS}}{R_S} = A_v\left(\frac{\omega_L + \omega_v}{\omega_L - \omega_v}\right)^3\left(\exp\left[-\frac{\hbar\omega_v}{k_BT}\right] + \frac{\beta_s^2\beta_p^2\sigma_s I_L\tau}{\hbar\omega_L}\right) \tag{2.2}$$

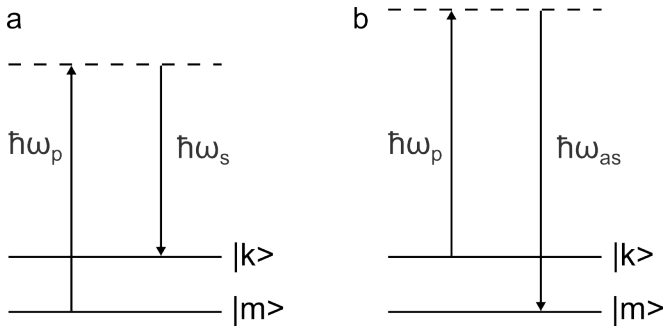

Figure 2.1: a) Stokes and b) anti-Stokes Raman scattering energy level diagrams. The diagrams depict a pump photon (ω_p) being instantaneously scattered, inelastically from a vacuum state, producing an oscillation at frequency ω_s or ω_{as}.

The relation holds for a Raman mode of frequency, ω_v, with excited state vibrational lifetime, τ, pumped using a laser with frequency, ω_L, at intensity, I_L. The Raman cross section (σ_s) and local temperature (T) are also included. The first and second terms in the parenthesis describe thermal population and vibrational pumping, respectively. Included, also, is a vibrationally dependent asymmetry factor (A_v) incorporating the enhancement factors at the AS and Stokes wavelengths, their respective cross sections (σ), and the fields representing the excitation source and AS and Stokes scattered fields.

$$A_v = \left| \frac{E_{as}}{E_L} * \frac{E_L}{E_s} \right|^2 \frac{\sigma_{as}}{\sigma_s} = \left(\frac{\beta_{as}}{\beta_s} \right)^2 \frac{\sigma_{as}}{\sigma_s} = \left(\frac{\beta_{as}}{\beta_s} \right)^2 \left(\frac{\omega_{as}}{\omega_s} \right)^3 \tag{2.3}$$

Although it is clear in the literature that Raman scattering is ω^3-dependent in the vacuum field [55–57], there is still confusion in the SERS community. While some reports accurately characterize the frequency dependence for Raman scattering [48, 58], there are several, some recent, which mistakenly characterize it as ω^4-dependent [49, 51, 52, 59–61]. For this reason, before addressing the temperature dependence for SERS, a brief derivation showing the ω^3-dependence in the vacuum field is given.

The stimulated Raman transition rate (w_{km}), via Fermi's golden rule, is written as [56],

$$w_{km} = \frac{2\pi}{\hbar}\rho\frac{2\pi\hbar(N_s+1)}{V}\omega_s\frac{2\pi\hbar N_p}{V}\omega_p|\boldsymbol{\epsilon}_p\cdot\alpha_{km}\cdot\boldsymbol{\epsilon}_s|^2 \tag{2.4}$$

where c is the speed of light and ω_s and ω_p are the Stokes and pump laser frequencies, respectively. N_p/V is the pump laser photon density and N_s is the number of stimulated Stokes photons in the scattering process ($N_s = 0$ for spontaneous Raman and SERS). The emitted density of states ρ is expressed using,

$$\rho = \frac{V}{(2\pi c)^3}\frac{\omega_s^2}{\hbar}d\Omega \tag{2.5}$$

Measured Raman count rates are proportional to the Raman differential cross section (DCS); therefore, one must know how the transition rate (w_{km}) is related to the DCS. The DCS is defined by,

$$d\sigma = \frac{\text{rate of scattering into solid angle } d\Omega}{\text{pump beam incident photon flux}} \tag{2.6}$$

The rate of scattering into a solid angle is simply $w_{km}\, d\Omega$ and the pump beam photon flux is $N_p c/V$. This value is equivalent to the pump photon flow rate per unit area that crosses a unit area. Accordingly, the stimulated Raman DCS is given as,

$$\frac{d\sigma_s}{d\Omega} = (N_s+1)\frac{\omega_s^3\omega_p}{c^4}|\boldsymbol{\epsilon}_p\cdot\alpha_{km}\cdot\boldsymbol{\epsilon}_s|^2 \tag{2.7}$$

The total cross section (σ) is recovered by integrating Equation 2.7 over the solid angle $d\Omega$,

$$\sigma = \oint_{4\pi}\frac{d\sigma}{d\Omega}\,d\Omega = 4\pi\frac{d\sigma}{d\Omega} \tag{2.8}$$

and total cross section becomes,

$$\sigma_s = 4\pi(N_s+1)\frac{\omega_s^3\omega_p}{c^4}|\boldsymbol{\epsilon}_p\cdot\alpha_{km}\cdot\boldsymbol{\epsilon}_s|^2 \tag{2.9}$$

The expression in Equation 2.9 for σ_s is the most general form for Raman scattering. It can be applied to both stimulated and spontaneous Raman. To apply the expression to spontaneous Raman, we simply set $N_s = 0$. A similar approach is performed for spontaneous AS scattering, and the resulting expressions for the spontaneous Raman cross sections become:

$$\sigma_s = 4\pi \frac{\omega_s^3 \omega_p}{c^4} |\boldsymbol{\epsilon}_p \cdot \alpha_{km} \cdot \boldsymbol{\epsilon}_s|^2 \tag{2.10a}$$

$$\sigma_{as} = 4\pi \frac{\omega_{as}^3 \omega_p}{c^4} |\boldsymbol{\epsilon}_p \cdot \alpha_{km} \cdot \boldsymbol{\epsilon}_{as}|^2 \tag{2.10b}$$

Finally, knowing that the Raman scattering rates are directly proportional to the total cross sections we find:

$$\begin{aligned} R_{as/s} \equiv \frac{R_{as}}{R_s} &= \frac{N_1}{N_0}\frac{\sigma_{as}}{\sigma_s} \equiv \frac{N_1}{N_0}\sigma_{as/s} \\ &= \frac{N_1}{N_0}\left(\frac{\omega_{as}}{\omega_s}\right)^3 \equiv \frac{N_1}{N_0}\omega_{as/s}^3 \end{aligned} \tag{2.11}$$

where R_s and R_{as} are the Stokes and AS scattering rates, and the shorthand notation has been introduced for the recurring ratios. From this final expression, we see the ratio between the rates is ω^3 and not ω^4-dependent. This is true for photon counting detectors such as CCDs, PMTs, and APDs. For further clarification, it is worth noting the ω^4-dependence persists from times when Raman scattered light was treated classically as dipole emitters and was measured using power meters [57, 62].

At thermal equilibrium, the ratio between excited and ground state populations is given by the Boltzmann distribution:

$$\frac{N_1}{N_0} = \exp\left(-\frac{\hbar\omega_v}{k_B T}\right) \tag{2.12}$$

From Equations 2.11 and 2.12, we see the AS-to-S ratio is effectively a vibrational thermometer:

$$T_{vib} = \frac{-\hbar\omega_v}{k_B \ln\left[\omega_{s/as}^3 R_{as/s}\right]} \tag{2.13}$$

Equation 2.13 is correct for spontaneous Raman, but we want to know how temperature affects the measured SERS rate. The principal mechanism of SERS is identified as the enhancement of local fields relative to the incident field, by a factor $\beta = E_L/E_0$. The enhancement is expected to be frequency dependent due to (broad) plasmonic resonances, as such, we give it an index to identify the considered fields. The SERS cross sections for the Stokes (σ_s^*) and AS (σ_{as}^*) are modified relative to the Raman cross sections:

$$\sigma_s^* = \beta_s^2 \beta_p^2 \sigma_s \tag{2.14a}$$

$$\sigma_{as}^* = \beta_{as}^2 \beta_p^2 \sigma_{as} \tag{2.14b}$$

where the quantity $\beta_s^2 = |E_{L,s}/E_0|^2$ and $\beta_p^2 = |E_{L,p}/E_0|^2$ are the Stokes and pump scattered field enhancement averaged over the surface of the SERS emitter. $E_{L,s}$ is the average magnitude of the field radiated by the SERS particle and E_0 is the input field supplied by the incident laser beam. After considering the enhancement factors, the SERS vibrational temperature becomes,

$$T_{SERS} = \frac{-\hbar\omega_v}{k_B \ln\left[\beta_{s/as}^2 \omega_{s/as}^3 R_{as/s}\right]} \tag{2.15}$$

The ratio between AS and Stokes is an important quantity, as will be shown in the following, therefore we introduce the concept of a vibrational dependent asymmetry factor, A_v,

$$A_v \equiv \beta_{as/s}^2 \tag{2.16}$$

As will be shown, nantennas illuminated by a laser source heat-up at a rate linear in the incident intensity (I_n),

$$T = T_0 + \kappa I_n \tag{2.17}$$

where κ is the heat transfer coefficient, with units of $\mathrm{K\,cm^2\,s\,photon^{-1}}$. The heating rate is a competition between the rate of energy absorbed and rate of cooling; therefore, it depends on the conductivity of the sample and environment. Equilibration among the vibrations is expected to occur on ∼10 ps time scales, while heating rates of nanostructures embedded in a dielectric occurs on time scales >100 ns. As such, a single vibrational temperature is expected to be maintained under steady state excitation, with heating resulting in a nonlinearity of the observed line intensities. To relate observable scattering rates to excitation intensities, it is useful to separate the material response and light intensity by writing rates in terms of Raman cross sections, σ ($\mathrm{cm^2}$) and incident light intensity, $I_n = E_i^2$ ($\mathrm{photons\,cm^{-2}\,s^{-1}}$).

To start, we consider a single molecular vibrational level at the intensity dependent temperature, $T = T_0 + \kappa I_n$. In addition to the thermal population, a laser with intensity I_n creates occupation of the excited level through optical pumping with a rate proportional to the Raman Stokes cross section (σ_s) and the laser intensity. Vibrations remain in the excited state for its lifetime (τ_v). More accurately, τ_v is defined as the time required for the instantaneously populated excited state to drop to 1/e of its value at excitation [63]. The rate equation for the excited state population N_1 becomes,

$$\frac{dN_1}{dt} = N_0\sigma_s I_n + \frac{N_0}{\tau_v}\exp\left[-\frac{\hbar\omega_v}{k_B(T_0+\kappa I_n)}\right] - \frac{N_1}{\tau_v} \tag{2.18}$$

where ω_v is the frequency of the vibration. The rate equation states that the rate of change of the excited state (dN_1/dt) depends on the rate of population (first two terms) and the rate of depletion (final term). The first term on the right shows the rate for optically populating the excited state, while the second term explains how the intensity dependent thermal population contributes to the excited state. In the steady state ($dN_1/dt = 0$) and for $I_n = 0$, the relation

becomes:

$$N_1 = N_0 \exp\left[-\frac{\hbar\omega_v}{k_B T_0}\right] \tag{2.19}$$

which is the population expected from Boltzmann statistics. When $I_n \neq 0$, the population is described by,

$$N_1 = N_0 \left(\exp\left[-\frac{\hbar\omega_v}{k_B(T_0 + \kappa I_n)}\right] + \tau_v \sigma_s I_n\right) \tag{2.20}$$

This equation says if the product of the input intensity and Stokes cross section is sufficiently large, a measurable optical contribution to the excited state will manifest itself through AS Raman scattering ($R_{as} \propto N_1$).

In going from normal Raman to SERS, we replace the Raman cross section (σ) with the SERS cross section (σ^*), and include the asymmetry parameter, $\sigma^*_{as} = A_v \omega^3_{as/s} \sigma^*_s$. The SERS scattering rates become,

$$R_s = N_0 \sigma^*_s I_n \tag{2.21a}$$

$$R_{as} = N_0 \sigma^*_{as} \left(\exp\left[-\frac{\hbar\omega_v}{k_B(T_0 + \kappa I_n)}\right] I_n + \tau_v \sigma^*_s I_n^2\right) \tag{2.21b}$$

$$\rho \equiv R_{as/s} = A_v \omega^3_{as/s} \left(\exp\left[-\frac{\hbar\omega_v}{k_B(T_0 + \kappa I_n)}\right] + \tau_v \sigma^*_s I_n\right) \tag{2.21c}$$

where the two unknowns are the heating rate constant (κ) and τ_v. The latter is limited by the coherence time obtained from linewidths, or directly obtained from time domain measurements. Otherwise, σ^*_s is the SERS rate obtained from measurements at low intensity, in the limit of zero heating and pumping, and can be reliably obtained from the slope of intensity measurement for R_s.

The above proposition fails in practice. We will describe sets of careful measurements on many nanostructures, cw and ps measurements, as a function of intensity. We find that the sequential excitation rate, to prepare v = 1 and probe it with a second photon via the AS emission, namely the second term in Equation 2.21b, is dramatically enhanced. Empirically,

the data can be fit by the inclusion of an anomalous enhancement parameter, η_v, of order 10^3, such that Equation 2.21b and 2.21c now read:

$$R_{as} = N_0 \sigma^*_{as} \left(\exp\left[-\frac{\hbar\omega_v}{k_B(T_0 + \kappa I_n)} \right] I_n + \eta_v \tau_v \sigma^*_s I_n^2 \right) \tag{2.22a}$$

$$\rho = A_v \omega^3_{as/s} \left(\exp\left[-\frac{\hbar\omega_v}{k_B(T_0 + \kappa I_n)} \right] + \eta_v \tau_v \sigma^*_s I_n \right) \tag{2.22b}$$

The placement of the correction makes it clear that the AS rate from the thermal population (first term in parenthesis) is given correctly, and that it is the sequential process that does not obey the original proposal. The immediate suggestion is that rather than sequential excitation, the AS emission is generated via a coherent excitation; meaning, we are observing coherent anti-Stokes Raman (CARS). This is a novel proposition becomes it infers the Stokes field is being supplied by the localized plasmon. In the typical CARS experiment, pump and stimulating Stokes photon pulses is employed. The experiments make it clear that this is not necessary in SERS at plasmonic cavities with large enhancement factors.

Two important considerations are used to rationalize this result. Firstly, we note that a spontaneous versus stimulated rate process is distinguished by the density of the final optical states. When the transition occurs into a single cavity mode, spontaneous and stimulated rates become indistinguishable, or equivalently, spontaneous rates are enhanced by the Purcell factor. This does not explain the enhanced rate, because CARS and sequential Raman have the same number of acting fields, and if the enhancement was solely due to field enhancement factors, they would both be enhanced by β^8. The additional enhancement must come from the polarization, rather than the field. This may be argued to belong to the chemical enhancement mechanism, or just noting that the second pump field must act not on the bare molecule, but the plasmon dressed molecule (polaron) with a significantly larger dipole. This thesis will be supported by the detailed measurements and their analysis. Experimental measurements will be completed by carrying out proper CARS measurements, in which the "spontaneous"

and stimulated CARS processes can be simultaneously observed. We should note that the current measurements are carried out on nano-structures that show unusually large SERS enhancement factors, as such, are likely from junctions that contain asperities.

2.2 Methods

All experiments mentioned utilize a combination of optical design and engineering, and computer control to fully automate experimental controls and data acquisition. Computer control and automation is implemented because it maximizes the efficiency of the measurement process by yielding shorter experiment times, higher measurement throughput, and improved consistency and accuracy.

2.2.1 cw intensity sweeps using HeNe laser at 632.8 nm

We want to see if the anomalous AS-to-S ratios are wavelength dependent. This can help shed light into the physical nature of the ratios. First, we start by illuminating the sample with a HeNe laser (632.8 nm). We begin with the HeNe for two reasons: (1) We have the required notch filters at 632.8 nm to reject the Rayleigh scattered light from the spectrometer, and (2) we have $> 4000\,\mathrm{cm}^{-1}$ bandpass throughput at the grating center of wavelength of about 640 nm. In our case, this relatively large amount of bandpass throughput allows us to simultaneously collect complete AS and Stokes scattered spectra.

Surface-enhanced Raman scattering (SERS) spectra are collected for 1,2-Bis(4-pyridyl)ethylene (BPE) functionalized silica-coated gold nantennas using both a HeNe 632.8 nm laser and a 735.2 nm single-mode laser diode. The laser beams are individually focused onto the ITO coverslip-nantenna interface using a high NA objective (60x, oil immersion, 1.25 NA) in an inverted microscope (Olympus IX-71) and the scattered Raman photons are collected using

the same objective in an epi-configuration. Raman scattered light is delivered to a grating imaging spectrometer (Andor Shamrock 500i) equipped with a 1600x200 element TE-cooled CCD detector (Andor Newton 970). The scattered light is focused onto the entrance slit (slit width $= 70 - 80\,\mu$m) of a 500 mm focal length spectrometer. The relatively large slit width is used to maximize the Raman light entering the spectrometer while also trying to optimize the spectral resolution. The grating used is a 300 g/mm grating, thus acquiring high resolution spectroscopy is secondary to visualizing the AS and Stokes scattered spectrum simultaneously. The Rayleigh scattered light for the laser beam is filtered using a combination of notch filters. For the HeNe, two notch filters (SEMROCK: NF03-633E-25) are sufficient to totally suppress the reflected laser and Rayleigh scattered photons.

To ensure illumination of independent nantennas, a backscatter image of the sample is collected using a scanning-stage (NT-MDT: NTEGRA Spectra) and photodiode. To prevent detection of DC signal from the photodiode, the HeNe laser is modulated using an acousto-optic modulator (AOM) with 50:50 duty cycle at 1000 Hz. The modulated backscatter signal detected by the photodiode and is demodulated using a lock-in amplifier, and the resulting output DC voltage is routed to the scanning stage controller and an image is formed using the stage software.

The intensity-dependent Raman scattering measurements discussed in this article were collected using a fully-automated and computer controlled software program designed in NI LabView. First, to measure the Raman scattered signal as a function of input laser intensity, an attenuator composed of a polarizer, half-wave plate (HWP), and analyzer is inserted into the incident beam path. A calibration curve equating HWP orientation angle with laser power is collected and the results are saved into LabView. Requesting movement to a desired power rotates the HWP to the proper orientation dictated by the calibration curve. The resulting power value is measured to better than 1% uncertainty when compared to the input (i.e. desired) power. Finally, the initial, final, and interval power values are set and the

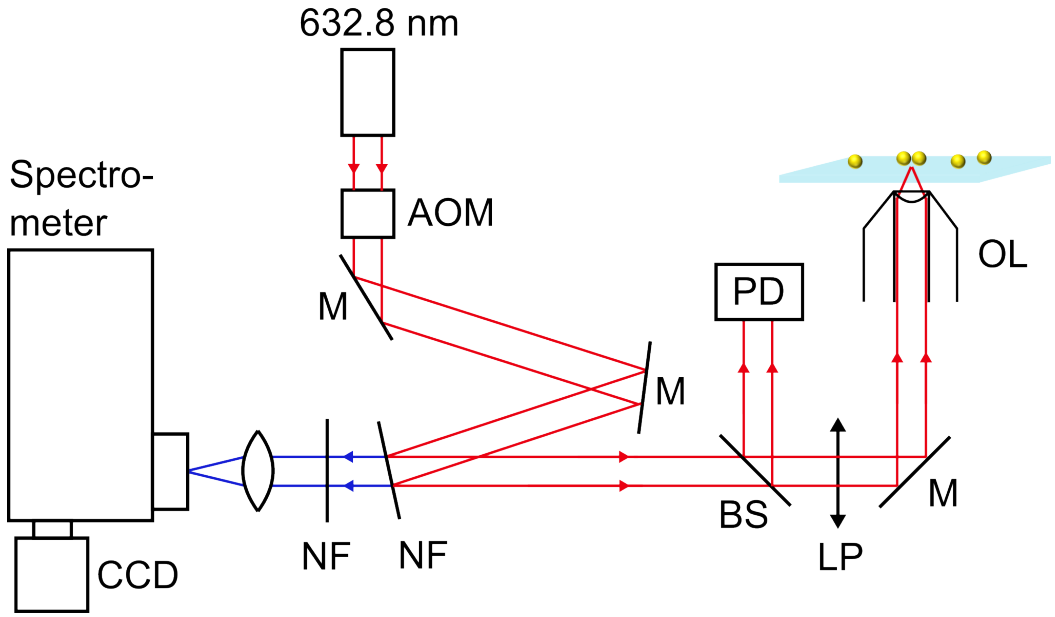

Figure 2.2: Surface-enhanced Raman scattering (SERS) incident (red) and collection (blue) paths when using the 632.8 nm HeNe cw laser. The optical components: (AOM) acousto-optic modulator, (M) silver mirror, (NF) 633 nm notch filter, (BS) microscope coverslip beamsplitter, (LP) linear polarizer, (OL) objective lens, (PD) photodiode, (CCD) camera detector. Although drawn using straight lines, we use the first-order diffracted output from the AOM and block all other orders using an iris diaphragm. Not depicted are the radio frequency (RF) and square-pulse generators, the electronic mixer, and the RF amplifier used to send 80 MHz pulses at 1000 Hz to the AOM to use it as an amplitude-modulator.

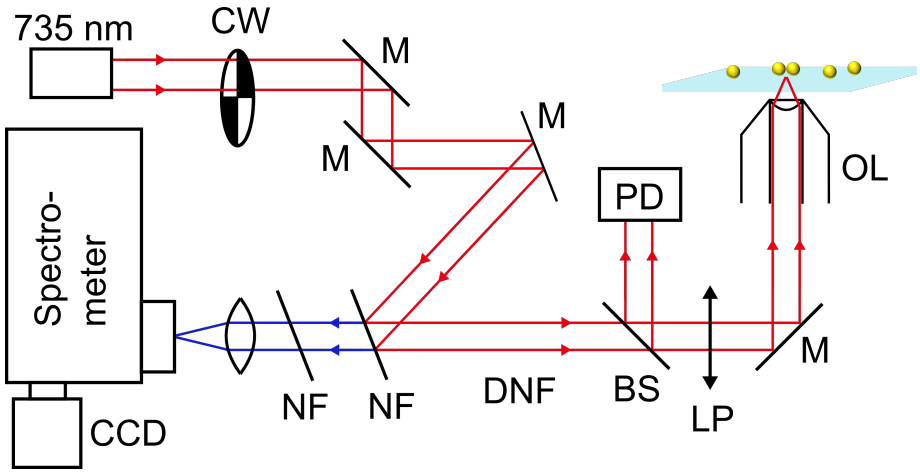

Figure 2.3: Surface-enhanced Raman scattering (SERS) incident (red) and collection (blue) paths when using the cw Sacher Lasertechnik tunable diode laser at 735 nm. The optical components: (CW) optical chopper wheel, (M) silver mirror, (NF) 785 nm notch filter, (BS) microscope coverslip beamsplitter, (LP) linear polarizer, (OL) objective lens, (PD) photodiode, (CCD) camera detector. The optical chopper modulates the laser at approximately 250 Hz for backscatter imaging using the photodiode detection and Lockin amplifier demodulation.

program begins. Data acquisition begins when a trigger pulse is sent to the CCD, which then sends a fire pulse to the software to signal acquisition completion. The fire pulse also acts to tell the software to move to the next power value. This iteration is performed until Raman is collected for all power values. An automated procedure allows for increased throughput, consistency, and accuracy, not otherwise offered.

2.2.2 cw Intensity sweeps using a 735 nm laser diode

The procedure differs slightly when performing experiments using a 735 nm laser as the pump source. Due to the diffraction grating (300 g/mm), we are limited to a bandpass throughput of $\sim$3000 cm^{-1}. As a result, we cannot record AS and Stokes scattered light at 1620 cm^{-1} simultaneously. To resolve this issue, we perform our experiments using two grating positions. One position allows us to collect the AS scattered light at 1620 cm^{-1}, while the second position provides detection of the same line Stokes shifted.

The laser diode uses a more unique combination of filters to reject Rayleight scattered photons originating from the pump source. First, the laser diode is reflected towards the microscope using a notch filter (SEMROCK: NFD03-785-25) oriented so the incident beam path is at an angle of $\sim 36^{\circ}$ with respect to the beam path to the microscope. This tunes the band block center wavelength to appear at 735 nm rather than 785 nm. The same logic is used for an additional notch filter of the same type with respect to the incident Rayleigh path. The two filters are necessary to fully block the reflected and Rayleigh scattered laser diode photons. The backscatter imaging procedure is identical for the 735 nm laser but the modulation is instead performed using an optical chopper with a 50:50 duty cycle at 280 Hz. The laser diode optical schematic for Raman spectroscopy is shown in Figure 2.3.

2.2.3 Instrument response function

The intensity values for the raw spectra are composed of the counts given by the analog-to-digital converter (ADC) for the CCD. Before the Raman photons are detected by the CCD, they experience attenuation to a degree dictated by the collection optics. We can construct an instrument response function (IRF), which we can use to better determine the amount of Raman photons scattered at the sample. We assume no photons are lost at the air-substrate interface and that no photons are lost due to reflection from the silver mirror used to reflect the scattered light from the collection objective to the spectrometer. This means the numbers we will present are slightly underestimating the amount of scattered photons at the nanojunction.

To determine the amount of Raman photons scattered at the sample, we correct for the transmittance or reflectance from the collection optics, and the grating and CCD quantum efficiencies. Figure 2.4 gives the IRF when considering the collection and Rayleigh filtering optics used for the 632.8 nm HeNe laser. The left-hand plot gives the IRF ranging from

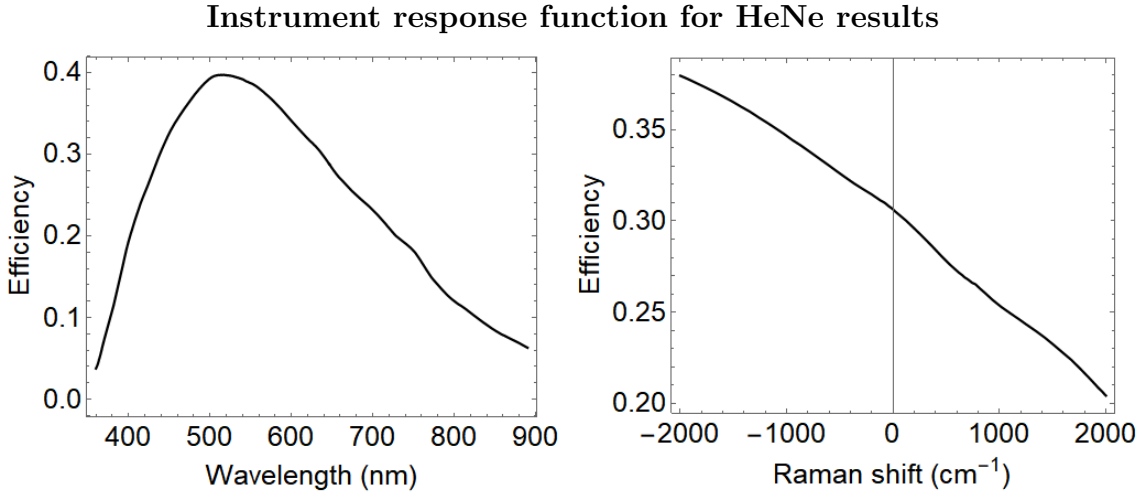

Figure 2.4: The instrument response function (IRF) used for the HeNe Raman results on a wavelength (left) and Raman shift (right) axes scale. For the Raman shift scale, a value of 0 cm^{-1} corresponds to the laser wavelength, 632.8 nm.

about 380-900 nm, while the right-hand curve gives the IRF on a Raman shift scale centered around a Rayleigh wavelength of 632.8 nm. The right-hand curve is representative of the range used to correct for the Raman scattered signal when using the HeNe laser. From the right hand-side curve, we lose approximately 2/3 to 4/5 of our Raman signal because of our detection efficiency determined by the IRF.

The IRF is composed from the transmittance or reflectance spectra for all the optics placed in the collection path. This includes the transmittance spectra for the objective lens, Rayleigh notch filter, and focusing lens to the spectrometer entrance slit, and also includes the reflectance spectrum for the three Al/MgF_2 mirrors inside the spectrometer housing. Lastly, the IRF also includes the 500 nm blazed grating and CCD quantum efficiencies. As previously mentioned, the entrance slit width was set to a value of $\sim 70 - 80\ \mu$m which resulted in very little signal loss. Therefore, the IRF assumes no signal loss at the entrance slit. This is confirmed by directly comparing the Raman counts at 70 and 250 μm slit widths. The resulting spectrum at 70 μm shows no signal loss when compared to the 250 μm spectrum.

2.2.4 Objective collection efficiency

The IRF given in Figure 2.4 is not the only source of loss when it comes to Raman detection. A significant amount of Raman signal is also lost due to the numerical aperture (NA) of the collection objective lens. Raman scattering has angular distribution; therefore, we measure the differential cross section ($d\sigma/d\Omega$) within a limited solid angle, $d\Omega$. Assuming angularly isotropic SERS scattering, we pull out the differential cross section from the integral over angles:

$$\begin{aligned} \sigma &= \oint_{4\pi} \frac{d\sigma}{d\Omega}\, d\Omega \\ &= \frac{d\sigma}{d\Omega} \int_0^{2\pi} \int_0^{\theta} \sin(\theta')\, d\theta'\, d\phi' \end{aligned} \tag{2.23}$$

where the second line in Equation 2.23 uses spherical coordinates. Notice the differential cross section has been pulled out of the integral because it does not depend on the polar and azimuthal collection angles. Using the definition of numerical aperture for a lens, the polar angel (θ) is determined using,

$$\theta = \text{ArcSin}\left[\frac{\text{NA}}{n}\right] \tag{2.24}$$

where $n = 1.51$ is the refractive index for the immersion oil. The Raman photon scattering rate (R) is then calculated from the measured count rates (W_{exp}) using:

$$R = \frac{W_{\text{exp}}}{\eta_\omega \Delta\Omega} \oint_{4\pi} d\Omega = N I_n \oint_{4\pi} \frac{d\sigma}{d\Omega}\, d\Omega = N_0 \sigma I_n \tag{2.25}$$

Equation 2.25 allows us to find the Raman cross section (σ) from the measured count rates. Using Equations 2.23 and 2.24, we can calculate the solid angle spanned by the objective lens ($\Delta\Omega$) as a function of NA. We note, the greatest collection efficiency is realized at $\theta = \pi/2$ radians; therefore, the maximum value for the double integral is 2π steradians (sr). This

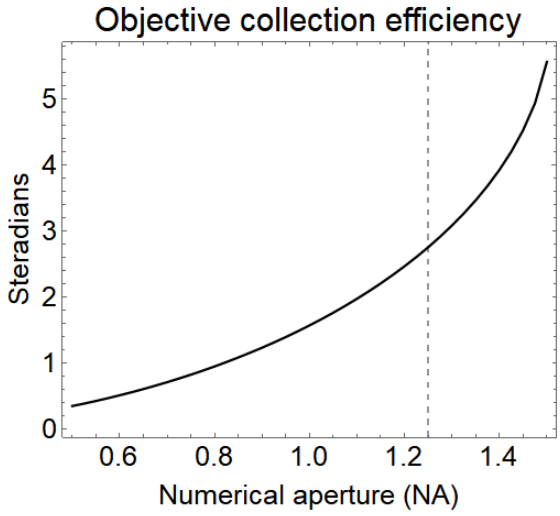

Figure 2.5: Oil-immersion objective lens collection efficiency in terms of steradians collected as a function of numerical aperture (NA). The gray dashed line indicates an objective NA = 1.25. The intersection of the solid curve with the dashed line yields the experimental value of 2.76 steradians. An efficiency is determined by dividing 2.76 by 4π, resulting in an efficiency of 0.219 (or 21.9 %) for our measurements.

result says, at a minimum, half the available Raman scattered signal is lost when collecting using a single objective lens.

Figure 2.5 shows the solution to the double integral in Equation 2.23 as a function of objective NA. The information in the curve allows us to define a wavelength-independent collection efficiency determined solely by the NA of the collection objective. For example, an ideal oil-immersion objective with NA = 1.51 would result in an objective collection efficiency of 0.5 (or 50 %). A gray dashed line indicating our experimental NA is visible in Figure 2.5. We can then determine our experimental efficiency by noting where the gray dashed line intersects the solid curve. For an oil-immersion lens at NA = 1.25, a solid angle of 2.76 sr of Raman scattered light is collected from a maximum amount of 4π sr. This tells us our objective lens has a collection efficiency of $2.76/4\pi = 0.219$ (or 21.9 %). This efficiency is wavelength independent and can be used to scale the results in Figure 2.4 to give a more accurate prediction for the total amount of scattered Raman photons at the sample plane.

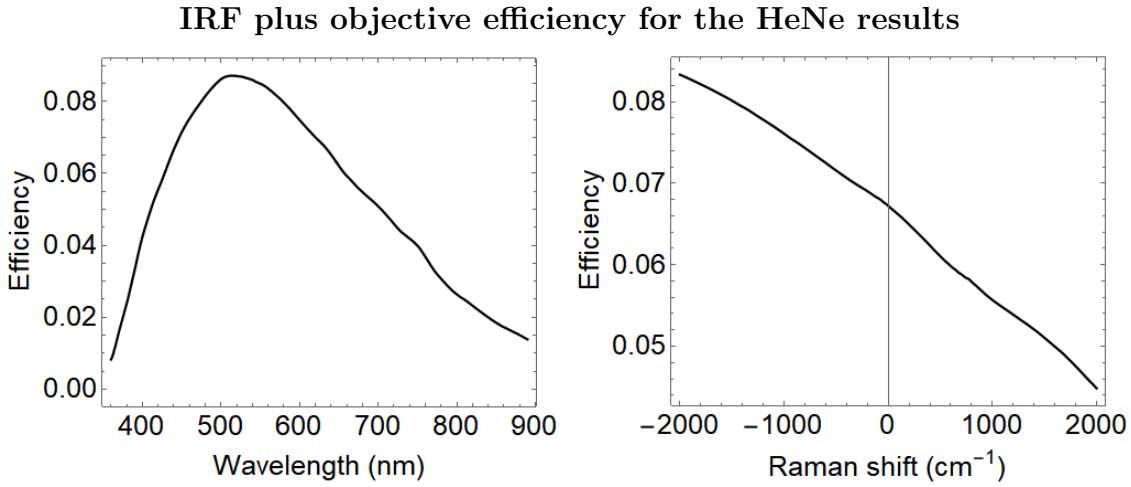

Figure 2.6: The total experimental collection efficiency including instrument response function (IRF) and the objective efficiency used for the HeNe Raman results on a wavelength (left) and Raman shift (right) axes scale. It is worth noting our Raman experiment using the 632.8 nm laser detects about 4 to 9 Raman photons for every 100 Raman photons scattered at the sample plane. The raw Andor results presented previously are corrected by the total efficiency curve given in the right-hand side plot.

By combining all sources of loss in the detected Raman signal, we can correct for our total collection efficiency. The total collection efficiency is defined as the product of the previously defined wavelength-dependent IRF and the wavelength-independent objective collection efficiency. Figure 2.6 gives the total collection efficiency when performing Raman using the collection optics and filters for a 632.8 nm laser beam. From the right-hand side curve, we see we only detect about 4 to 9 Raman photons for every 100 photons scattered at the sample plane.

2.3 SERS cross sections from measured count rates

From the measured spectral results, we see AS-to-S ratios which differ from those expected for a purely thermal excited state population. Figure 2.7 gives a SERS count rate spectrum representative of a silica-coated gold nantenna composed of $\sim 2-10$, as confirmed by scanning

electron microscopy (SEM). The results are intriguing due to the enhancement in the AS rates for the doublet at $\sim 1620\,\mathrm{cm}^{-1}$, observed using either a 632.8 nm HeNe (top row) or 735 nm laser diode (bottom row) pump source. The enhancement is manifested through the boost in AS rates that cannot be described by a thermal population alone. The pair of spectra are collected from the same nantenna with equal input intensities (41 $\mu\mathrm{W}/\mu\mathrm{m}^2$). An important observation is the increase in count rates when using the laser diode as the pump source, which is consistent over multiple nantennas. For eight of the nine nantennas where measurements were performed using both lasers, the five most intense modes showed SERS Stokes scattering rates that were a factor of $\sim 10-40$ times larger at 735 nm, depending on the resonance and nantenna of interest. We note that $\sim \omega^4$-dependence of scattering rates would predict the opposite, the scattering rate at 633 nm excitation should be ∼1.8 times larger than at 735 nm. Therefore, the Stokes cross sections should be ∼1.8 times larger and the observed Raman rates for 633 nm should be clearly greater. It is safe to conclude that the product of enhancement factors, $\beta_p^2\beta_s^2$, is larger at 735 nm. Indirect evidence suggests that the effect may be dominated by enhancement of the scattering rather than excitation.

All nantennas undergo laser irradiation induced degradation, as visualized from decreasing scattering rates versus irradiation time, which show a lower threshold at 633 nm. If we make the assumption that enhanced pump fields also lead to enhancement in non-radiative (heating) channels (which is not necessarily the case), then we can conclude that the effect is dominated by β_s^2. Stokes shifted Raman when using the HeNe falls in a wavelength window of $660-710$ nm, while Raman pumped using the laser diode falls in the window $770-840$ nm; meaning, β_s^2 is greater in the window of $770-840$ for the significant majority of nantennas. Larger β_s^2 values in this range is consistent with our observation on nantennas with small nanocavities; meaning, cavities with sub nm gap distances. Cavities with sub nm gap distances have been consistently shown to push the plasmon resonance further into the NIR [48]. Similarly, $660-710$ nm has been shown to be a region where plasmonic scattering diminishes. The region typical falls into the local minimum between the lower

and higher energy plasmon modes. We state with confidence that $(\beta_p^2\beta_s^2)_{735} > (\beta_p^2\beta_s^2)_{633}$; meaning, the product of the enhancement factors at the pump and Stokes frequencies are greater when using the laser diode as a pump. As stated, this is true for the five most intense modes. We can be more thorough and say, $(\beta_p^2\beta_s^2\omega_p\omega_s^3)_{735} > (\beta_p^2\beta_s^2\omega_p\omega_s^3)_{633}$. This inequality highlights how the enhancement factor terms work overtime to compensate for the more efficient scattering for the HeNe pump source due to the frequency dependence of Raman scattering.

For an optical contribution to the excited state population to manifest in the measured AS rates, the Stokes cross section needs to be significantly enhanced by the plasmonic nantenna. The plasmonic enhancement to the Stokes cross section can be determined by comparing the measured SERS Stokes spectrum to cross section values reported in the literature. The experimentally measured count rates (W_{exp}) are limited to a collection solid angle; therefore, in terms of the differential Raman cross section ($d\sigma/d\Omega$):

$$W_{\text{exp}} = \eta_\omega N I_n \frac{d\sigma}{d\Omega}\Delta\Omega \tag{2.26}$$

where η_ω is the frequency dependent collection efficiency (see Methods 2.2.3), N is the number of molecules, $\Delta\Omega$ is the collection solid angle, and I_n is the input laser intensity. We note η_ω is a frequency dependent function (i.e. spectrum) that corrects for the collection efficiency and also converts the measured count rate to a detected photon rate via the CCD quantum efficiency (QE) and sensitivity output. In this context, the CCD sensitivity output is the figure of merit which gives the CCD counts-to-electrons ratio. Assuming isotropic scattering, which is justified by the large NA of the objectives used, we measure the differential cross section (DSC):

$$\frac{d\sigma}{d\Omega} = \frac{W_{\text{exp}}}{\eta_\omega N I_n \Delta\Omega} \tag{2.27}$$

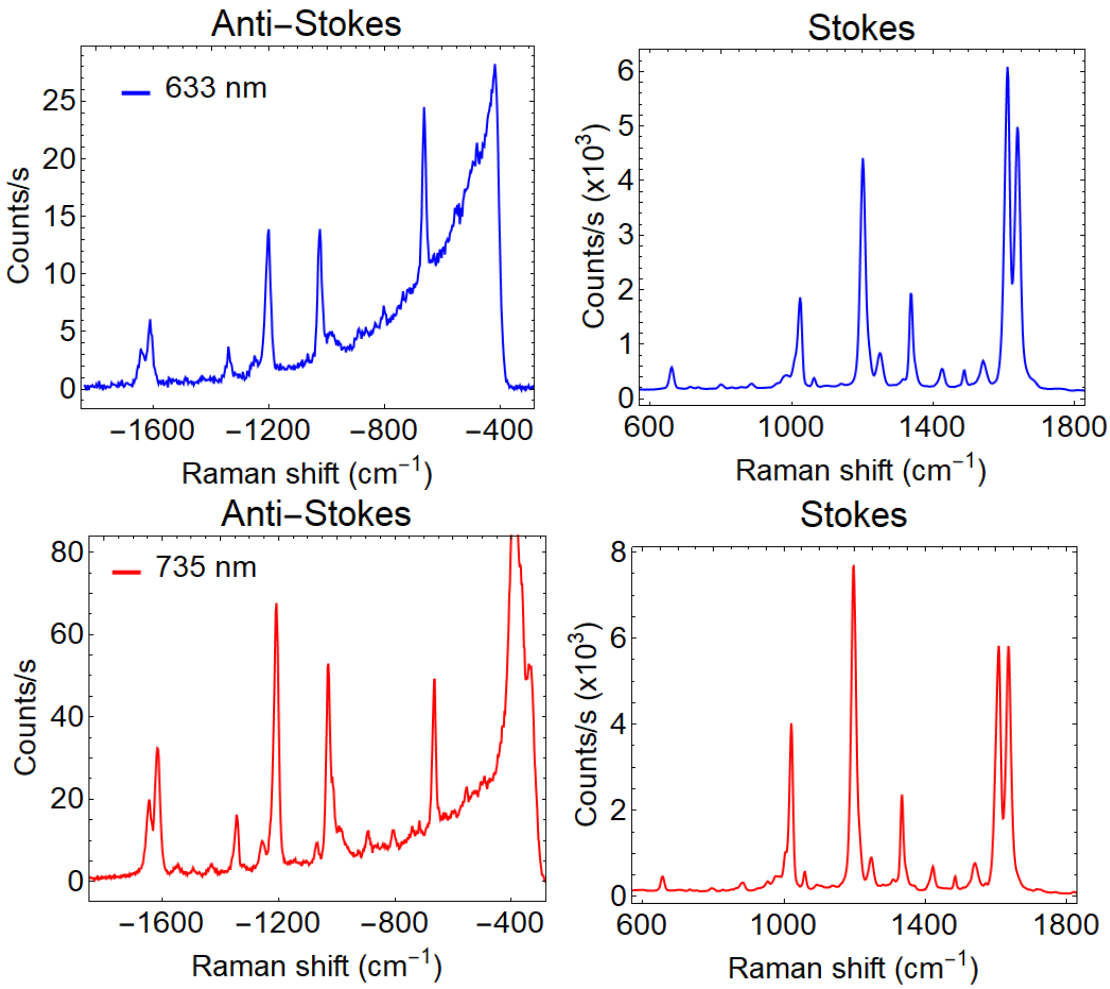

Figure 2.7: Measured SERS spectrum given for a BPE-functionalized silica-coated gold nantennas using laser wavelengths of 633 nm (top row) and 735 nm (bottom row). Both laser beams deliver 41 μW/μm^2 to the sample using an oil-immersion objective lens (NA = 1.25). The spectrometer entrance slit width (80 μm) is set to optimize the signal collection while still maintaining good spectral resolution. Notice the vertical axes are in units of counts per second; meaning, reported count rates are from the A/D converter for the CCD. The count rates reported here are proportional to the differential SERS cross section, which will be used to retrieve the enhancement factors.

The ratio of the measured DSC to that of the free molecule gives the enhancement factors. In the photon scattering rate equations, the total cross section (σ) is used, whose definition was stated previously by Equation 2.8.

Figure 2.8 shows a SERS spectrum for BPE-functionalized nantennas measured using a cw HeNe laser at 632.8 nm and an average laser power of 18 μW. The top row shows the measured results taken directly from the data acquisition software, Equation 2.26, and the bottom row shows results after being corrected for the instrument response, Equation 2.21a. If considering room temperature, which is reasonable for low power cw excitation in ambient conditions, we see from the spectrum that the AS scattering rates are greater than what is expected from a purely thermally populated excited state described by the Boltzmann distribution. This is clearest when observing and analyzing the doublet at $\sim$1620 cm^{-1}.

SERS enhancement factors (EFs) can be challenging to determine resulting in different protocols used to calculate them; therefore, a wide range of values have been given over time. In this work, we show EFs that are consistently around 10^{11} to 10^{12}. EFs at these orders of magnitudes are consistent over several nantennas and for two pump wavelengths used in these studies. We compare the measured Stokes SERS differential cross sections (DCSs) for BPE to reported Raman DCSs for BPE dissolved in ethanol [64], Table 2.1. We show representative BPE SERS Stokes photon scattering rates when using 633 and 735 nm lasers for the same nantenna, Figure 2.9. For the large majority of nantenna dependent SERS spectra, we consistently see larger Stokes cross sections for the 735 nm laser, when compared to the results using 633 nm. The 660 cm^{-1} mode is the exception to this rule; meaning, the 660 cm^{-1} mode is consistently larger for the 633 nm laser.

Moving forward, the DCSs for solid BPE dissolved in ethanol will be known simply as, Raman DCSs, and the nantenna BPE results will be known as SERS DCSs. The Raman DCSs were determined using a 633 nm HeNe laser; as such, we can make a direct comparison between our results and the literature values for 633 nm. We see the nantenna provides mode specific EFs

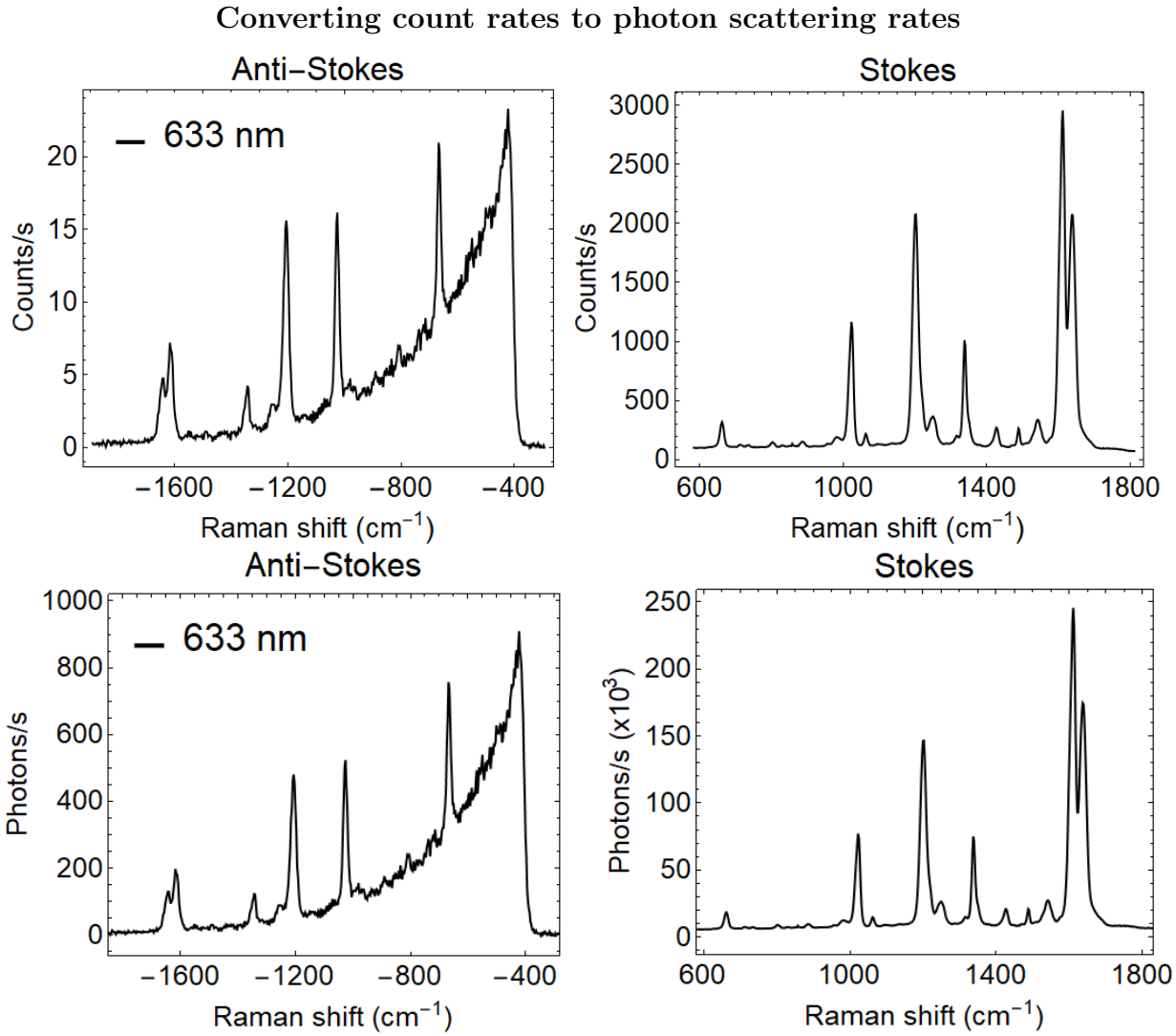

Figure 2.8: Measured SERS spectra in scattering units of counts s^{-1} (top row) and photons s^{-1} (bottom row). The measured results (W_{exp}) are converted, using Equations 2.25 and 2.8, to Stokes and AS photon scattering rates, R_s and R_{as}. Spectral intensity values reported as a count rate are proportional to the Raman differential cross section ($d\sigma/d\Omega$) and values reported as a photon rate are proportional to the total cross section (σ). By sweeping the input beam intensity and fitting the corresponding intensity dependent scattering rates, we can find SERS $d\sigma/d\Omega$ and σ for the modes of interest.

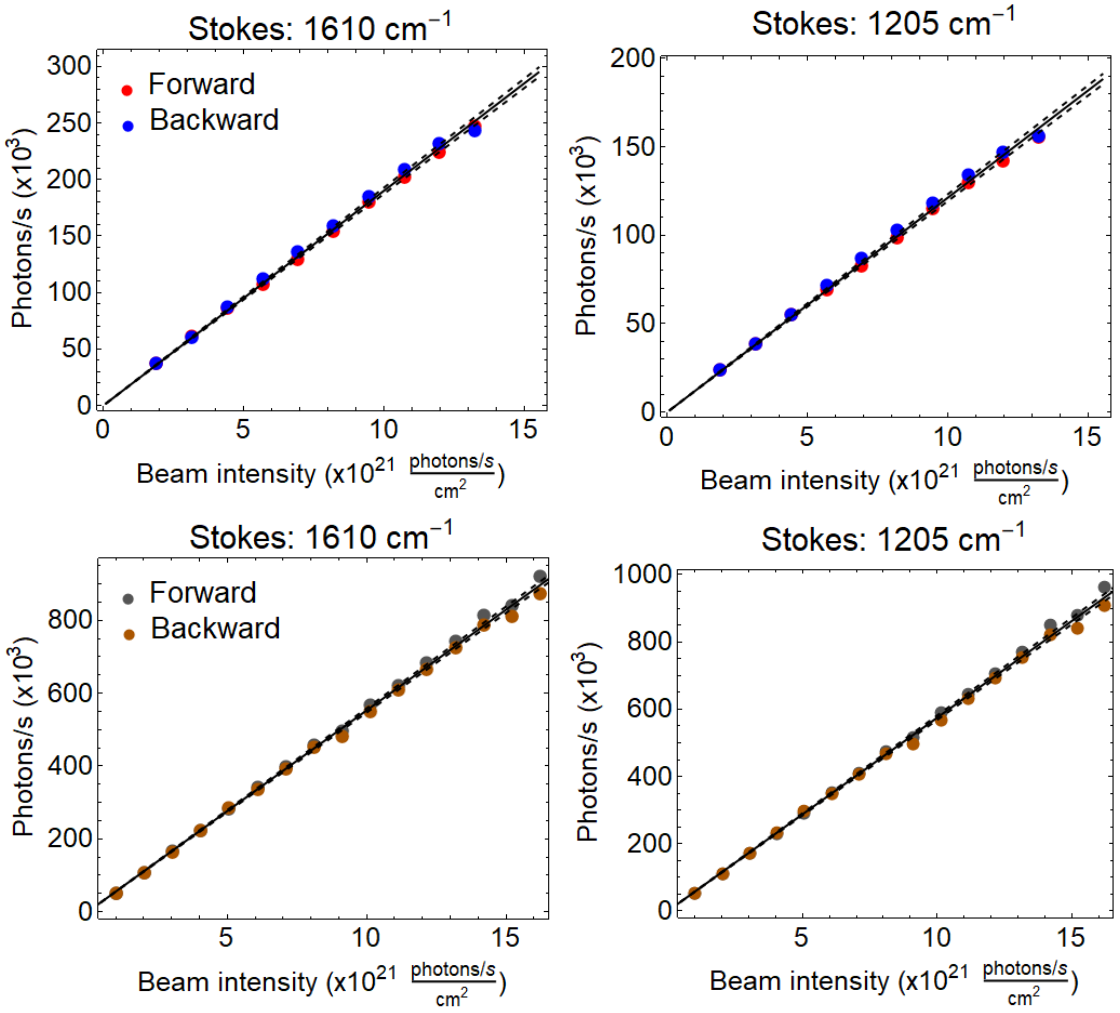

Figure 2.9: Stokes photon scattering rates as the input intensity is swept when using 632.8 nm (top row) or a 735 nm (bottom row) cw lasers. The measured results are from an identical nantenna, and are fit to a straight line (solid black) to retrieve the total cross sections (σ). The black dashed lines signify the 99% confidence intervals for the fit. The results show greater Stokes cross sections when using the laser diode (735 nm). This effect is consistent for the vast majority of nantennas interrogated.

ranging from approximately $1.5 - 7.0 \cdot 10^{11}$. Using the quartic law of enhancement, $EF = \beta^4$, this suggests a large local field enhancement of $\sim$800. An enhancement this large suggests a field which is localized to a small asperity in the nanojuction [49, 65]. An enhanced field localized to an asperity suggests the bulk amount of SERS scattered light contributing to the total signal is coming from a single molecule.

It is worth mentioning that our measurements are performed on the stronger scattering nantennas. This adds to our previous assertion suggesting the nantennas under investigation are localizing the fields to an asperity in the junction. The surrounding, weaker, scattering nantennas likely have nanocavity rather than pico-cavity junctions. In recent years, a pico-cavity junction has been reserved to describe a plasmonic junction localized at an asperity. Another piece of evidence to suggest that we are probing pico-cavities is the observed signal degradation. When the investigated nantennas are illuminated at relatively large powers >30 μW, we see a small but persistent decrease in the Raman signal. The persistent degradation manifests as a weakening in the Raman signal but we typically do not see an introduction of new vibrational modes in the spectrum. This suggests a widening of the junction; therefore, a decrease in the local field and Raman signal strength. In other words, the asperity is reorganizing and finding a new equilibrium, due to local heating from the high local fields.

Table 2.1: Mode dependent spontaneous ($d\sigma_s/d\Omega$) and SERS ($d\sigma_s^*/d\Omega$) Stokes differential cross sections (DCSs) for BPE and their associated enhancement factors (EFs). The spontaneous Raman results were collected using a 632.8 nm HeNe laser [64]. We report relatively large EFs, suggesting SERS signal is being amplified by an asperity in the nanojunction.

cm^{-1}	$d\sigma_{s,633}/d\Omega$ (cm^2/sr)	$d\sigma^*_{s,633}/d\Omega$ (cm^2/sr)	$d\sigma^*_{s,735}/d\Omega$ (cm^2/sr)	EF_{633}
1640	$5.5 \cdot 10^{-29}$	$1.6 \cdot 10^{-17}$	$5.4 \cdot 10^{-17}$	$2.9 \cdot 10^{11}$
1610	$2.9 \cdot 10^{-29}$	$1.9 \cdot 10^{-17}$	$5.5 \cdot 10^{-17}$	$6.6 \cdot 10^{11}$
1335	$1.4 \cdot 10^{-29}$	$4.0 \cdot 10^{-18}$	$1.4 \cdot 10^{-17}$	$2.9 \cdot 10^{11}$
1205	$2.1 \cdot 10^{-29}$	$1.2 \cdot 10^{-17}$	$5.8 \cdot 10^{-17}$	$5.7 \cdot 10^{11}$
1020	$2.6 \cdot 10^{-29}$	$4.4 \cdot 10^{-18}$	$2.2 \cdot 10^{-17}$	$1.7 \cdot 10^{11}$
660	—	$9.0 \cdot 10^{-19}$	$1.6 \cdot 10^{-18}$	—

2.4 Evidence for junction heating

Although we know optical contributions to the AS scattering rate have been necessary to explain previous reports, we start by seeing if we can model our results using a purely thermal model where the modes are heated at some equivalent rate for each mode. Previous reports have suggested thermal equilibrium between molecular and electronic temperatures of the metal [48], but this claim cannot be made by our results. This statement is highlighted by the electronic Raman scattering (ERS) results given in Figure 2.10. The ERS profile (Figure 2.10a) can be approximated using Boltzmann statistics [48, 66, 67]; therefore, is fitted using a Boltzmann distribution:

$$I_{ERS} = \omega^3 \exp\left[-\frac{\hbar\omega}{k_B T_e}\right] \tag{2.28}$$

The extracted electronic temperature for each input intensity value is plotted, Figure 2.10, and the result is a linear relation between the electronic temperature and the input laser intensity. The ERS temperature dependence on the input intensity is excellent evidence to

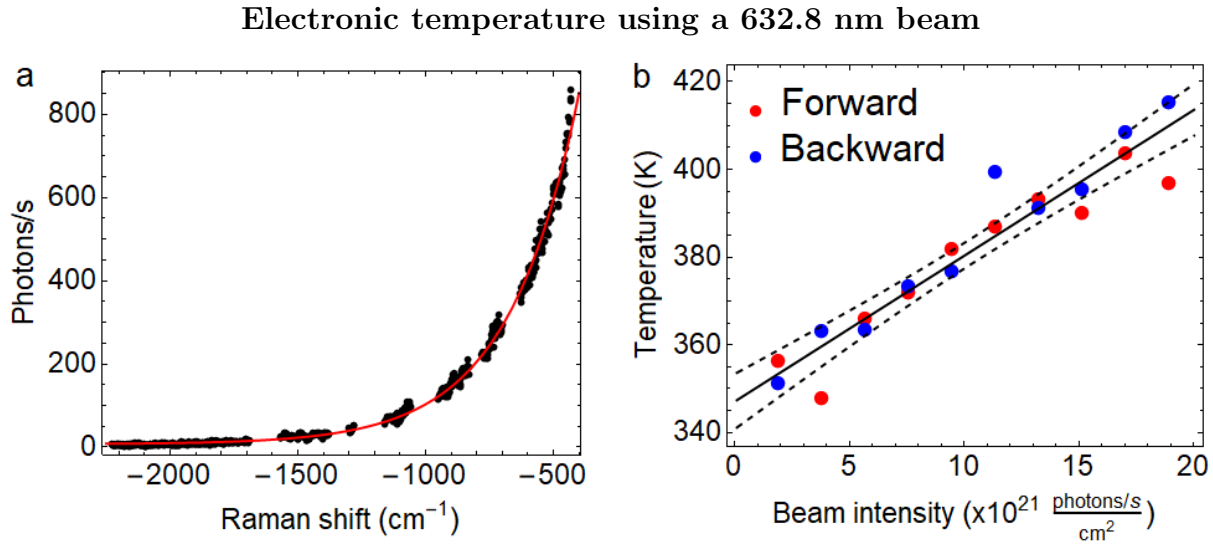

Figure 2.10: a) Fitting the electronic AS Raman scattering using (Equation 2.28) to extract the electron temperature at a specific input beam intensity value. b) The extracted electron temperature as a function of input beam intensity. The results suggest electronic temperatures that are greater than the vibrational temperature, and a linear relation between electronic temperature and input intensity.

suggest a heating contribution to the AS scattering rate. However, the extracted values of the temperature using Equation 2.28 are unreliable. This is evident by the intercepts of the linear dependence: $T(I_n = 0) \sim 350$ K instead of the ambient 295 K. Therefore, a meaningful comparison between vibrational and electronic temperatures cannot be made. Now that we are certain we are seeing heating of the molecule in the nanojunction, we see why we have included the heating rate terms in Equations 2.22a and 2.22b.

To further demonstrate the discrepancy between plasmonic and vibrational temperatures, we plot the implied vibrational temperature using the measured AS-to-S ratio and Equation 2.15. The resulting curve will suggest an intensity dependent excited state population if $T_{\text{vib}} \neq$ constant as a function of input intensity, Figure 2.11. When comparing Figures 2.10 and 2.11, it becomes clear that the effect on AS-to-S is not purely thermal. If the effect was purely thermal, we would expect to see plasmonic and vibration temperatures which have equivalent values when plotted against input intensity. The curves in Figure 2.11 suggest

the molecular temperature is lower than room temperature, which cannot be so for this measurement. Therefore, a purely thermal model for the excited state is not reasonable.

2.5 Raman as a vibrational temperature probe and the asymmetry factor

Raman has been successfully used as a vibrational temperature probe [55, 68, 69]. Starting with the assumption that the AS population ($N_{v=1}$) is purely thermal,

$$\begin{aligned} \rho = R_{as/s} &= \sigma^*_{as/s} \exp\left[-\frac{\hbar\omega_v}{k_B T}\right] \\ &= A_v \omega^3_{as/s} \exp\left[-\frac{\hbar\omega_v}{k_B T}\right] \end{aligned} \tag{2.29}$$

where ω_v is the Raman shift for the vibration under consideration and A_v is the asymmetry factor which has previously been defined as the ratio between the AS and Stokes enhancement factors, Equation 2.3. To use the values of ρ to calculate the molecular temperature, we can take the ratio of the mode specific integrated AS and Stokes rates from Figure 2.12. For normal Raman, one would expect to both retrieve the temperature of the molecule from ρ, and to observe a constant value for ρ as the input intensity is varied.

By rearranging Equation 2.29 and assuming no optical contributions to the excited state, the ratio between the ground and excited state populations can be obtained from the measurements:

$$\frac{1}{A_v}\omega^3_{s/as}\rho = \exp\left[-\frac{\hbar\omega_v}{k_B T}\right] = \frac{N_{v=1}}{N_{v=0}} \tag{2.30}$$

We can describe the unexpected, excited state population by considering the asymmetry factor (A_v). To clearly show the need for the asymmetry factor, we first set $A_v = 1$ in Equation 2.30 and plot the population ratio versus input intensity, Figure 2.13. When A_v is

Effective vibrational temperature using a 632.8 nm beam

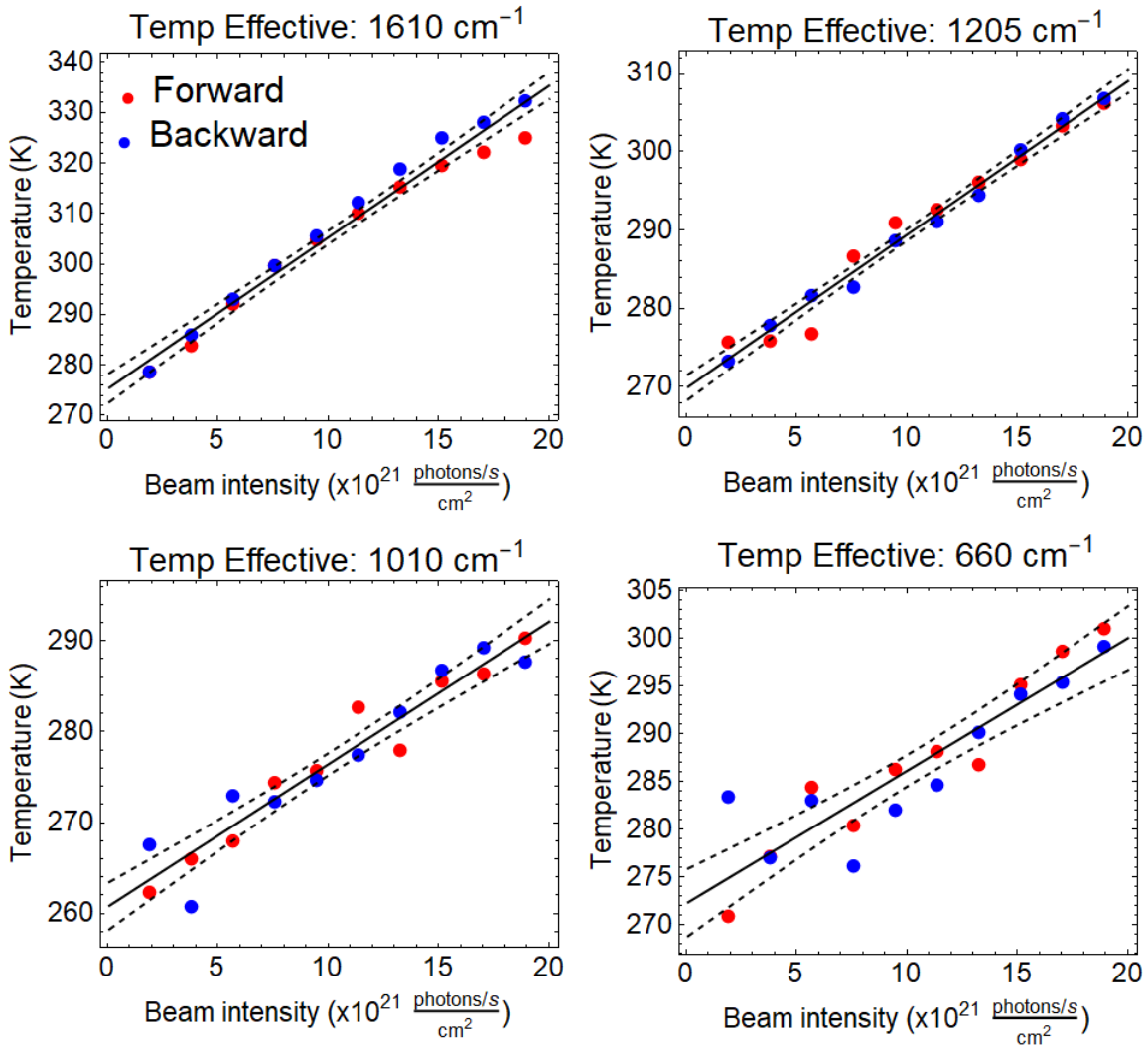

Figure 2.11: Using the measured intensity dependent BPE SERS AS-to-S ratios to calculate the effective vibrational temperature (Equation 2.13), assuming purely thermal excited states. The effective temperature versus input intensity for each labeled mode is fit to a line (solid black), which is bounded by the fit confidence intervals (dashed black). The results calculated the purely thermal model suggests the molecular temperature is colder than room temperature. The measurements are carried out at room temperature, so we expect the molecule to be at or greater than room temperature.

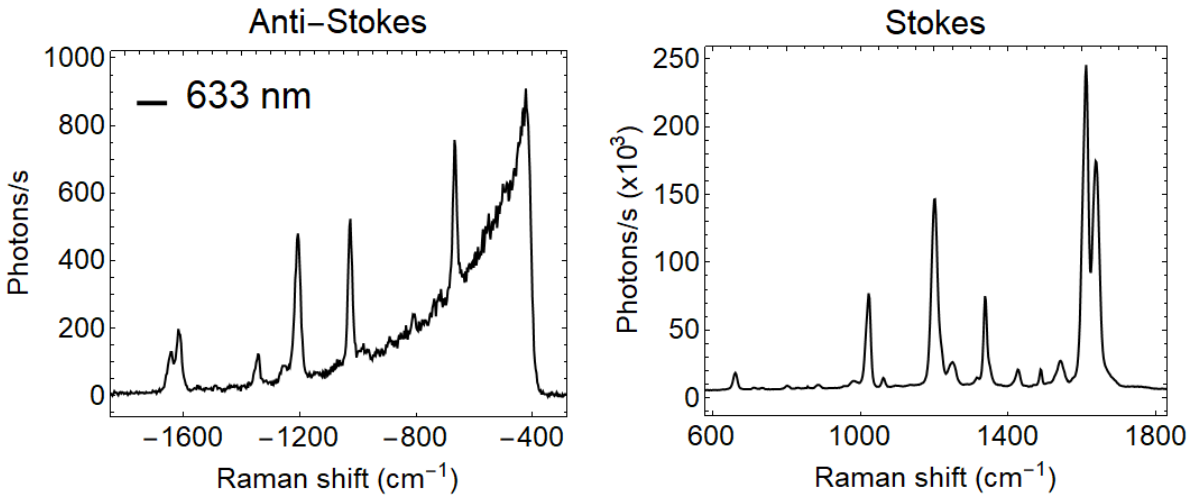

Figure 2.12: AS and Stokes scattering spectra from a BPE SERS nantenna when illuminating the nantenna with a cw HeNe laser at 632.8 nm. An oil-immersion objective lens (NA = 1.25) is used to focus the laser (18 μW) to the sample. Assuming a purely thermal population via Boltzmann statistics, the AS-to-S ratio from this spectrum can give the temperature of the molecule.

set to unity, the ratio between excited and ground state populations (horizontal green dashed lines) reaches values which are smaller than expected for room temperature. The results in Figure 2.13 suggest that $\beta^2_{s,633} > \beta^2_{as,633}$, which yields assumed populations that would be lower than expected for a thermally populated excited state at 295 K. Molecular temperatures are either in thermal equilibrium with the environment, or heated using the laser; therefore A_v is necessary to accurately model the results. The inclusion of A_v effectively raises the y-intercept of the measured results and fitted curves, yielding values that are greater than room temperature for all intensities (including $I_n = 0$). This assertion will become clearer in the following.

It is educational to first report the AS-to-S ratios to see if we obtain reasonable populations for the ground and excited state. Using the Raman spectrum, we can calculate the AS-to-S ratio, plot the result versus input laser intensity, and compare to what we expect from the Boltzmann distribution. The resulting curves are shown in Figure 2.13. The resulting curves suggest the following: 1) There is intensity dependence in the population ratio, due to thermal

(non-constant local temperature) or optical (sequential or coherent Raman) contributions. 2) The results are anomalous, in that, we are seeing populations which suggest the local molecular temperature is lower than room temperature. This cannot be so because the measurements are carried out at room temperature; therefore, the molecular temperature must be equal to or greater than room temperature.

Using a second laser source, 735 nm, we measure the BPE SERS spectrum to see how vibrational resonances, thermal population, and the asymmetry factor are influenced by pump frequency, Figure 2.14. We plot the spectra obtained using both the 735 nm (bottom row) and 632.8 nm (top row) lasers for direct comparison, where both sets come from the same nantenna. We then integrate over each of the two C=C modes (1610 and 1640 cm^{-1}), and take the AS-to-S ratio for each pump frequency and plot the results in Figure 2.15. From the curves, we see the pump frequency plays an important role in the measured AS-to-S ratios. As before, when we illuminate the nantenna using the 632.8 nm laser, we retrieve results which suggest excited state populations that are less than expected for a thermally populated state at 295 K. This says that $\beta^2_{s,633} > \beta^2_{as,633}$ and the Stokes scattered light is being enhanced preferentially over the AS light. When using the 735 nm laser as the pump, the opposite is true. We see intensity dependent ratios which suggest $\beta^2_{s,735} < \beta^2_{as,735}$, telling us that using the 735 nm laser as the pump source results in AS scattered light being enhanced to a greater degree than the Stokes scattered light.

Now that we have observed the dependence of the populations on pump frequency, we show how the asymmetry factor is used to explain the anomaly in the AS-to-S ratios. In Section 2.6, we will show how the asymmetry factors (A_v) are determined, but for now we will assume A_v is known for each mode; true whether the nantenna is illuminated with 632.8 or 735 nm laser light. Figure 2.16 shows the AS-to-S ratios after the results have been corrected using the mode specific A_v. To find the mode specific A_v values, we assume the molecule is at room temperature (295 K) when the input intensity is zero. The results highlight the

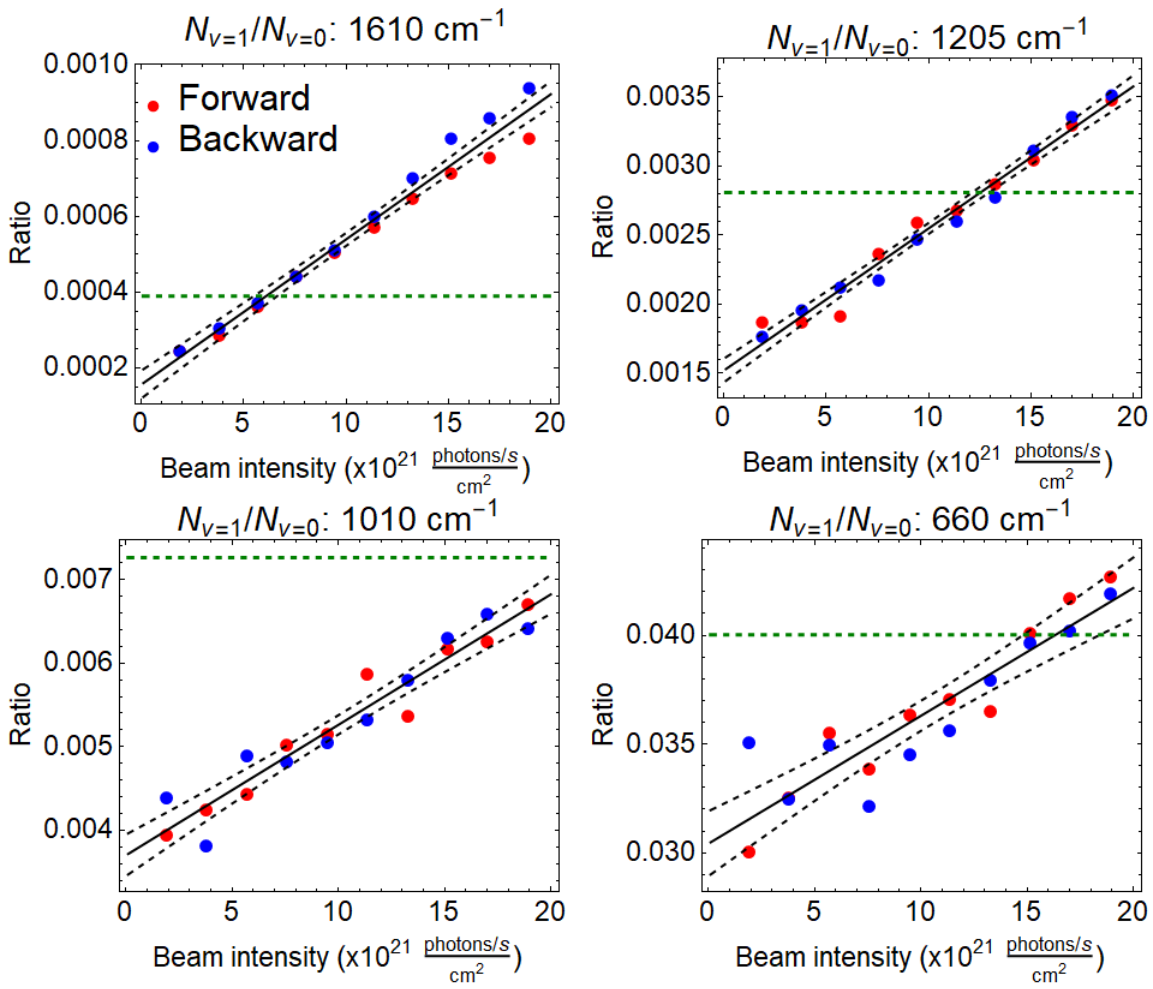

Figure 2.13: Using the measured BPE SERS spectrum, collected using 632.8 nm excitation, to calculate the ratio between excited ($N_{v=1}$) and ground ($N_{v=0}$) states as the input intensity is swept. The ratio for each labeled mode is fit to a line (solid black), which is bounded by the fit confidence intervals (dashed black). The horizontal dashed green line signifies the population for each mode assuming strictly thermal population via the Boltzmann distribution at 295 K.

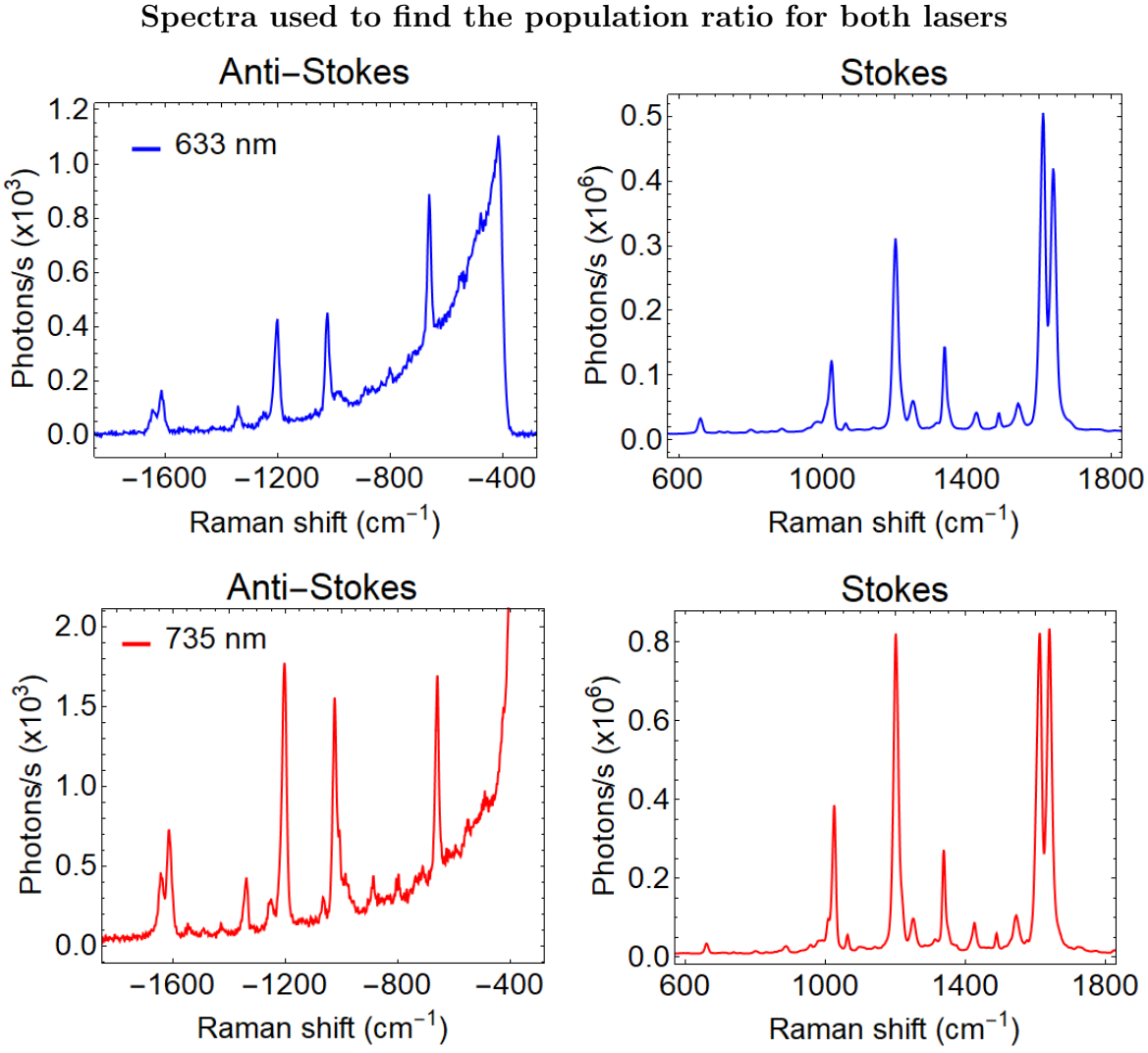

Figure 2.14: Two sets of BPE SERS spectra used to calculate the population ratio for when using either pump laser. AS and Stokes scattering spectra from a BPE SERS nantenna when illuminating the nantenna with a cw HeNe laser at 632.8 nm (top row) or a 735 nm single-mode laser diode (bottom row). The average power is approximately 12 μW for both lasers and an oil-immersion objective lens (NA = 1.25) is used to focus the laser onto the nantenna. When comparing the two sets of spectra, we see AS scattering rates are greater with respect to the Stokes rate when using the laser diode as the pump source.

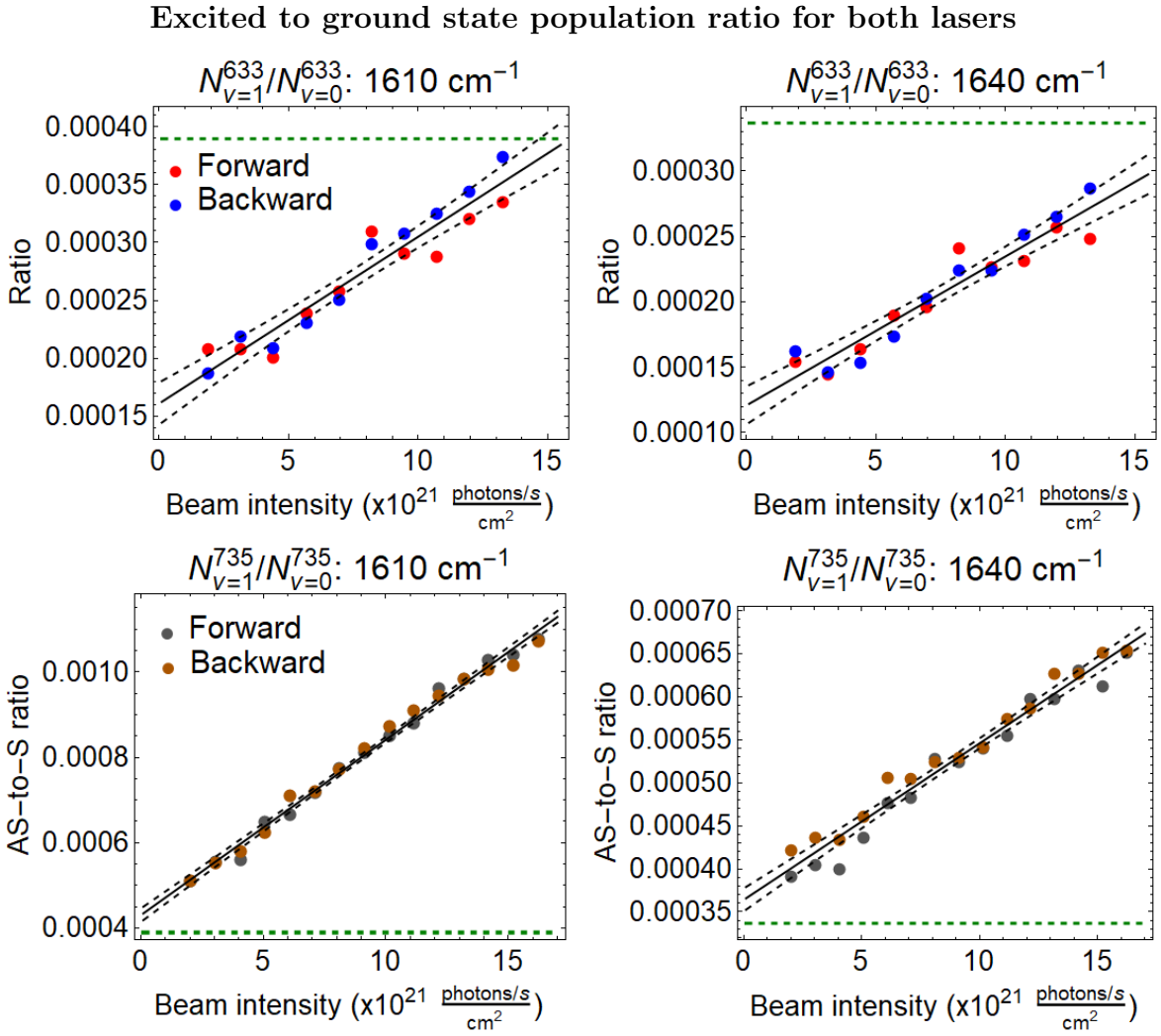

Figure 2.15: The ratio between excited ($N_{v=1}$) and ground ($N_{v=0}$) states as the input intensity is swept for both lasers. The asymmetry factor, A_v, is manifested by the measured results relation to the thermally expected population. The horizontal dashed green line signifies the population for each mode assuming strictly thermal population via the Boltzmann distribution at 295 K. Both sets of curves fail to yield the expected ratio at $I_n = 0$; that is, the ratio at room temperature (295 K).

significance of frequency dependent enhancement factors (EFs). After correcting for the EFs via the asymmetry factor, we retrieve populations that approach those expected for room temperature when $I_n = 0$. The asymmetry factor does not account for the seemingly linear relation between the AS-to-S ratio and input intensity; therefore, we must consider how intensity induced heating and optical contributions affect the AS scattering rates.

2.6 Heating rates from intensity sweeps

Ignoring the optical contribution term, and rearranging Equation 2.22b, we obtain:

$$\ln\left[\omega_{s/as}^3 \rho\right] = \ln\left[A_v\right] - \frac{\hbar\omega}{k_B\left(T_0 + \kappa I_n\right)} \tag{2.31}$$

We plot the AS-to-S ratio (ρ) results using the above expression and set $T_0 = 295\,\mathrm{K}$, resulting in the determination of the asymmetry factor (A_v) and heating rate (κ) for each vibration, Figure 2.17. This model assumes AS rates solely determined by intensity dependent heating. This assumption is most accurate for the 660 cm^{-1} mode but fitted plots for four prominent modes are displayed.

Using the purely thermal model for the AS-to-S ratio described by Equation 2.31, we see each mode is fit well when assuming AS rates that increase with intensity due to heating. However, each vibration shows a different heating rate. We expect thermal equilibrium among the vibrations, as such, the purely thermal model does not explain the observed populations. As a result, we must incorporate an optical pumping contribution to best describe the nonlinear AS rates. We see the smallest heating rate is that for the 660 cm^{-1} mode; thus, we choose this rate to use for the additional modes and incorporate the optical contribution to best model the higher frequency modes. Also, we expect 660 cm^{-1} to have a relatively small

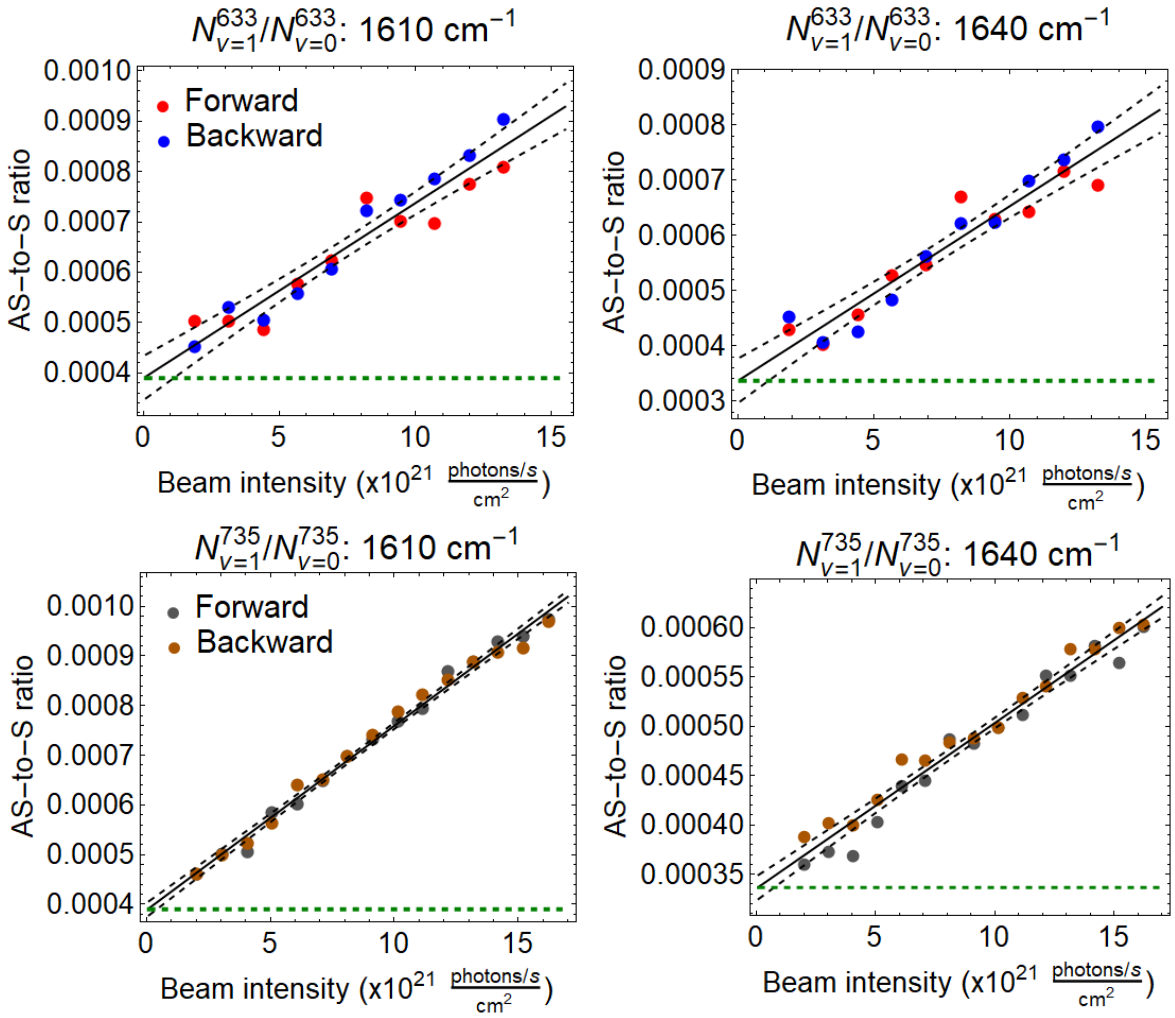

Figure 2.16: The ratio between excited ($N_{v=1}$) and ground ($N_{v=0}$) states when the AS-to-S ratio has been corrected for the asymmetry factor, A_v. The horizontal dashed green line signifies the population for each mode assuming strictly thermal population via the Boltzmann distribution at 295 K. We now see how incorporating the asymmetry factor yields the thermally expected ratio at $I_n = 0$.

Table 2.2: Mode specific heating rates for a nantenna illuminated using a 632.8 nm HeNe. The heating rates tabulated here are from the fits in Figure 2.17.

Mode (cm^{-1})	κ (10^{-21} $\frac{K\,cm^2}{photons\,s^{-1}}$)
1640	2.5
1610	3.2
1205	2.2
1010	1.8
660	1.5

optical contribution, by virtue of its Raman cross section being $\sim 10x - 100x$ smaller than the four more prominent modes.

After recording intensity sweeps on multiple nantennas, we find that different nantennas have unique heating rates. To this point, intensity sweep measurements using both the 633 and 735 nm lasers have been performed on four nantennas. Heating rates determined by the 660 cm^{-1} mode are given in Table 2.7. As stated, the results suggest heating rates are highly dependent on the specific nantenna and have secondary dependence on the laser source. This conclusion is made because one laser does not consistently heat the nantenna more than the second laser. We suspect nantennas that have larger heating rates using the 633 nm laser have greater absorption cross sections at 633 nm, and similarly for the 735 nm laser.

2.7 Optical contribution to the anti-Stokes scattering rates

Now that we know how to solve for the heating rate of the sample, we can use it to find the optical contribution needed to fit the AS and AS-to-S curves. The AS scattering rate has been previously described by Equation 2.22a and includes thermal and optical contributions to the nonlinearity. The term η_v is a frequency dependent anomaly coefficient needed so that the optical contribution to the scattering rate competes and surpasses the thermal

Heating coefficient extraction from the AS-to-S ratio using a 632.8 nm beam

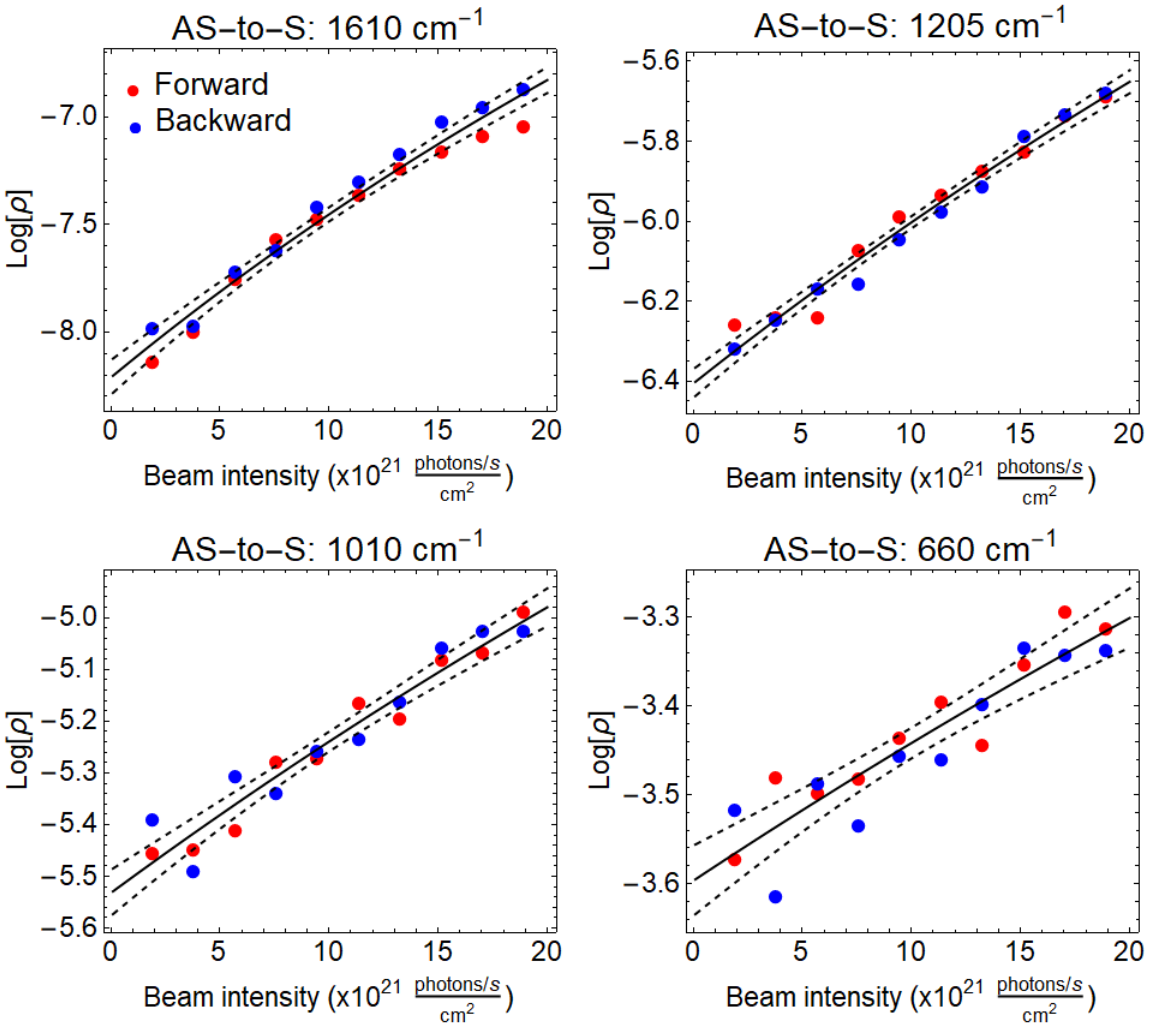

Figure 2.17: Curves and fits for the AS-to-S ratio using a purely thermal model and Equation 2.31. The fits show each mode can be described using a purely thermal model but the heating rate for each mode is unique. We know the sample is heated at a rate constant for each vibration; therefore, we use the heating rate for the 660 cm^{-1} mode because it is the smallest rate and has the smallest Stokes cross section.

Table 2.3: Vibration dependent asymmetry factor (A_v) and anomaly coefficient (η_v) from the fitted results in Figure 2.20 assuming $T_0 = 295\,\mathrm{K}$ when $I_\mathrm{n} = 0$ (photons $\mathrm{cm}^{-2}\,\mathrm{s}^{-1}$).

Resonance (cm^{-1})	A_v (unitless)	η_v (unitless)
1640	0.94	581
1610	0.80	805
1205	0.72	1570
1010	0.66	2920
660	0.79	—

contribution. We assume all vibrations have an equivalent heating rate (κ); therefore, we have to determine which heating rate to use. The heating rate determined from the 660 cm^{-1} mode was chosen to use for two reasons. First, the 660 cm^{-1} has the smallest Stokes cross section. As previously described, a vibrational mode with a large cross section will exhibit greater optical pumping rates when compared to modes with smaller cross sections. As a result, the 660 cm^{-1} mode is most likely to be purely thermal, at least when compared to the other modes under consideration. The second reason for using the 660 cm^{-1} mode is it has the greatest purely thermal AS rate, due to it having the largest excited state population, as dictated by the Boltzmann distribution. The AS scattering rates are fitted using Equation 2.22a, where the 660 cm^{-1} mode is modeled as purely thermal but the additional modes have both optical and thermal contributions, Figure 2.19. For the three additional modes, a solid green curve is added to the plot to show the purely thermal contribution to the AS scattering rate; meaning, the additional curvature in the plot is due to the optical contribution. The additional curvature for the higher energy modes demonstrate that contributions are not thermal alone; therefore, they must be optical in nature. To determine the asymmetry factor (A_v) and anomaly coefficient (η_v), we fit the AS-to-S ratio using the expression given in Equation 2.22b. We have two unknowns to determine for each of the modes, excluding the purely thermal mode of 660 cm^{-1}. From the plots in Figure 2.20, we can determine the unknowns from the fitting parameters. A_v and η_v for the three higher frequency modes are given in Table 2.3.

As previously described by Equation 2.20, the optical contribution to the excited state population (N_1) is dictated by the mode dependent total Stokes cross section (σ_s^*). Having an accurate value of σ_s^* for each of the modes is a critical component to determining the anomaly coefficient (η_v). Figure 2.18 gives intensity dependent results for the Stokes scattering rates, where the red and blue points signify the forward and backward portions of the scan, respectively. The results suggest good signal stability when remaining within the marked intensities values, and an accurate measurement of σ_s^* is obtained from the fitted linear coefficient. The SERS Stokes cross sections taken from the fits are representative of cross sections reported in the literature.

Now that we have the total Stokes cross sections, we desire to find the total AS cross sections and the anomaly coefficients, η_v. The AS results in Figure 2.19 are fit using the expression,

$$R_{as} = aI_{\mathrm{n}}^2 + bI_{\mathrm{n}} \exp\left[-\frac{\hbar\omega_v}{k_B(T_0 + \kappa I_{\mathrm{n}})}\right] \tag{2.32}$$

where $I_n = I_n\,(\text{photons}\,\text{cm}^{-2}\,\text{s}^{-1})$ and coefficients:

$$\begin{aligned} a &= N_0\eta_v\tau_v\sigma_{as}^*\sigma_s^* \\ b &= N_0\sigma_{as}^* \end{aligned} \tag{2.33}$$

The quadratic coefficient incorporates the to-be-determined anomaly coefficient; therefore, we use the linear coefficient (b) in Equation 2.32 to calculate the σ_{as}^*. The heating coefficient, κ is a known parameter previously determined for each nantenna. As shown in Equation 2.33, σ_{as}^* is present in both fitting coefficients a and b. Although we do not know the exact number of molecules (N_0) contributing to the SERS signal, we know $N_0\sigma_s^*$ exactly from the Stokes fits. From high resolution SERS, we know the vibrational lifetimes (τ_v) for each mode of BPE; therefore, with relatively good certainty, we can deduce σ_{as}^* from coefficient a. The same logic applies for determining σ_{as}^* from coefficient b. The critical assumptions for determining σ_{as}^* from b are: $T_0 = 295\,\text{K}$ for $I_{\mathrm{n}} = 0$ and the heating rate κ determined from the 660 cm^{-1}

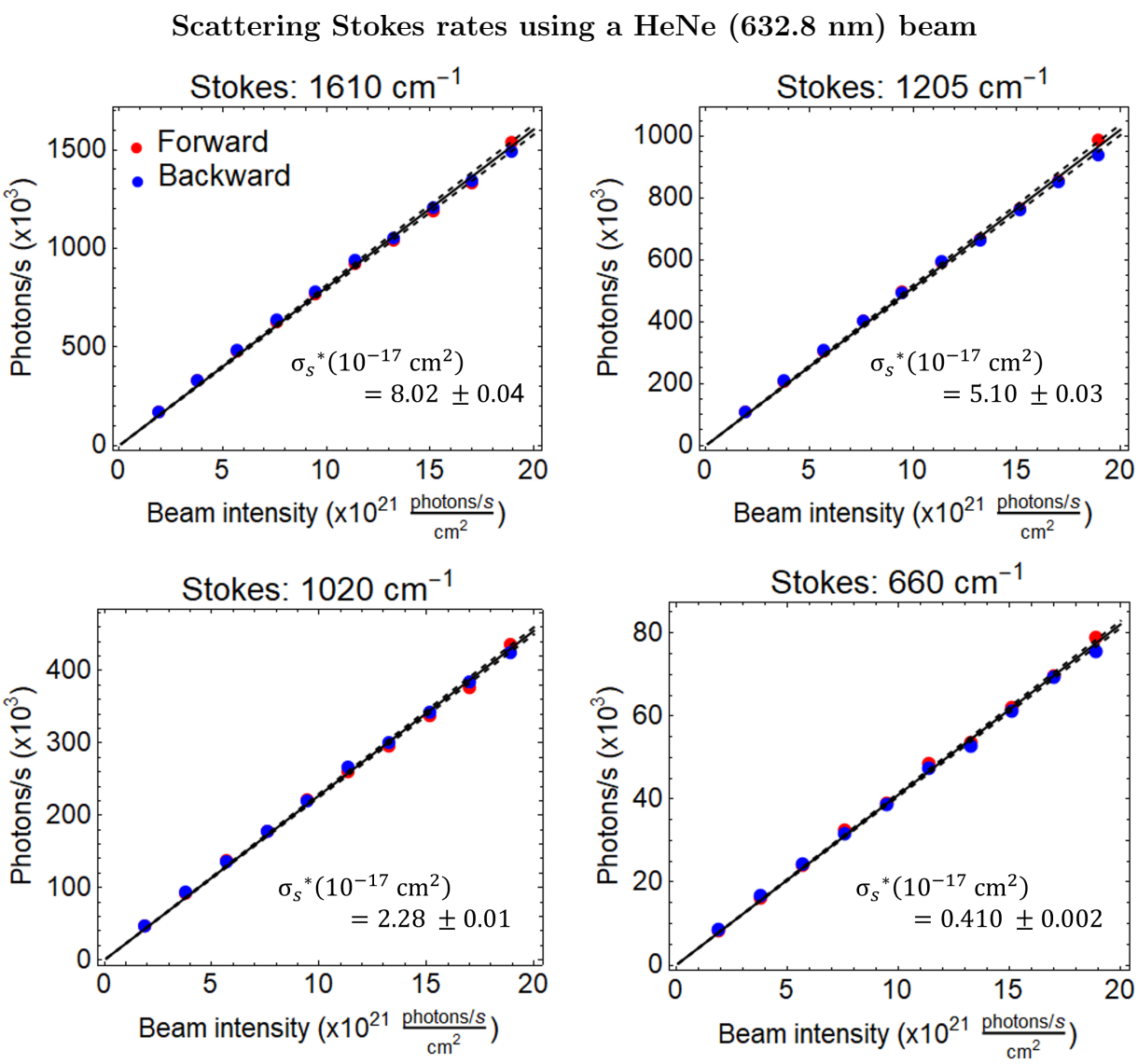

Figure 2.18: Integrated Stokes scattering rates when the input beam intensity is swept and the total Stokes cross section for each vibration obtained from the fitted slop. The results are fit to a line (solid black) to retrieve the Stokes total cross section. The dashed black lines show the 99% confidence intervals for the fit. The reported Stokes cross sections are not great enough to achieve optical pumping; therefore, a coherent process is needed to explain the enhanced AS rates.

Optical and thermal contributions to the AS rates the HeNe laser

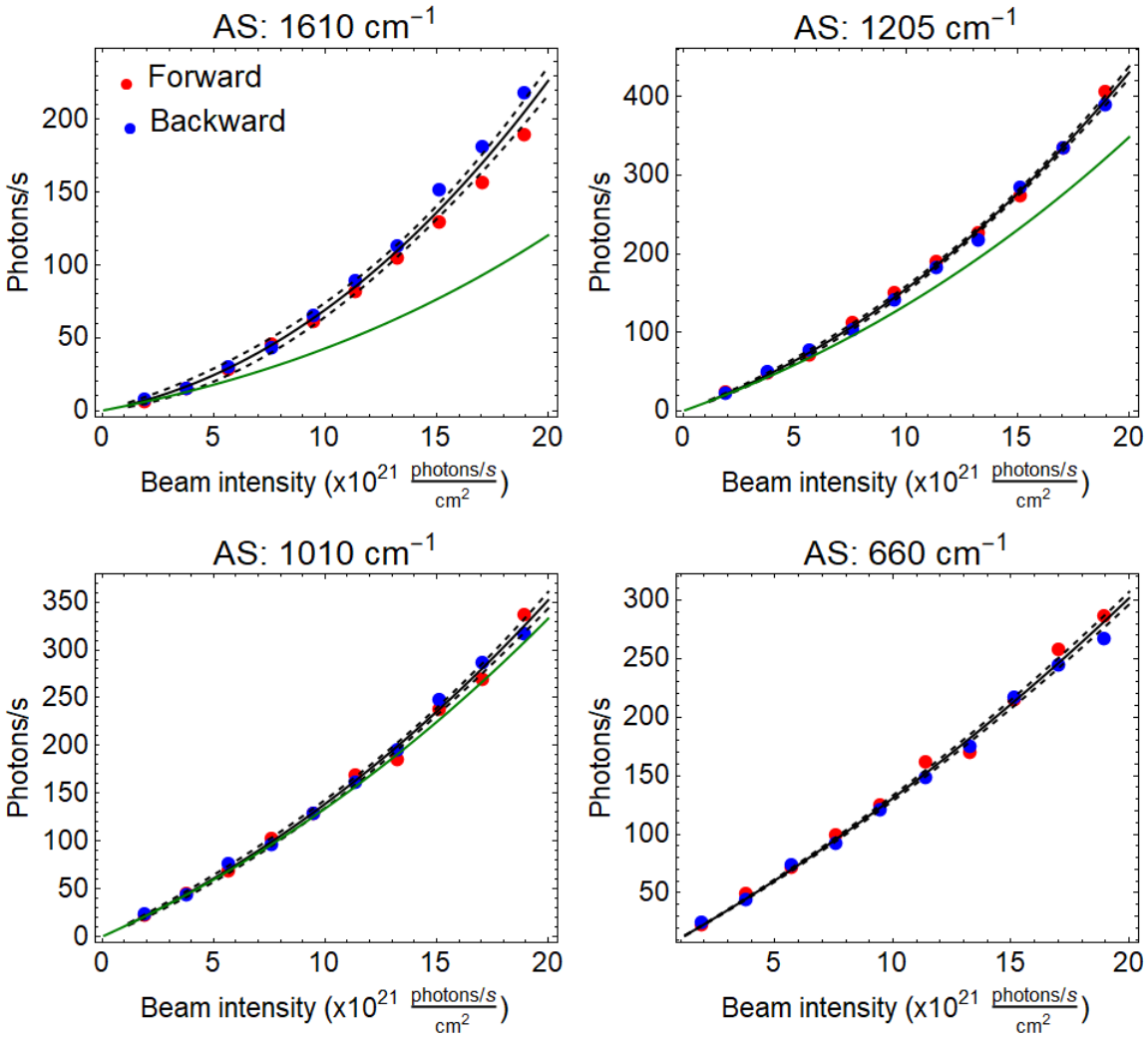

Figure 2.19: Measured results and fits (solid black) for AS scattering rates using the optical and thermal contributions and Equation 2.22a. The solid green curves in three of the plots show the curvature due to the thermal contribution. The deviation from the green curve is due to the optical contribution to the AS rates.

Table 2.4: Vibration dependent SERS AS cross sections from the fitted results in Figure 2.19 assuming $N_0 = 1$. The third column is the probability to find the vibration in v = 1 at T = 295 K

Mode (cm^{-1})	σ^*_{as} (10^{-17} cm^2)	$N_{v=1}$(T = 295 K)
1640	6.91	$0.34 \cdot 10^{-3}$
1610	9.77	$0.39 \cdot 10^{-3}$
1205	4.70	$2.81 \cdot 10^{-3}$
1010	1.99	$6.92 \cdot 10^{-3}$
660	0.364	$40.0 \cdot 10^{-3}$

mode. With these assumptions, we know every term contained in the exponential. We can now take the ratio of $N_0\sigma^*_{as,b}$ (from b) and $\sigma^*_{as,a}$ (from a) to potentially obtain a value for N_0. Upon taking the ratio, we find $\sigma^*_{as,a} > N_0\sigma^*_{as,b}$, which says we must place a prefactor (an anomaly coefficient, η_v) before $\sigma^*_{as,a}$ so that the inequality is physically reasonable.

The AS-to-S ratio curves can then be fit to verify results from the AS and Stokes fits. The ratio is described by Equation 2.22b and the AS-to-S results are then fitted using the expression,

$$R_{as/s} = A_v \left(\exp\left[-\frac{\hbar\omega_v}{k_B(T_0 + \kappa I_n)} \right] + \beta\, I_n \right) \tag{2.34}$$

where A_v has been previously defined and,

$$\beta = \eta_v \tau_v \sigma^*_{as} \tag{2.35}$$

The AS cross section (σ^*_{as}) is then calculated using β. The AS cross sections, from one of the nantennas, are displayed in Table 2.5.

From the AS results, we see the linear coefficient returns an AS cross section which nearly matches the Stokes cross sections. We use the AS cross section from the linear coefficient best fit, because in spontaneous Raman, the AS cross section is directly proportional to the slope in the AS rates versus input intensity curve. The fitted results have been corrected for ω^3 scattering, so we expect AS and Stokes cross sections which match one another (assuming

Optical and thermal AS-to-S ratio using a 632.8 nm beam

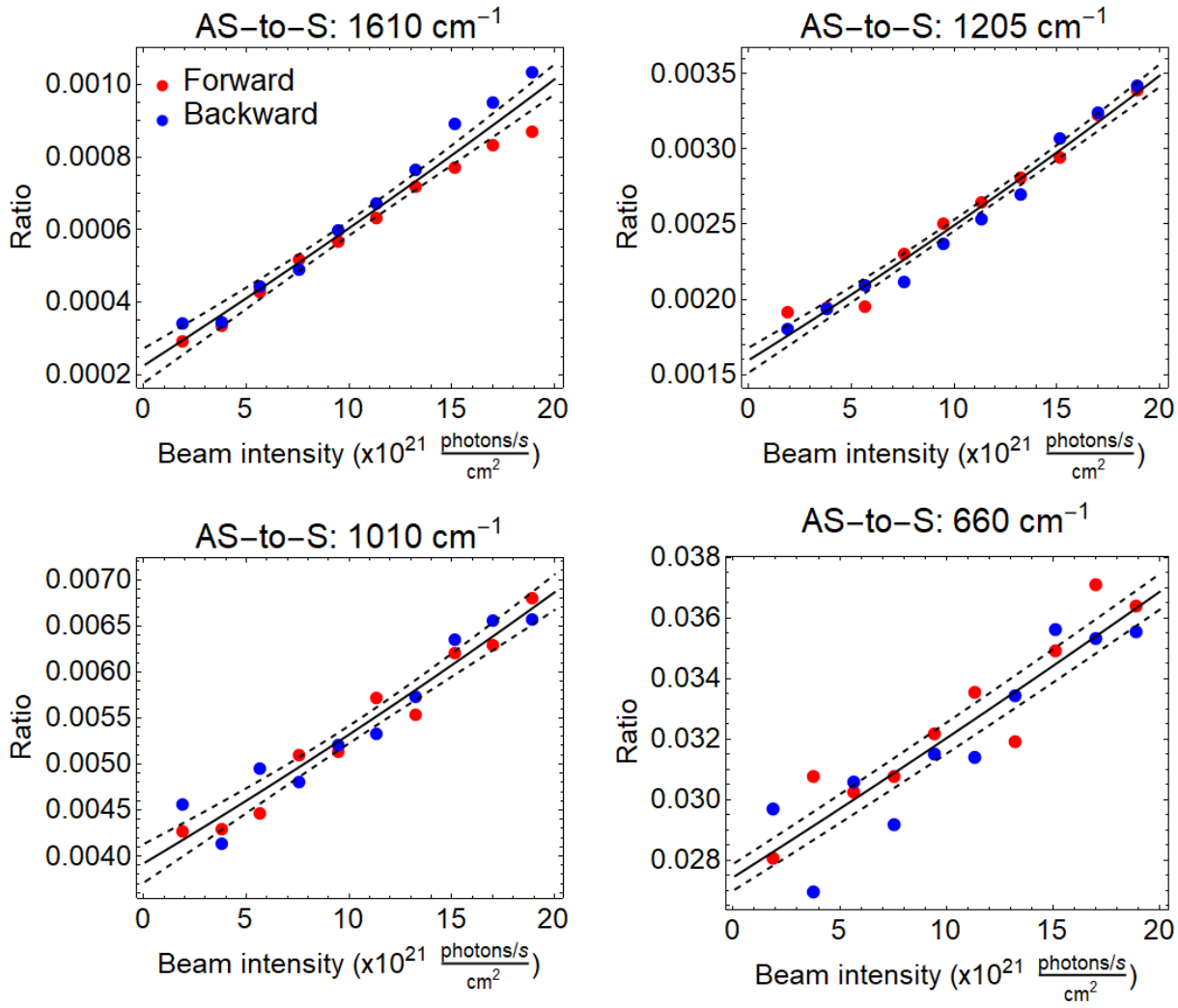

Figure 2.20: Curves and fits for the AS-to-S ratio when illuminating a nantenna with the 632.8 nm laser. The fitted curves assume the thermal and optical contribution model (Equation 2.22b); meaning, curvature which depends on thermal and optical dependence on input intensity.

Table 2.5: Mode specific SERS AS and Stokes cross sections from fitting AS-to-S curves using the 735 nm laser diode.

Mode (cm^{-1})	σ^*_{as} (10^{-16} cm^2)	σ^*_s (10^{-16} cm^2)
1640	15.0	6.79
1610	16.9	6.95
1335	2.88	1.71
1205	8.57	7.23
1010	2.70	2.80
660	0.35	1.96

Table 2.6: Mode specific SERS AS cross sections measured from the same nantenna using 632.8 nm and 735 nm laser sources. The results show the improved AS scattering achieved when using the laser diode (735 nm) as the pump source.

Mode (cm^{-1})	$\sigma^*_{as,633}$ (10^{-16} cm^2)	$\sigma^*_{as,735}$ (10^{-16} cm^2)
1640	1.47	15.0
1610	1.92	16.9
1335	0.38	2.88
1205	1.03	8.57
1010	0.36	2.70
660	0.083	0.35

equivalent enhancement factors). Not surprisingly, the intercept coefficients from the linear fits to the AS-to-S curves also return reasonable AS cross sections. Again, the values are in nice agreement with the values taken from the linear coefficient in AS fits. We desire to investigate the anomalous AS scattering further and employ a 735 nm laser diode as the pump source. Intensity dependent BPE SERS spectra are measured using the laser diode and the resulting curves are displayed in Figure 2.21. Stokes cross sections are taken from linear fits and are compared to the cross sections obtained using the HeNe laser (Table 2.6). We see the cross sections are greater when using the 735 nm pump source, phenomenon that is consistent over the bulk of nantennas investigated.

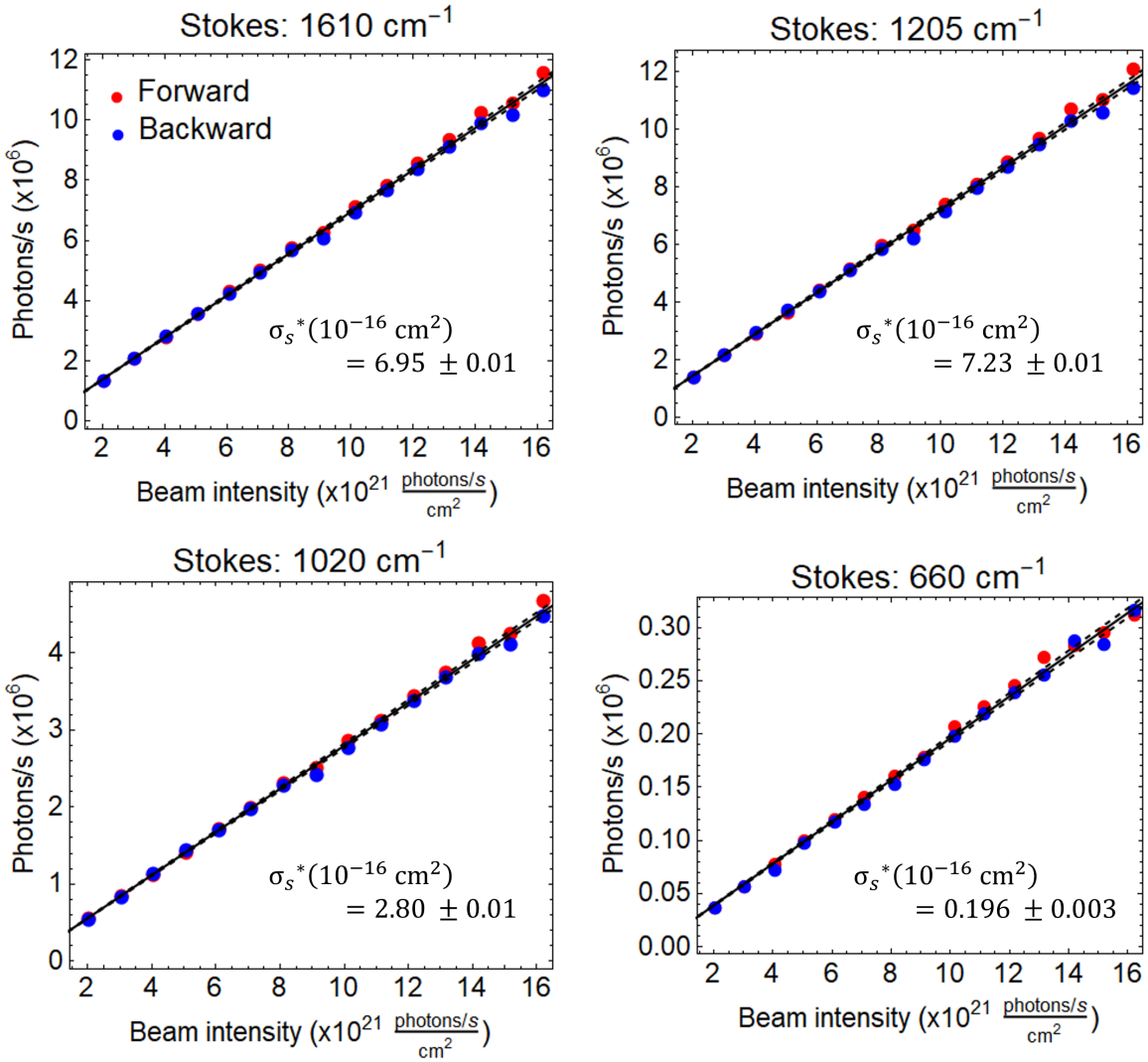

Figure 2.21: Integrated Stokes scattering rates when the input laser diode (735 nm) intensity is swept. The results are fit to a line (solid black) to retrieve the Stokes total cross section. The dashed black lines show the 99% confidence intervals for the fit. Like the results for 633 nm, the reported Stokes cross sections are not great enough to achieve optical pumping; therefore, a coherent process is needed to explain the enhanced AS rates.

Optical and thermal contributions to the AS rates using a 735 nm beam

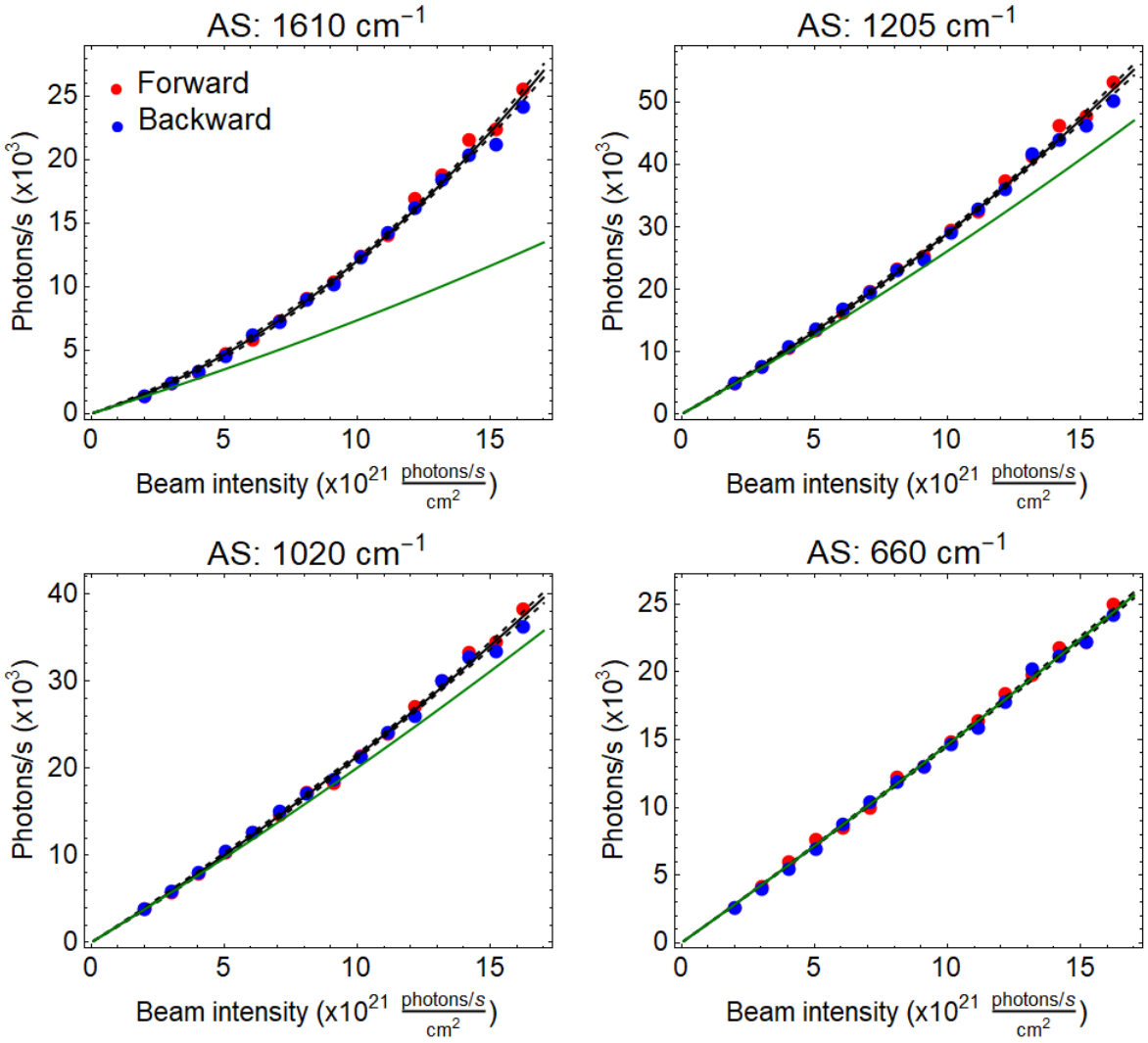

Figure 2.22: Measured results and fits (solid black) for AS scattering rates using the optical and thermal contributions and Equation 2.22a. The solid green curves in three of the plots show the curvature due to the thermal contribution. The deviation from the green curve is due to the optical contribution to the AS rates.

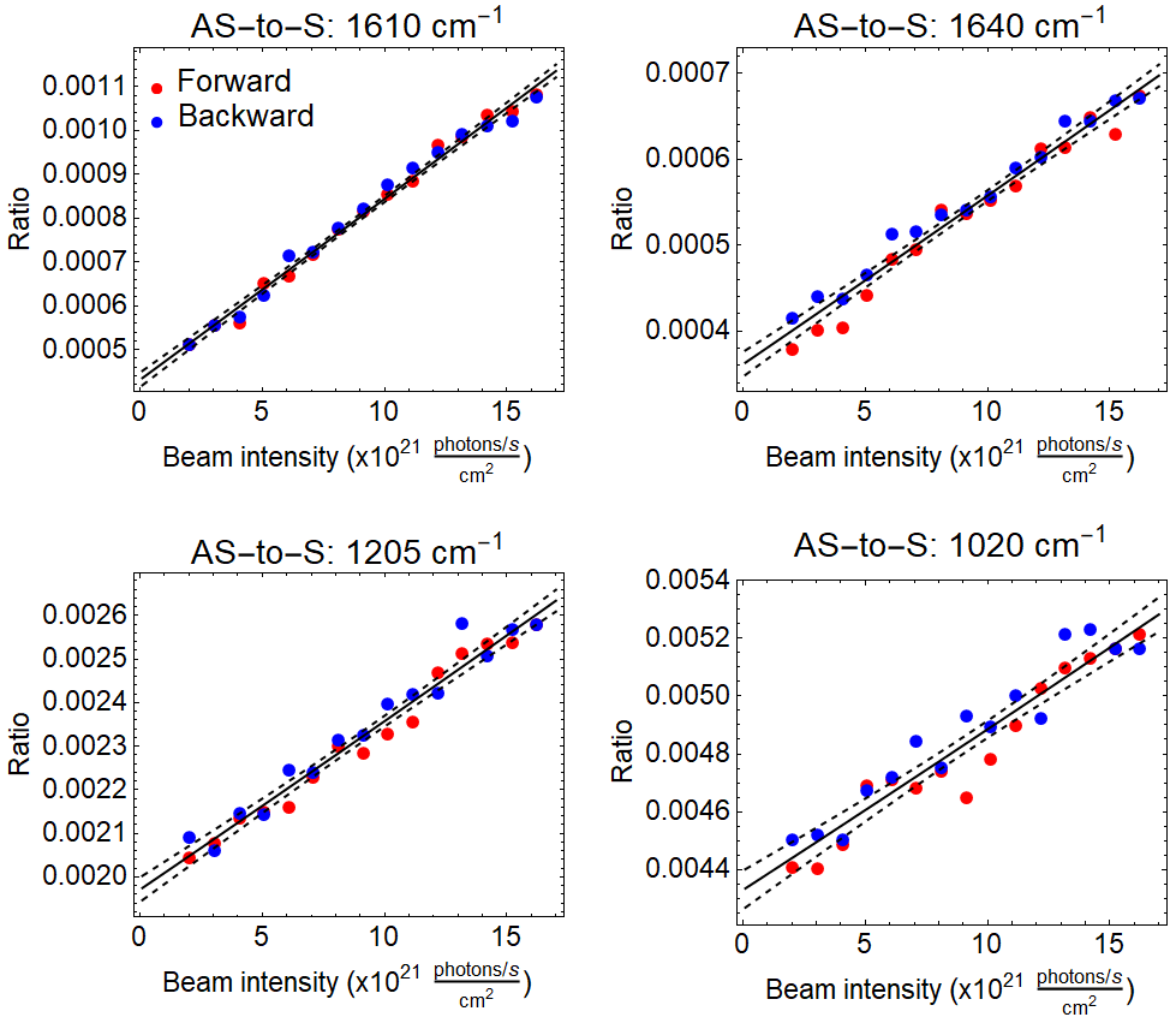

Figure 2.23: Mode specific AS-to-S ratios when using the laser diode (735 nm) as the pump source, modeled using thermal and optical contributions, Equation 2.22b. When comparing the results to those measured using the HeNe, we consistently see larger ratios for the majority of nantennas tested. This says that the optical contribution to the signal is more pronounced when using the laser diode.

Table 2.7: Heating rates determined using the 660 cm^{-1} mode for four individual nantennas. As previously mentioned, the vibrational modes must heat at the same rate; therefore, the reported values in this table are used for all Raman modes.

Nantenna	κ_{633} $(10^{-21}$ $\frac{\mathrm{K\,cm^2}}{\mathrm{photons\,s^{-1}}})$	κ_{735} $(10^{-21}$ $\frac{\mathrm{K\,cm^2}}{\mathrm{photons\,s^{-1}}})$
98	0.23	0.42
99	0.86	0.48
101	0.55	0.38
104	1.31	0.61

2.8 Nantenna dependent asymmetry factors and anomaly coefficients

Early results suggested larger anomalous contributions to the AS rate when using a 632.8 nm pump source, so we collected intensity sweep measurements using both the HeNe and laser diode sources for several nantennas. First, we found the heating rate, κ, is not strongly dependent on pump frequency, Table 2.7. Our results show larger nantenna-to-nantenna variation when using the same pump frequency than they show for differing pump frequencies. In other words, we see less variation when switching pump frequencies than we do when switching nantennas. This point is clarified by the histogram in Figure 2.24. We see the maximum number of occurrences fall between heating rates of $0.4 - 0.6 \cdot 10^{-21}\,\mathrm{K\,cm^2\,s}$, for both laser beams. Also, we see heating rates vary substantially around the maximum occurrence range of values. For the limited amount of nantennas tested, we do not see a conclusive pump frequency dependence in heating at the nanojunction. This statement is important because it suggests the increase in AS rates, when using the laser diode, is due to the optical contribution. The optical contribution manifests itself through both the asymmetry factor, A_v, and the anomaly coefficient, η_v. Both values for each mode can be obtained by fitting the AS rates and AS-to-S ratio curves. To see how pump frequency affects A_v and η_v, we compare intensity sweep measurements from four nantennas in Figures 2.25 and 2.26.

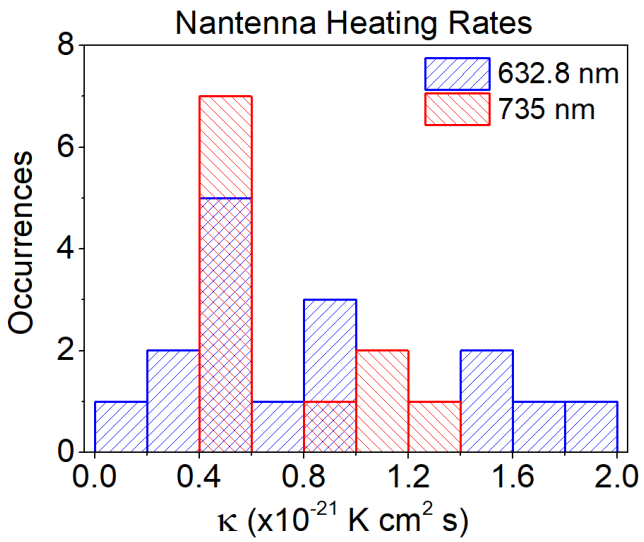

Figure 2.24: Histogram showing heating rate occurrences when using both pump frequencies. We see the maximum number of occurrences falls in the range $0.4 - 0.6 \cdot 10^{-21}$ K cm^2 s, for both pump sources. The histogram shows that heating rates depend more on the nantenna under investigation, and less on the pump source used.

First, we consider the results for A_v, Figure 2.25, for possible mode specificity. Variations in A_v among the different vibrations may have a plasmon resonance dependent spectral origin, or a chemically enhanced mode specificity. There are some clear trends in the data. Note, $A_v = 1$ means no asymmetry; that is, the AS-to-S ratios are the same as in the free molecule. At 632.8 nm, the factors are consistently smaller than one, in all four particles they fall in the range of 0.4 ± 0.2, increasing toward the smaller vibrational shifts. At 735 nm, values for A_v are generally greater than one, show a similar 50% spread in values, and a valley near the middle of the range. The consistent trend, $A(632.8) < 1 < A(735)$ is global, clearly, not mode-specific. Also, the general trend of valley versus a mild linear dependence cannot be mode specific, which by definition requires vibration specific variation to be independent of the excitation wavelength. The dominant effect in the asymmetry comes from the variation in the spectral dependence of the enhancement factors, as postulated at the onset. Nevertheless, there is also evidence for mode specificity. This is evident in the pair of C=C stretching lines near 1600 cm^{-1}, which are separated by 35 cm^{-1}. The variation in A_v between these two lines is as large as the full range of the data at 633 nm, less at 735 nm. Given the

absence of a clear trend, and that plasmon resonances are an order of magnitude broader than the separation between the doublet modes, it is concluded that the fluctuation in A_v over narrow frequency bands is a mode specific chemical effect, due to the adsorption site of the molecule and nanocavity geometry. Modes are selectively enhanced due to the position of the molecule in the nanojunction. Raman scattering intensity is stronger when the vibration becomes more polarizable, due to inductive charge coupling between molecule and metal. Also, orientation of the molecule relative to local field and field gradient can lead to mode specific enhancement. If the polarizability tensor for a normal mode of the molecule better aligns with the input and scattered fields, the Raman rate increases.

Now that we have addressed mode specificity, we turn our attention to pump frequency dependence. We see from our curves for A_v, that measured results are highly dependent on the pump laser. The clear excitation wavelength dependence of the asymmetry factor, $A_v(633) < 1 < A_v(735)$, appears to be correlated with the Stokes SERS cross sections, $\sigma_s(633) < \sigma_s(735)$. This tells us that the AS SERS cross section is significantly larger when using the laser diode, as compared to results using the HeNe. This corroborates that the anomaly is optical in origin, and that the effect grows with increasing scattering efficiency.

We turn our attention to the anomaly coefficient, η_v. As with A_v, it can be seen that η_v is vibration dependent, Figure 2.26. The error bars signify the 66.7% confidence intervals for the reported value (solid marker). The error bars are relatively large for some of the modes, $\sim 30 - 50\%$ of the reported value. The relatively large uncertainty is partly a consequence of the double pass intensity sweep utilized for data collection. Due to slight signal degradation, the reported value for η_v for the two sweep directions differs. This is a determinant uncertainty in the results. If we report values and uncertainties for the single direction sweeps, we see uncertainties that are smaller than shown in Figure 2.26. Again, we see values for η_v that vary rapidly with respect to frequency (Figure 2.26); therefore, we do not expect the coefficient to be dominated by the plasmon resonance. Similar to A_v, we see values for η_v that are highly

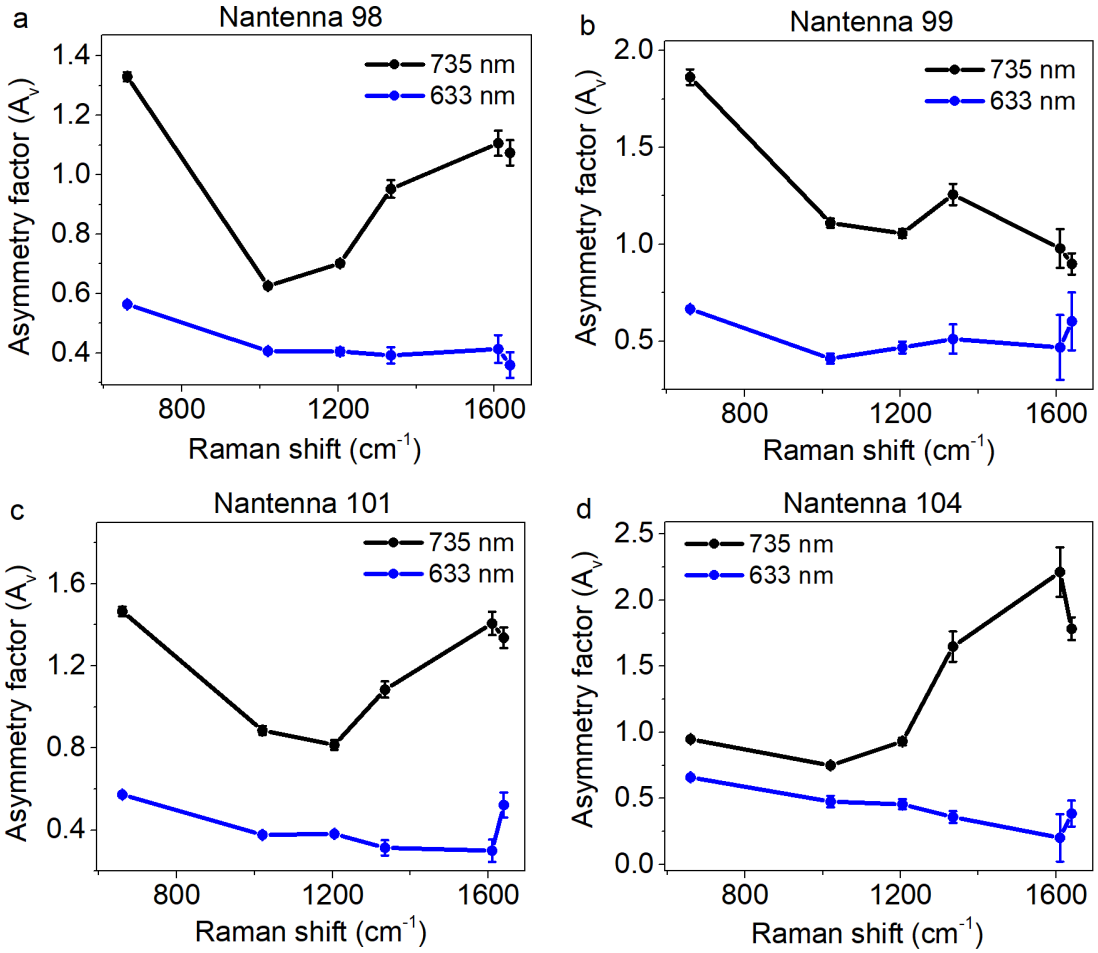

Figure 2.25: Measured asymmetry factors for four nantennas using the 633 and 735 nm lasers. Asymmetry factors are determined by fitting the AS-to-S ratio results using both intensity dependent thermal and optical contributions. The vertical bars signify the 95% confidence interval for the reported value. For certain data points, the height of the vertical bars are smaller than the marker used to signify the asymmetry factor value.

dependent on the nantenna. As before, it can be suspected that the orientation of the BPE molecule in the nanocavity plays a significantly role in the reported values for η_v.

From the curves for η_v, we again see significant pump frequency dependence. For 735 nm, we see larger values for A_v affect the anomaly by lowering its magnitude; meaning, a smaller η_v is needed to model the results because the increase in the AS enhancement factor is providing additional signal intensity. For HeNe, A_v is smaller; therefore, the AS enhancement factor is smaller. To accurately model the HeNe results, η_v must take on values that are larger by one order of magnitude. To make the pump frequency dependence for η_v clearer, we plot measured curves using both lasers on the same graph, Figure 2.26c. We see η_v values for the $\sim$1620 cm^{-1} doublet, when using the HeNe, begin to approach the η_v values for 1020 cm^{-1} obtained using the laser diode. This suggests to us that η_v values begin to merge in the region of $710 - 790$ nm. Note, the spectral variation is mild under 735 nm excitation and dramatically increases toward the smaller Stokes shifts under 633 nm excitation (Figure 2.26). By plotting the data as a function of Stokes wavelength, the curves obtained using both pump sources can be combined (Figure 2.26c).

2.9 Sequential optical excitation cannot explain the data

We observe enhanced spontaneously scattered AS photons when illuminating our nantennas with cw lasers. By enhanced, we mean AS count rates which are greater than expected for a combination of thermal population and optical pumping [50–53, 59]. The sequential mechanism of AS scattering, namely the preparation of v = 1 population by Raman scattering and its subsequent re-excitation is described by Equation 2.22a. All variables that appear in the equation are experimentally determined, including: the heating rate constant, κ, which is

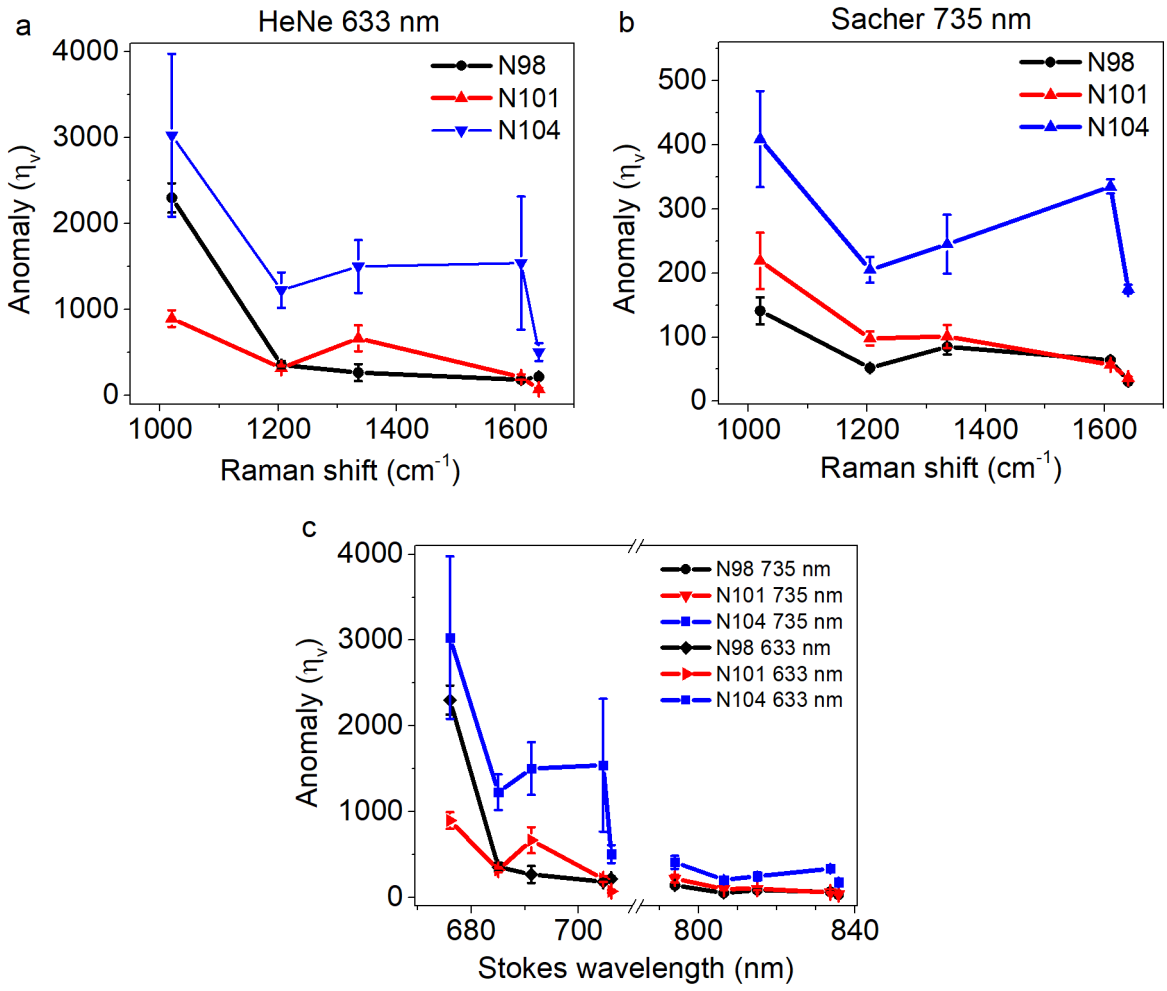

Figure 2.26: Measured anomaly coefficients (η_v) for three nantennas using the 633 and 735 nm lasers. Anomaly coefficients are determined by fitting the AS-to-S ratio results using both intensity dependent thermal and optical contributions. The vertical bars signify the 66.7% confidence interval for the reported value. For some data points, the height of the vertical bars is smaller than the marker used to signify the anomaly coefficient.

well determined subject to the constraint that a single temperature describes the vibrational population, σ_s^*, which is directly obtained from the Stokes count rates, the vibrational lifetime (τ_v), which is determined by linewidths (and through time-resolved measurements described in the next chapter). To bring the data into agreement with this mechanism, it is necessary to introduce the asymmetry and anomaly factors factors, A_v and η_v, respectively. The former can be understood as the spectral shifts of AS and Stokes lines relative to the broad plasmonic resonance, and the effect is a factor of order $\sim$2 (or 0.5). The dramatic deviation is the anomaly factor, which is of order 10^3 and cannot be explained in the sequential excitation mechanism. We are led to propose that the AS scattering is dominated by coherent anti-Stokes scattering (CARS), in which the second photon acts on the coupled molecule-plasmon coherence, with significantly larger polarizability than the molecule alone. The unusual aspect of this assignment is that it is a single beam process, in contrast with the standard scheme that requires injection of both pump and Stokes photons. In CARS, the Stokes transition is stimulated. A single beam SE-CARS would imply that the plasmon mediated pump photon stimulates the Stokes transition, as we expand in the next chapter.

Chapter 3

SECARS from individual plasmonic nantennas

3.1 Introduction

From the Chapter 2, we introduced the concept of impulsive stimulated single-beam SECARS. Briefly, a pump photon promotes the vibration to the excited state, while also exciting the localized plasmon resonance. There is now charge motion in the metal (gold) and the surrounding dielectric (silica). The impulsive plasmon driver may be thought of as the localized surface plasmon analogy to the surface plasmon polariton. The impulsive plasmon resonance is short in time and broad in frequency. The broad plasmon resonance has photons throughout the Stokes frequencies that can stimulate the vibrations to the excited state, instantaneously. A coherence is now formed between the ground and excited states. Then, a second pump photon scatters from the excited state and is detected via a spontaneously emitted AS photon.

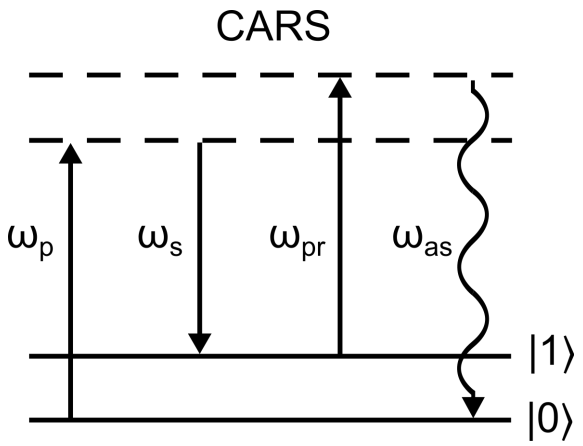

Figure 3.1: Jablonski diagram for CARS. Pump (ω_p) and Stokes (ω_s) photons instantaneously excite and stimulate a molecular vibration, creating a coherence between the ground ($|0\rangle$) and excited ($|1\rangle$) state. A probe photon (ω_{pr}) then acts to probe the coherence, which is ultimately observed through the coherently prepared, spontaneous anti-Stokes photon (ω_{as}).

Coherent Anti-Stokes Raman Scattering (CARS) at plasmonic nanojunctions has received much attention throughout the years due to its increased scattering rates [70–72] and single molecule sensitivity [29, 73, 74]. Surface-enhanced CARS (SECARS) has been successfully implemented for biological imaging, single-molecule detection at nanoparticle junctions, and tip-enhanced scattering at a tip-planar junction. CARS is a parametric four photon process that results in a signal field generated at frequency ω_{as}, depicted in Figure 3.1. In CARS, the pump (ω_p) and Stokes (ω_s) fields interact with the sample and generate an anti-Stokes (AS) signal at $\omega_{as} = 2\omega_p - \omega_s$, without depositing energy in the sample.

3.2 Methods

3.2.1 ps Intensity-dependent SERS measurements

The ps intensity-dependent SERS measurements are collected in a fashion almost identical to the cw case. The differences between the two measurements will be mentioned here. For the 735 nm measurements, the signal beam of the OPO is used, while for the 633 nm excitation,

the doubled idler beam is used. Either ps laser beam is the guided to a conventional inverted microscope converted to perform transmission-type spectroscopy. This is accomplished by fitting a low NA (10x, 0.25 NA) objective lens (i.e. top objective) to the condenser holder using an adapter, resulting in an upright microscope. The laser beam is elevated to the top objective using a periscope and is focused on the ITO substrate/nantenna plane. Raman scattered photons are then collected using an objective lens (60x oil, 1.25 or 1.42 NA) and reflected to the spectrometer and CCD camera. This geometry is chosen to give low input intensities while maintaining high objective collection efficiency. The previously mentioned automated program is then used to collect the intensity-dependent results.

3.2.2 Picosecond CARS spectroscopy

The 1,2-Bis(4-pyridyl)ethylene (BPE) functionalized silica-coated gold nantenna sample is transferred to a conventional inverted optical microscope interfaced with a tunable optical parametric oscillator (picoEmerald OPO, A.P.E.) pumped using the second harmonic of a 1031 nm fiber laser (NKT aeroPulse). A coincident pair of 2 ps, 80 MHz pulse trains are used for the ps-SECARS measurements. The depleted fundamental beam at 1031 nm serves as the Stokes pulse, while the tunable OPO signal beam (700-950 nm) performs as the pump and probe pulses. In part to eliminate backlash, the pump beam sweeps from low to high wavelengths, or equivalently, from high to low Raman shift. The Stokes and probe pulses are on motorized, software-controlled time-delay stages to ensure time-zero overlap among pump, Stokes, and probe pulses. The pump and Stokes beam combination generates difference frequencies spanning from 1550 to 1660 cm^{-1}, which covers the spectrum of the bright C=C modes. The pump, Stokes, and probe beams are overlapped temporally and spatially and are focused on the sample plane using an oil-immersion objective lens (0.65 or 1.25 NA). The collinear beams are focused onto the ITO coverlip-nantenna interface using a microscope objective lens (60x oil, 0.65 or 1.25 NA). At each frequency increment, CARS

signal in the epi-direction is collected and is reflected using a long-pass 801 nm dichroic beamsplitter to a grating imaging spectrometer (Andor Shamrock 500i) equipped with a 1600x200 element TE-cooled CCD detector (Andor Newton 970). Additional attenuation of the Rayleigh scattered light is blocked using an 800 nm short pass filter. The signal to noise is enough that no electron multiplying is required, and the detector is used in its conventional mode. The CCD is cooled to $-80\,^{\circ}\mathrm{C}$ to keep the dark counts at a minimum.

3.2.3 Picosecond CARS time-domain sweeps

We also carry out time-resolved SECARS measurements on the individual nantennas using the same 2 ps laser source. The typical CARS experiment probes the C=C stretching modes near 1600 cm^{-1}. For example, a CARS measurement will use pump ($\lambda_{pu} = 884$ nm), Stokes ($\lambda_{st} = 1031$ nm), and probe ($\lambda_{pr} = 884$ nm), for a difference frequency of, $\omega_{pu} - \omega_{st} = 1613$ cm^{-1}. The anti-Stokes photons are collected in the epi-direction. The pump (884 nm) and Stokes beams are initially time-overlapped and travel collinearly to an oil-immersion lens (NA = 1.25). The two beams are focused on a silica-coated gold nantenna functionalized with BPE molecule. The CARS scattered light from the nantenna is collected using the same objective and is directed to a 500 mm focal length Andor spectrometer fitted with an Andor Newton EMCCD. The spectrometer allows us to obtain a spectrogram of the scattered radiation and allows us to integrate over the portion of the CCD which detects the CARS signal.

The CARS time-sweep is performed by scanning the stage at constant velocity to the final stage position (i.e. the final time delay value). Once the stage reaches constant velocity, a trigger pulse is sent to the camera to begin a single acquisition. Once the single acquisition completes, the CCD sends a "Fire" pulse to the program and the program immediately queries and saves the current position of the stage. Immediately, we see there is a slight

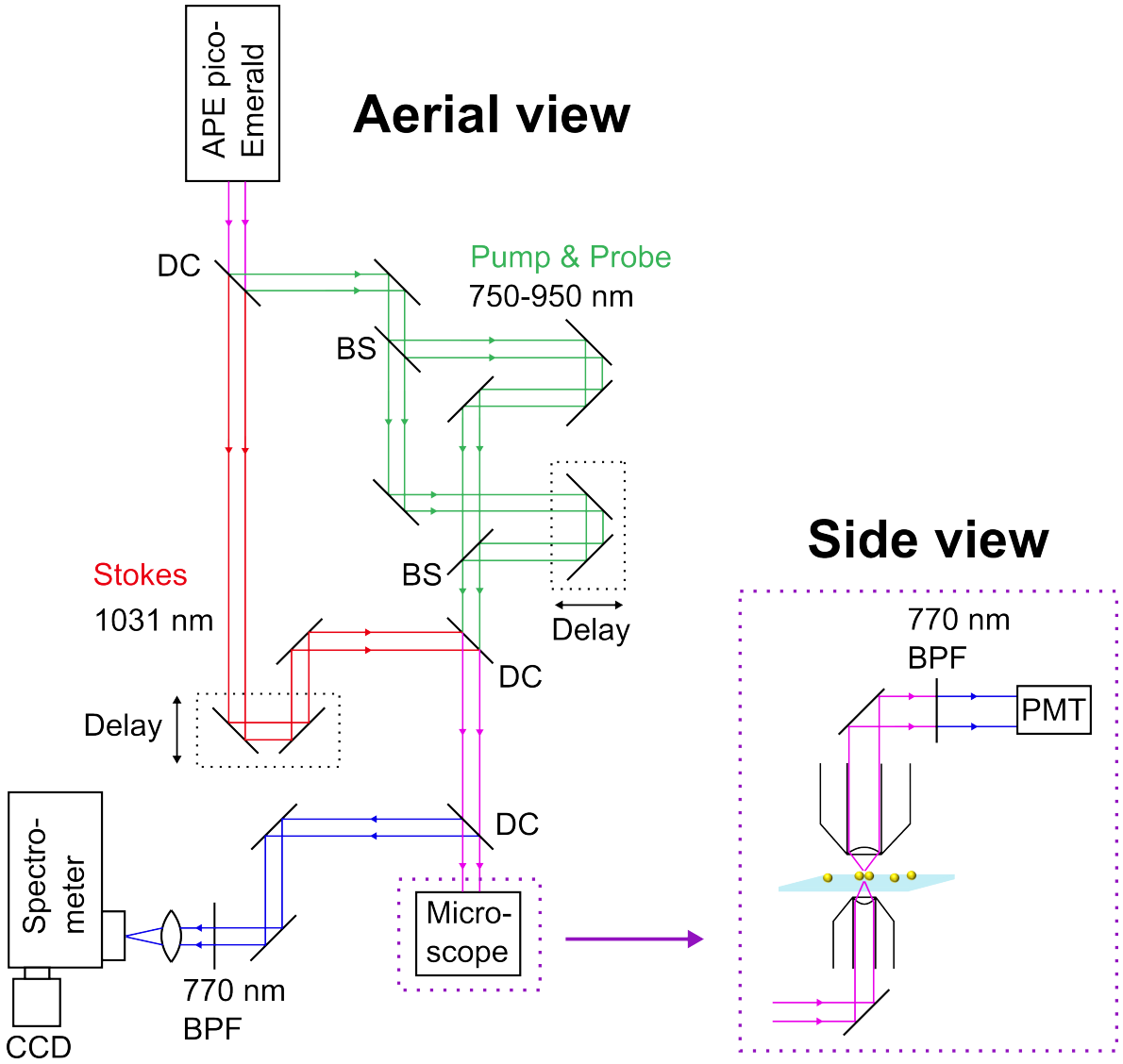

Figure 3.2: Surface-enhanced coherent anti-stokes Raman scattering (SECARS) incident and collection paths when using 2 ps pump, Stokes, and probe laser beams. The optical components: (DC) dichoric mirror, (BS) beamsplitter cube, (BPF) bandpass filter, (OL 1) incident objective lens, (OL 2) collection objective lens for forward scatter CARS detection, (PMT) photomultiplier tube, (CCD) camera detector. SECARS can be detected in both the forward and backscatter directions. Stimulated Raman scattering (SRS) can also be detected in the forward scatter using the proper components. Detecting SRS for a liquid (ex. Styrene or DMSO) in the forward scatter is an ideal method to ensure spatial and time overlap between the pump, Stokes, and probe pulses.

uncertainty in time from when the CCD ends its acquisition to when the computer marks the stage position, but this uncertainty would only introduce a constant offset to the time positions and would not cause linewidth broadening or narrowing.

3.2.4 Mapping individual nantennas for SERS and SECARS

The SECARS results presented in this chapter originate from individual clusters of nantennas at the sub-diffraction limit. To ensure that we are measuring SECARS from individual nantennas, we start by mapping the surface using scanning electron microscopy (SEM). Figure 3.3 shows SEM micrographs for the silica-coated gold nantennas. The regions are randomly chosen from a larger set of images meant to show typical nantennas at the surface of the substrate. From the micrographs, we see the number of particles making up the nantenna typically range from $2 - 10$ particles. The larger clusters are often composed of smaller clusters whose separation is dictated by the silica-coating thickness. The SEM micrographs are low-magnification, high pixel density images obtained using a FEI Magellan SEM.

Figure 3.4 shows forward-scatter (Rayleigh) detected optical images of the BPE nantennas. The bright sources correspond to nantennas that absorb the input laser (882 nm), while the background signal results from the unobstructed laser. In other words, the bright spots mean less laser is reaching the photodiode (PD) detector. The two images shown are the same except the right-side image contrast has been adjusted to better picture the lesser absorbing particles. I surmise that the weaker absorbing particles are gold monomers, or silica nanoparticles. From the SEM images, I know the surface is densely coated with pure silica particles. I emphasize the weaker absorbing particles because they also scatter molecular SECARS, albeit at larger input laser powers. The forward Rayleigh scattering optical images are collected by raster-scanning a piezo-driven stage over the focused 882 nm laser beam. A top-mounted objective lens is used to collect the transmitted beam and a silver mirror

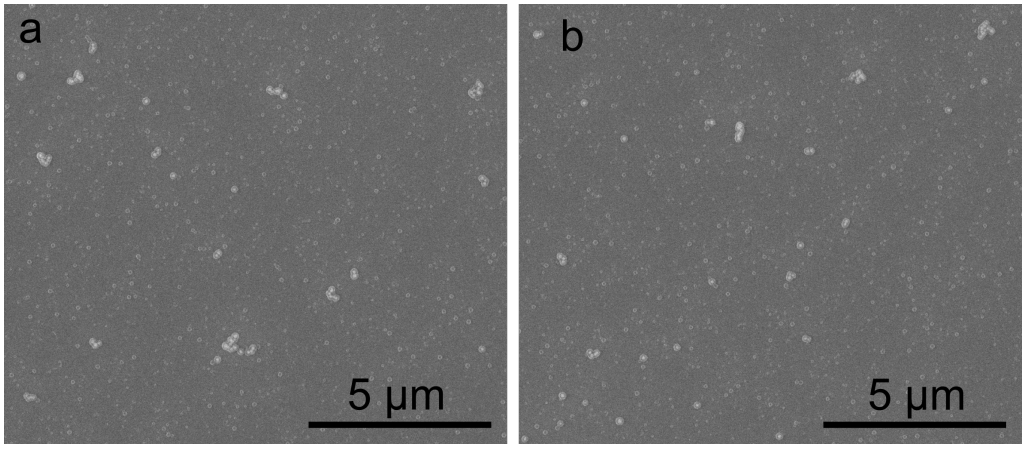

Figure 3.3: SEM images of BPE nantennas using the Magellan SEM. The images presented are randomly chosen areas, meant to illustrate the characteristic distribution of nantennas on the substrate.

reflects the light to a PD detector. The PD output is connected to a lock-in amplifier whose reference is set to coincide with the optical chopper frequency. The DC output from the lock-in is then used to construct the optical image.

3.3 Single-beam picosecond SECARS

In comparison to the cw measurements, at a given average intensity, excitation with the ps laser is expected to enhance the optical pumping channel, and diminish the thermal contribution. This is due to the higher peak power and reduced duty cycle offered by the ps laser, contributing to the optical and thermal contributions, respectively. To confirm our suspicions, we performed intensity sweeps and measured the Raman scattered light when illuminating the nantenna with a picosecond (ps) laser. If the AS rates are from a CARS process, then more nonlinearity should manifest when performing single-beam ps SERS. CARS will be more significant with a ps source because of the larger peak intensities. It is well known CARS scattering rates are proportional to peak intensities; therefore, ps SERS should result is more intense CARS scattering.

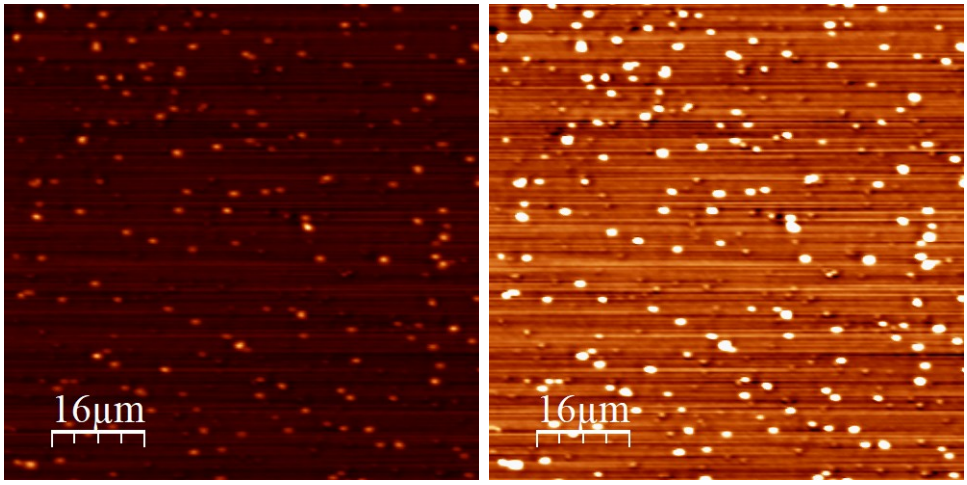

Figure 3.4: Forward Rayleigh scatter optical images for the nantennas on the ITO coverslip. Brighter sources signify nantennas that better absorb the input laser (882 nm). The two images are equivalent except the contrast in the right-side image has been adjusted to better picture the weaker absorbing particles.

Single-beam SECARS (SB-SECARS) depends on the bosonic plasmon resonance to stimulate the transition. Traditional CARS uses four interacting photon fields. For SB-SECARS, the interactions are: photon/plasmon, plasmon/photon, photon/plasmon, and plasmon/photon.

We report single-beam ps SERS spectra obtained by illuminating nantennas at 633.5 nm, Figure 3.5. Although the line-widths are broadened with respect to the cw excitation, we clearly see the characteristic BPE spectrum. To see how the Raman signal reacts to an external field, we sweep the laser intensity in forward and reverse directions and collect the AS scattered photons. We sweep the intensity in both directions to test for, and ensure, signal stability. We then integrate the detected signal under the four prominent Stokes lines and plot the results, Figure 3.6. The plots show the ps Stokes signal is proportional to input intensity and that the signal is adequately stable. From the fits in Figure 3.6, we extract the Stokes total cross sections, presented in Table 3.1. Interestingly, the ps Stokes total cross sections are measurably greater than their cw counterparts. Dependent on the nantennas being compared, ps total cross sections range from $2-4$ times greater than cw cross sections. Unfortunately, we did not collect ps and cw SERS from the same nantenna, so

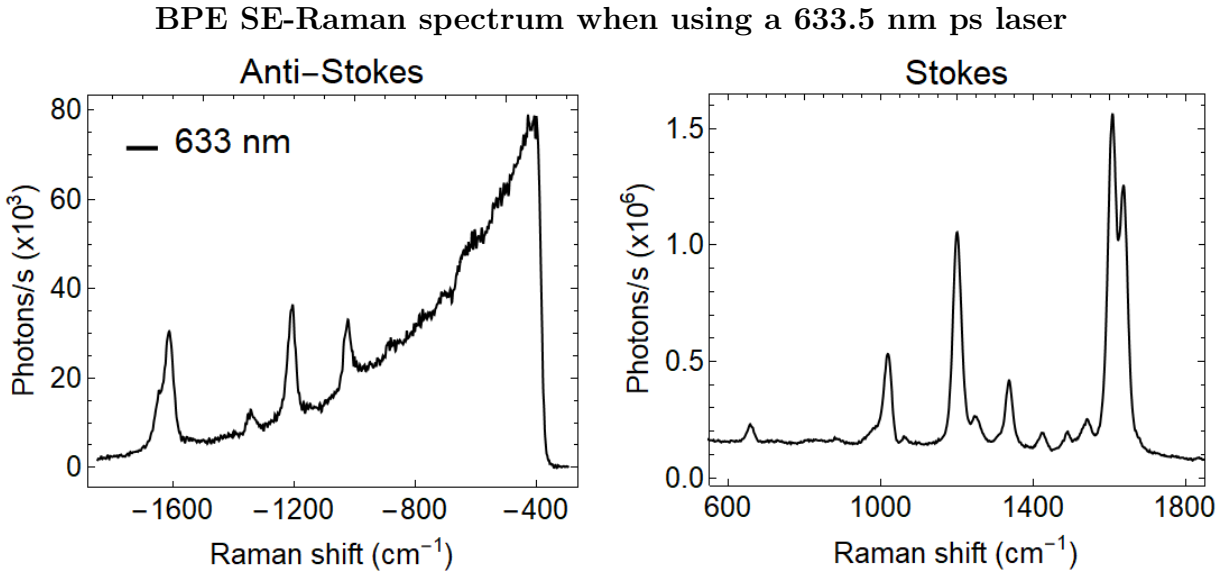

Figure 3.5: Anti-Stokes (AS) and Stokes single-beam SERS spectra when illuminating a nantenna with a ps laser (633.5 nm). Raman scattering is measured in a transmission geometry with excitation (NA = 0.25) and collection (NA = 1.42) objectives, and an input power of 24 μW. This yields a relatively low input intensity of $1.0 \cdot 10^{21}$ photons s^{-1} cm^{-2}. Compared to cw measurements, we see greater AS rates at lower average input intensities when using the ps source.

it is hard to make assertions from these results because cross sections can vary wildly from nantenna-to-nantenna. This is due to the significant dependence on the localized hotspot for each individual nantenna.

Our detection scheme allows for simultaneous Stokes and AS detection; therefore, we also plot the AS curves obtained from the intensity sweeps, Figure 3.7. The processed data is fitted to a second-order polynomial,

$$R_{as} = aI_n^2 + bI_n \tag{3.1}$$

due to the clear quadratic curvature in the AS rates. Interesting differences are noticed from the fitted AS curves, with respect to the cw results. First, we effectively retrieve a value of zero for the fitted linear parameter, b. The value retrieved from the fits for b is close to zero, and the standard error is large enough that we cannot report a reliable fitted value. For the

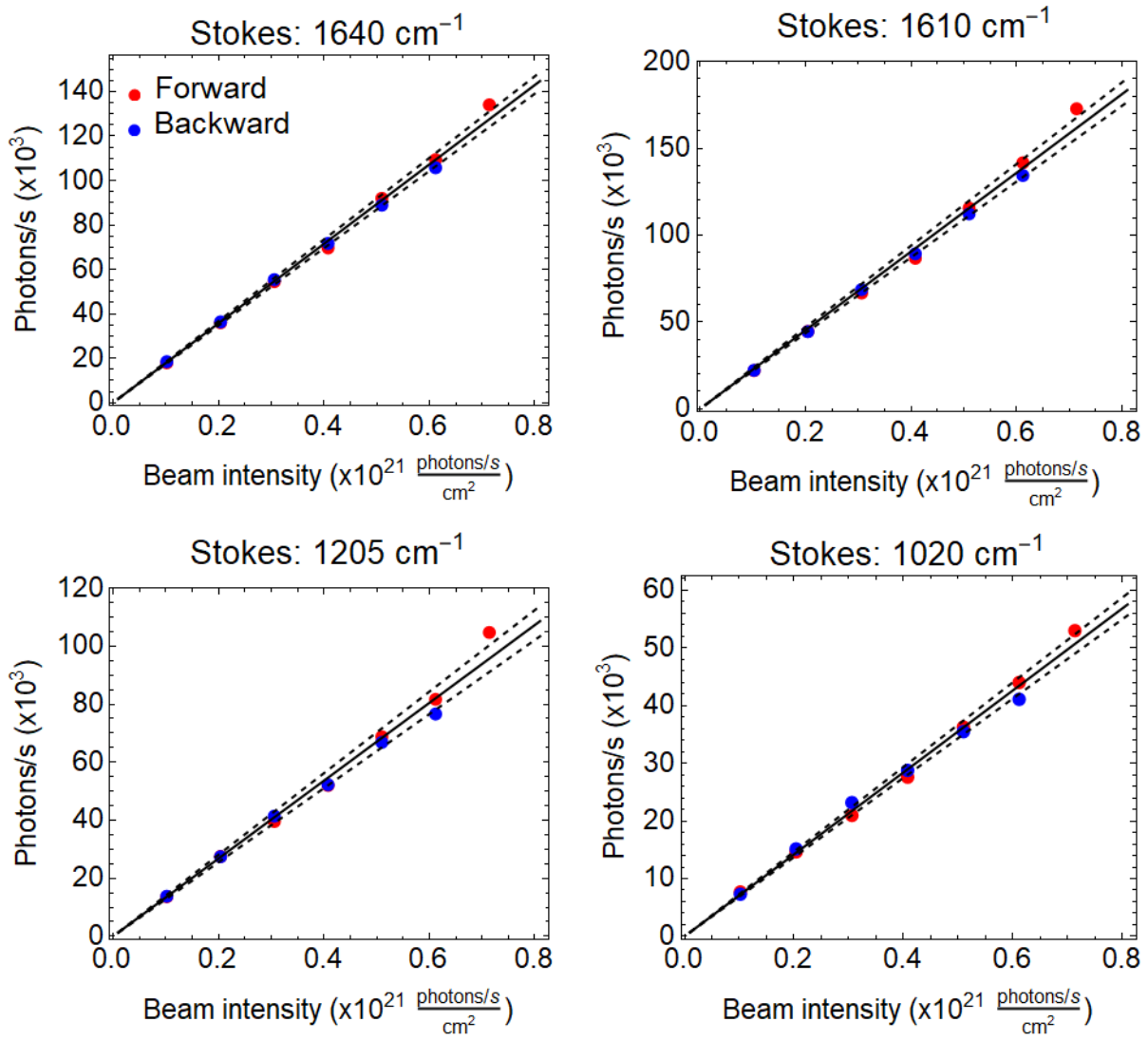

Figure 3.6: ps Stokes intensity sweeps using the 633.5 nm laser. The data points are fit to a linear function (solid line) and the confidence intervals are given (dashed lines).

Table 3.1: Stokes total cross sections (σ_s^*) for four prominent BPE modes obtained by fitting intensity sweeps to a line.

Particle	1640 cm^{-1} (10^{-16} cm^2)	1610 cm^{-1} (10^{-16} cm^2)	1205 cm^{-1} (10^{-16} cm^2)	1020 cm^{-1} (10^{-16} cm^2)
6	1.78 ± 0.06	2.27 ± 0.09	1.34 ± 0.07	0.71 ± 0.03
7	2.20 ± 0.07	2.62 ± 0.11	1.56 ± 0.07	0.68 ± 0.02
8	2.39 ± 0.10	2.82 ± 0.13	1.64 ± 0.09	0.77 ± 0.03
13	1.19 ± 0.08	1.42 ± 0.09	0.79 ± 0.08	0.41 ± 0.02

1640 cm^{-1} mode, $b = -0.20 \pm 0.33$, where a 95% confidence interval is used for the reported uncertainty. The fitted linear coefficient for the 1640 cm^{-1} mode has the smallest standard error, with respect to the three additional modes. Therefore, we cannot claim a reputable value for the linear coefficient for any of the four prominent modes observed in the ps SERS spectrum. The second difference noticed was the enhanced value for the quadratic coefficient, a, for the ps AS fits. For cw, a is $\mathcal{O}10^{-42}$, while for the ps results, values for a range from approximately $\mathcal{O}10^{-38}$ to $\mathcal{O}10^{-39}$. The solid green curves in Figure 3.7 show the expected AS rates when using the cw laser. The solid green line is the best fit to the cw AS rates assuming thermal and optical contributions, as previously discussed in Chapter 2. By displaying the cw results, we see the dramatic increase in AS scattering provided by the ps laser. The results suggest optical contributions account for the anomalous AS rates, and heating influences the rates slightly or not at all. We cannot unequivocally state that heating is contributing to the AS rates. Heating may contribute, but we need a more sensitive technique to measure the heating that may be present.

We are now interested in knowing the origin of the additional enhancement is the quadratic coefficient (a) for the ps AS fits; that is, we are interested in the $\sim 10^3 - 10^4$ difference between the cw and ps results. Is it due to the high peak intensities, or is the anomaly coefficient (η_v) enhanced compared to the cw case? In the following, we show the enhancement in coefficient a is a consequence of using ps lasers with large peak intensities. The transition rate for the ps SERS differs from the cw rate, and is described in the following. The peak intensity I_n^p is proportional to the average intensity I_n:

$$I_n^p = \frac{I_n}{\tau_p \nu_r} \tag{3.2}$$

Intensity dependent AS count rates for the 633.5 nm ps laser

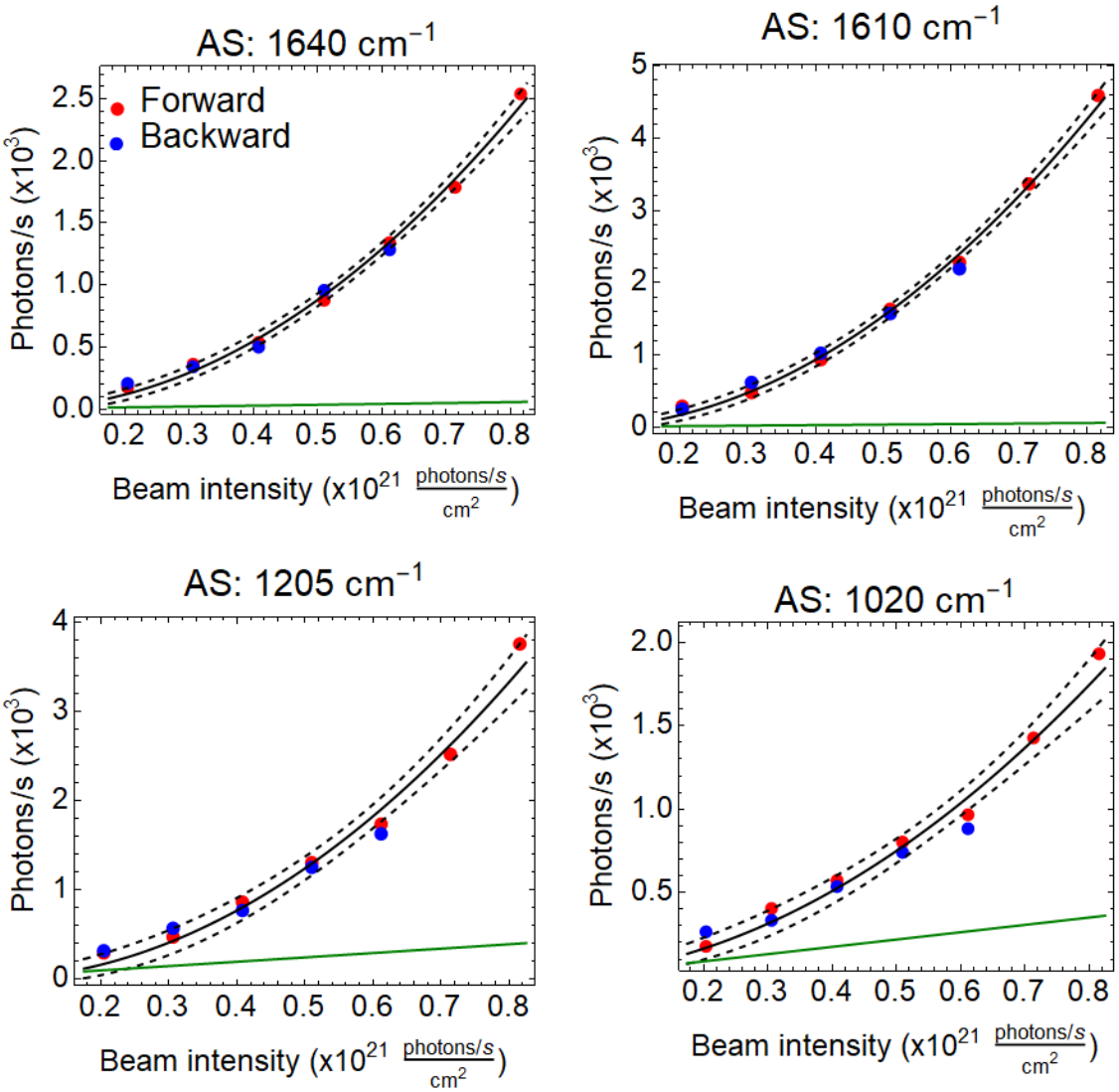

Figure 3.7: ps AS intensity sweeps using the 633.5 nm laser. The data points are fit to a second order polynomial function (solid line) and the confidence intervals are given (dashed lines).

where τ_p and ν_r are the pulse duration ($\sim$2 ps) and repetition rate (80 MHz) for the ps laser, respectively. The probability of exciting to the first vibrational state may be expressed by,

$$N_1 = N_0 I_n^p \sigma_s^* \tau_p \tag{3.3}$$

which can be defined as the $v = 1$ optically pumped population. The probability P_T to perform Raman on the $v = 1$ state to obtain AS scattering,

$$P_T = N_1 I_n^p \sigma_{as}^* \tau_v \tag{3.4}$$

where τ_v is the vibrational lifetime for the mode under consideration. To obtain an AS transition rate due to optical pumping (R_{as}), we must multiply the probability (P_T) by the repetition rate of the laser (ν_r). This gives the expression,

$$\begin{aligned} R_{as} &= P_T \, \nu_r \\ &= N_1 I_n^p \sigma_{as}^* \tau_v \nu_r \\ &= N_0 \, I_n^p \sigma_s^* \tau_p \, I_n^p \sigma_{as}^* \tau_v \nu_r \end{aligned} \tag{3.5}$$

Using $I_n^p = I_n / (\tau_p \nu_r)$, the expression can be simplified to,

$$R_{as} = N_0 \sigma_{as}^* I_n^2 \, \frac{\sigma_s^* \tau_v}{\nu_r \tau_p} \tag{3.6}$$

Finally, the thermal AS contribution is added. As noted before, it is not clear that the junction is heating; therefore, the overall rate is:

$$R_{as} = N_0 \sigma_{as}^* \left(\exp\left[-\frac{\hbar \omega_v}{k_B T} \right] I_n + \frac{\sigma_s^* \tau_v}{\nu_r \tau_p} \, I_n^2 \right) \tag{3.7}$$

and the AS-to-S (ρ) ratio for ps illumination becomes:

$$\rho = A_v \left(\frac{\omega_{as}}{\omega_s}\right)^3 \left(\exp\left[-\frac{\hbar\omega_v}{k_B T}\right] + \frac{\sigma_s^* \tau_v}{\nu_r \tau_p}\, I_n\right) \tag{3.8}$$

As stated, we want to determine whether the additional curvature in the AS rates is due to the ps laser peak intensity, or if there is a unique anomaly coefficient for ps irradiation. If we take the ratio between the quadratic term in Equation 2.22a with Equation 3.6, we find a factor of $1/(\nu_r \tau_p)$ remains. Using the repetition rate ($\nu_r = 80\,\text{MHz}$) and approximate pulse duration ($\tau_p = 2\,\text{ps}$) for the ps laser, we calculate $1/(\nu_r \tau_p) = 6250$. This factor is in agreement with our observation that cw and ps results differed by $\sim 10^3 - 10^4$; therefore, we have confirmed that the difference in the fitted quadratic curvatures between the cw and ps AS rates is due to the large peak intensities for the ps laser.

AS-to-S ratios observed when illuminating the nantenna with the ps laser are also shown, Figure 3.8. We see ratios that are much greater compared to the cw curves. The ratios being much larger is a surprise due to the enhanced Stokes scattering observed. For the ps results, the AS rates are so large that they overcome the enhanced Stokes rates, with respect to the cw results. In other words, the AS rates are boosted to a greater degree than the Stokes rates. The enhanced ratios show how using the ps laser source yields single-beam SECARS rates that are much greater than for the cw case. The ps results help validate our claim that the observed AS curvature is due to single-beam SECARS. For the cw measurements, the enhanced local fields are enough to produce single-beam SECARS. Then, when we use ps lasers, the large peak intensities boost the single-beam SECARS further. To quantify the enhancement in the AS-to-S for the ps results, we fit both the ps and cw results to a line and report the linear coefficients. For the cw results, the vibration dependent coefficient ranges from $\sim 0.2 - 1 \cdot 10^{-4}$, and for the ps the range is $\sim 170 - 330 \cdot 10^{-4}$. We see coefficients that are $\mathcal{O}10^3$ greater when using the ps source.

We have analyzed AS and AS-to-S curves for five separate nantennas. As mentioned before, the linear coefficient for the AS curves has a large uncertainty. The uncertainty for the fitted parameter is larger than the reported value; therefore, we cannot claim a physical value for the linear coefficient. When analyzing the AS-to-S ratios, we retrieve y-intercept values with smaller uncertainties, but when analyzing several particles, we cannot claim the y-intercept is physically significant. For some vibrations, for some of the nantennas, we retrieve fitted values for the y-intercept that are physically reasonable. For instance, values for the y-intercept tell us the degree of linear AS scattering we see when using the ps laser. We can also state what the asymmetry factor and anomaly coefficient are, much like we did for the cw case. Although there are times when we retrieve physically sensible y-intercept values, we more often get values that are not physical. For example, we retrieve negative values even though we expect positive values for a physically significant process. If we do happen to retrieve a positive value, the uncertainty in the fit is too large and we cannot claim the value is positive. Overall, statistics show that we cannot claim a value for the y-intercept, similar to being unable to claim a value for the linear coefficient for the AS curves. This is reasonable because the linear coefficient and y-intercept for the AS rates and AS-to-S ratios give insight into the same physical phenomena. Refer to the values for cw excitation for clarity.

The lack of physically significant values for the AS curve linear coefficient and AS-to-S ratio y-intercept tells us that a relatively insignificant amount of AS SERS is being produced by the ps laser, at the small average intensities used in this measurements. Therefore, the majority of the AS scattered light that is being detected is due to the single-beam SECARS. This is plausible because the average powers used for the ps SERS measurements are very small when compared to the cw results. Telling us that the large amount of signal we see is dependent on the peak intensity, and CARS is a signal which depends on the peak intensities.

Intensity dependent AS-to-S ratio for the 633.5 nm ps laser

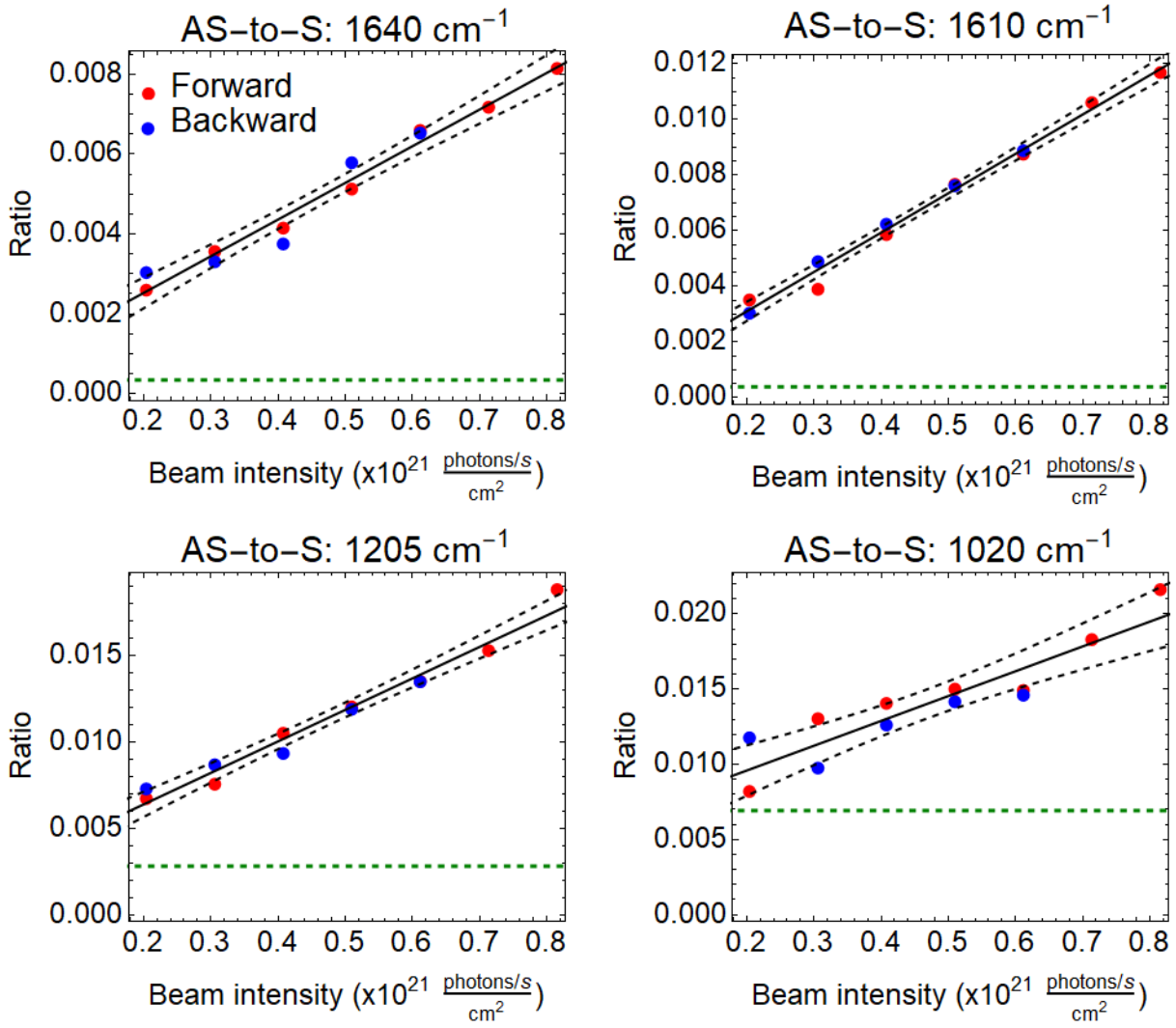

Figure 3.8: ps AS-to-S ratio sweeps using the 633.5 nm laser. The data points are fit to a linear function (solid line) and the confidence intervals are given (black, dashed lines). The horizontal green, dashed lines represent the ratio expected for a system composed of a purely thermally occupied excited state.

3.4 Plasmonic substrates for individual nantenna SE-CARS

After analyzing the single-beam SERS results, the Stokes beam was introduced. With spatially and temporally coincident pump and Stokes beams, the vibrational excitation profile can be obtained by recording AS signal as a function of frequency difference between the two beams. We keep the Stokes wavelength fixed at 1031 nm, and scan the pump wavelength near 883.5 nm, to obtain the vibrational line profile, Figure 3.9. The vibrational resonance in the SECARS excitation profile is notable by its flat baseline and high contrast, since on a nantenna the signal is always accompanied by the electronic CARS continuum of the metal. When introducing the pump and Stokes beams simultaneously, the resulting AS signal should be enhanced at the difference frequency to provide CARS. Figure 3.9 shows the enhanced AS signal resulting from the CARS process, using 883.5 nm as the pump source.

The photo-stability of the nanojunctions is limited. The signal degrades with irradiation time, with decay rates that are intensity dependent. To collect reliable CARS results, we aimed to find the average powers needed to obtain a stable CARS signal. Figure 3.10 shows the CARS signal over time when illuminated with different laser powers. The average powers given in the legend of Figure 3.10 are the same for pump and Stokes beams. The observed degradation of the signal over timescales of minutes, is suggestive of structural evolution in the nanojunction, such as the disappearance of hotspot due to fusion of the nanojunction.

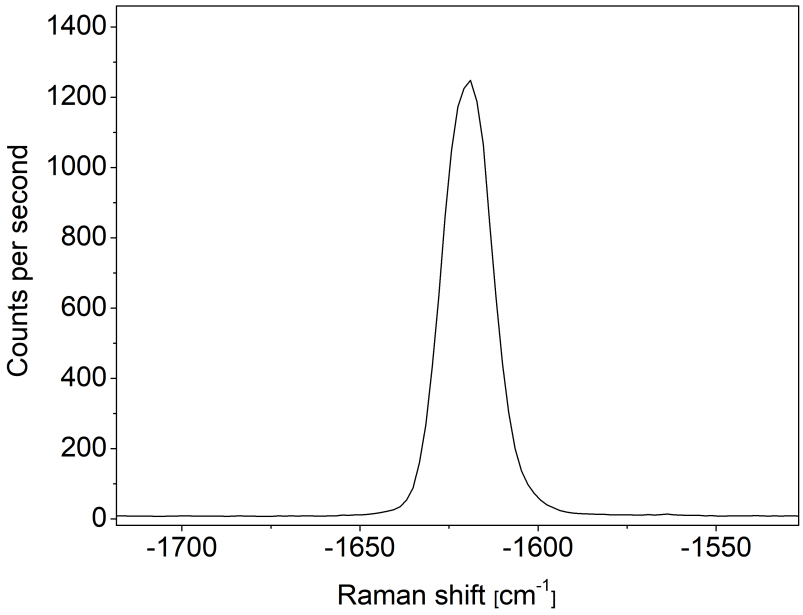

Figure 3.9: SECARS signal measured using a spectrometer and CCD when illuminating a BPE functionalized gold nantenna using 2 ps, 883.5 nm pump and 1030 nm Stokes beams. Average powers of 23 μW are used for each beam, which are focused on the sample plane using an oil-immersion objective lens (NA = 1.25). It is important to note this figure is desinged to show the SECARS signal as observed in the spectrometer software. The reported average powers, and observed SECARS signal, are too large to retain a stable SECARS signal (i.e. a signal that does not decay over time). The CARS resonance appears at an absolute Raman shift value of 1619 cm^{-1}.

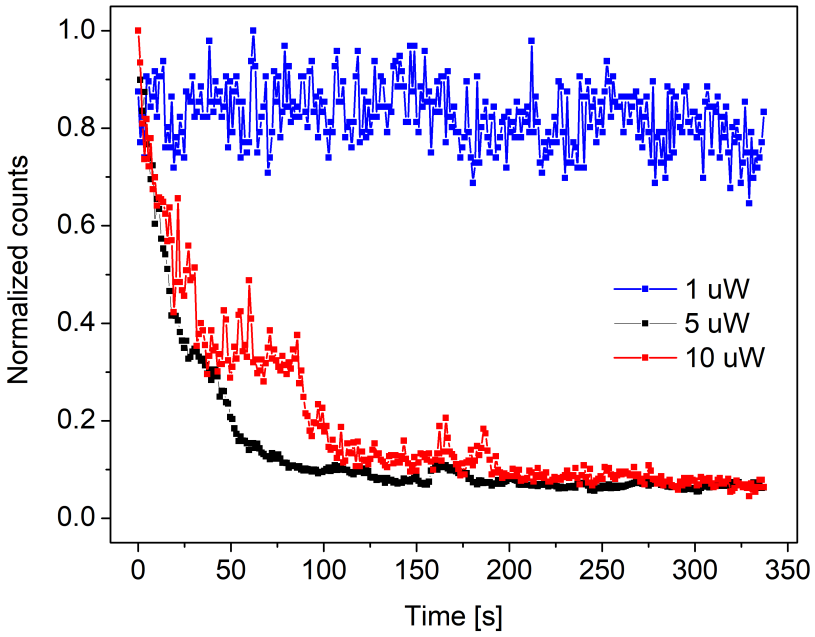

Figure 3.10: Trajectories showing time-dependent count rates for the SECARS signal as a function of incident laser power. The average powers are equivalent for the pump and Stokes beams and are given in the legend. The CARS signal is confirmed to be stable for average powers of 2 μW for both the beams.

3.5 Vibrational SECARS spectra show non-dispersive profiles

Figure 3.11 shows BPE SECARS for three separate nantennas on a pump wavelength (top row) or Raman shift (bottom row) axis. The back-scattered SECARS signal is measured by dispersing the AS scattered photons using a diffraction grating and recording the spectrum using a CCD camera. This allows us to integrate the SECARS signal over the vibrational resonance, effectively filtering out the non-resonant SECARS photons. The count rates given in Figure 3.11 are the rates specified by the A/D converter of the CCD.

From the SECARS results, we can make comparisons with liquid phase CARS. First, analogous to CARS, we see a non-resonant background contribution to $\chi^{(3)}$ when we tune the pump beam off resonance. This nonresonant SECARS signal arises principally from the metal

electrons of the nantenna. Second, in contrast to CARS, a dispersive contribution to $\chi^{(3)}$ does not manifest itself in the SECARS. The CARS signal is given as the square of the third order polarization, where the cross term (interference) between resonant and non-resonant contribtions, $\left[P_R^{(3)} + P_{NR}^{(3)}\right]^2$, leads to the dispersive line-shape when the components are out of phase [75]. The absence of such a profile implies that the molecular and electronic contributions are in phase and simply add under the square. Figure 3.12 repeats the spectra previously shown but this time overlayed to show the small particle-to-particle variation, where vertical dashed lines are added to represent the pump wavelengths used for resonant (883.8 nm) and detuned (887.9 nm) time-series scans. We see the variation in the resonance maximum is small, allowing us to use the same on and off resonance pump wavelengths for differing nantennas. This knowledge lets us perform time-series sweeps for several nantennas without having to measure each of their unique SECARS spectral signature.

According to our results, the SECARS and SERS spectral profiles are very similar. To aid in determining the mechanism for Gaussian broadening in the SECARS spectra, we compare to the Gaussian broadening seen in SERS. To check the molecular lifetime limited BPE linewidths, nantennas are illuminated with a cw HeNe laser at 632.8 nm. In practice, a cw laser linewidth is infinitely sharp with respect to the molecular linewidth. Therefore, the SERS spectrum will yield lifetime-limited molecular linewidths, as long as the spectrometer slit is sufficiently narrow. The Raman scattered light is focused into a spectrometer using a 1200 g/mm grating and 30 μm input slit width. The spectrometer resolution in the C=C region is approximately 2 cm^{-1}, as determined using a NeAr lamp source. The high resolution Stokes spectrum for a BPE-functionalized nantenna is displayed in Figure 3.13. The spectrum is representative for every nantenna tested, telling us there is no significant variation in resonance position from nantenna-to-nantenna SERS scattering. The measured FWHM for each of the five most prominent vibrations is given in Table 3.3. We see from the SERS Stokes scattering that the linewidths are Gaussian broadened with respect to spontaneous Raman. This says the resonance dissipates faster when it finds itself is a plasmonic bath.

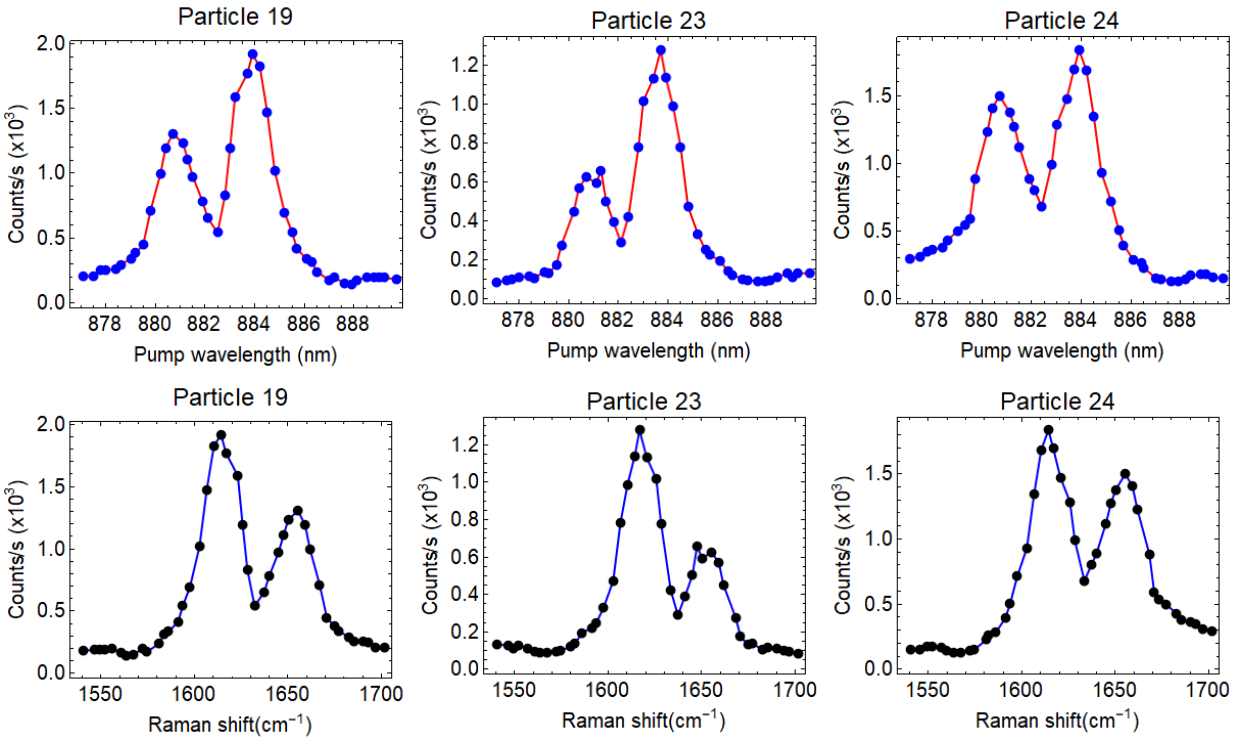

Figure 3.11: BPE SECARS spectra for multiple nantennas plotted either on a pump wavelength (top row) or Raman shift (bottom row) axis. The average input intensities are approximately 2.5 and 2.0 μW/μm^2 for the pump and Stokes beams, respectively. The average laser powers used for intensity calculations are measured before the objective lens. By sweeping the pump laser in approximately 0.3 nm increments, we measure the CARS spectrum for the C=C stretching modes near 1600 cm^{-1}.

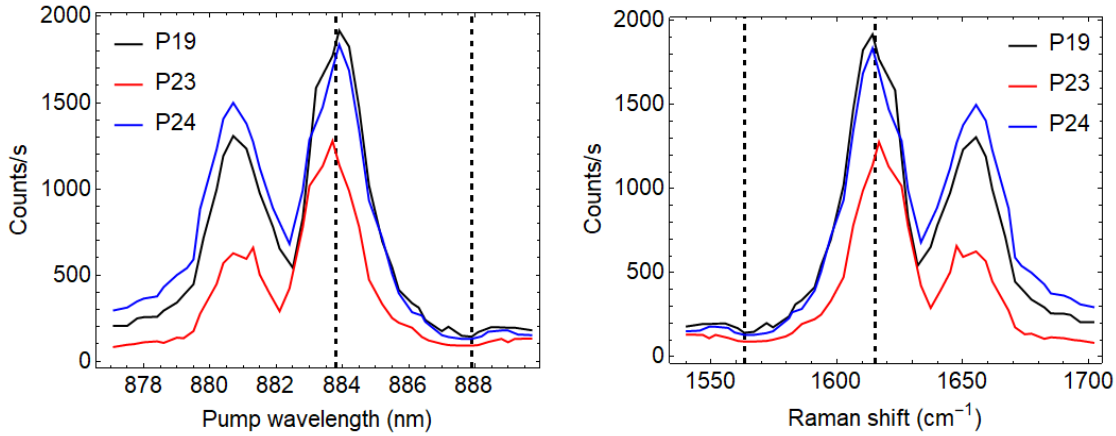

Figure 3.12: Overlayed SECARS spectra for multiple nantennas plotted either on a pump wavelength (left) or Raman shift (right) axis. The spectra are the same as those shown in Figure 3.11 but are overlayed here to highlight the variation between individual nantennas. The vertical dashed lines signify the pump wavelengths used for time-series measurements. Pump wavelengths of 883.8 and 887.9 nm are used for on and off resonances time-series sweeps, respectively.

In other words, the vibrational lifetime is made smaller when the molecule is sandwiched in a plasmonic nanocavity. From the FWHM information, we can estimate the vibrational lifetime for each of the five resonances.

It has previously been reported that BPE SERS linewidths appear Gaussian [29] due to inhomogeneous broadening. In my high-resolution SERS spectra, I also see line-shapes that are significantly Gaussian broadened, resulting in line-shapes that show more Gaussian than Lorentzian character. The Lorentzian character is still present as evidenced by the resonance tails which tend to the baseline more slowly than for a Gaussian. Again, the results suggest the linewidths are better modeled by the Voigt profile. In Figure 3.14, we show the C=C region of the SERS spectrum and fit the resonances to both a Voigt (3.14a) and Gaussian (3.14b) distribution. We can see both distributions adequately fit the data points around the maxima but the Voigt profile outperforms in the tails. To see how the resonance behavior varies from nantenna-to-nantenna, we measure high resolution Stokes scattering for six separate nantennas. The results shown in Table 3.2 indicate there is nantenna-to-nantenna

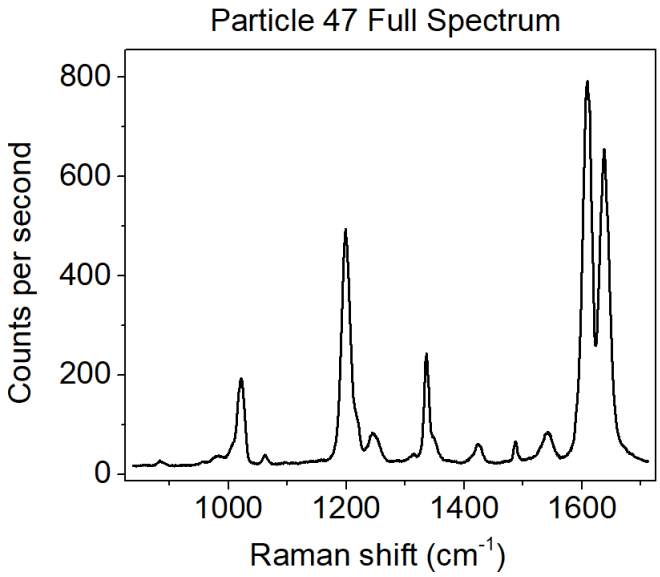

Figure 3.13: High resolution SERS spectrum for BPE collected using a 1200 g/mm grating and 30 μm slit width. We use the vibrational limited linewidths to estimate the excited state lifetimes for each resonance. The spectrum is representative of measured nantennas; meaning, we see consistent spectra from nantenna-to-nantenna.

variation in the fitted parameters. Interestingly, the contribution to the line-shape from Gaussian broadening consistently results in profiles that clearly have more Gaussian than Lorentzian character.

For a CARS process, the resonant contribution to the line-shape follows a Lorentzian distribution if homogeneously broadened. It is important to note that to obtain the true line-shape, the spectral widths of the pump and Stokes lasers should be much sharper than the molecular linewidth. This is realized in CARS measurements using nanosecond and longer pulse durations. When using picosecond (ps) pulses, like in these measurements, one needs to consider how the laser bandwidth is going to broaden the molecular resonance. When using a Gaussian ps pulse, with spectral width comparable to a homogeneously broadened molecular line, the SECARS linewidth will no longer be purely Lorentzian. It will become a convolution of a Lorentzian and Gaussian, namely, a Voigt profile. Using the time-bandwidth product for a Gaussian laser pulse, we find linewidths of 8.4 cm^{-1} and 6.2 cm^{-1} for the 882 nm pump

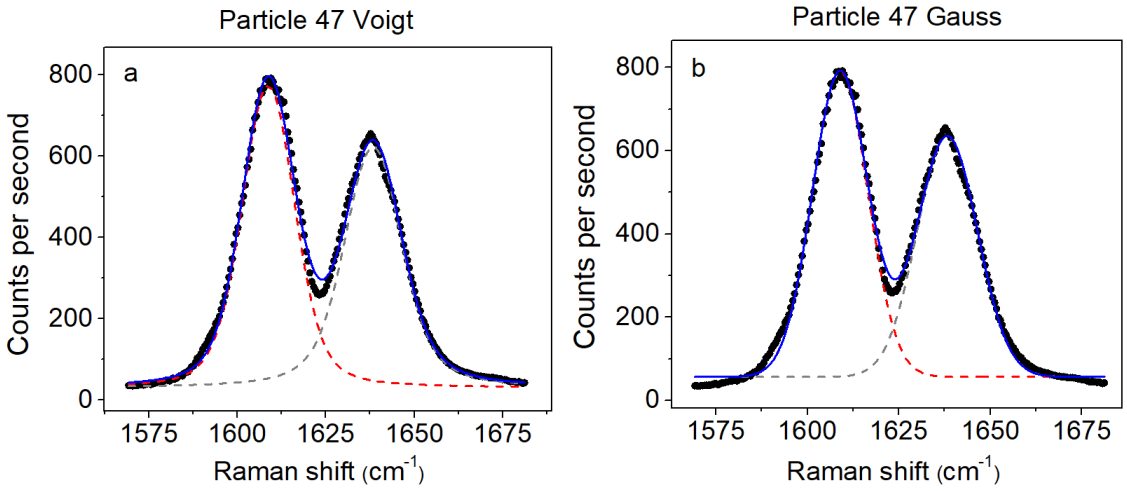

Figure 3.14: Magnified SERS spectrum displaying the C=C region with fits using either a Voigt (a) or Gaussian (b) distribution. The black points represent the measured results and the curves represent the fits. The blue curves is the best fit using a sum of Voigt or Gaussian profiles. The red and gray dashed curves represent the individual linewidth fits.

Table 3.2: Measured FWHM ($\Delta\tau$) values from the BPE SERS using a Voigt distribution. The Gaussian (σ) and Lorentzian (γ) contributions to the line-shape are also given for each resonance.

Particle	σ_1 (cm^{-1})	γ_1 (cm^{-1})	$\Delta\tau_1$ (cm^{-1})	σ_2 (cm^{-1})	γ_2 (cm^{-1})	$\Delta\tau_2$ (cm^{-1})
44	13.3	6.53	17.1	15.7	4.60	18.3
45	18.2	3.82	20.4	16.5	5.88	19.9
46	15.4	3.93	17.6	16.8	5.66	20.0
47	14.7	5.26	17.7	14.7	7.88	19.4
48	17.3	4.68	19.9	17.7	4.95	20.5
49	18.1	2.97	19.7	21.5	0.22	21.6

Table 3.3: Approximate FWHM values for the Raman lines shown in Figure 3.13. The values are determined from the wavenumber difference between 50% intensity points.

Resonance (cm^{-1})	FWHM (cm^{-1})	Lifetime (ps)
1022	15.3 ± 1.0	0.96 ± 0.06
1200	18.2 ± 1.0	0.81 ± 0.04
1336	10.9 ± 1.0	1.4 ± 0.12
1610	19.8 ± 1.0	0.74 ± 0.04
1638	21.9 ± 1.0	0.67 ± 0.03

($\Delta\tau_{\text{pulse}} = 1.75$ ps) and 1030 nm Stokes pulses ($\Delta\tau_{\text{pulse}} = 2.38$ ps), respectively. The third-order measurement involves a triple convolution of the pulses, and the resulting instrumental resolution can be directly obtained experimentally by considering the non-resonant electronic SECARS response.

Now that we have justified the anticipated line-shape, the SECARS spectrum is fit to a Voigt profile, Figure 3.15. The resulting Lorentzian and Gaussian contributions to the Voigt fit are given in Table 3.4. The two resonances are centered around 1615 cm^{-1} (resonance 1) and 1655 cm^{-1} (resonance 2). For both resonances, we have consistent fitted parameters yielding linewidths that are predominantly Gaussian. There are two exceptions to this general observation. For Particles 24 and 26, we see one resonance for each nantenna violates the general observation. For Particle 24, resonance 2 is the offender, but its discrepancy is rationalized by signal degradation. The resonance tail at higher Raman shifts does not tend to the baseline as quickly as expected. Considering pump wavelength sweeps begin at smaller wavelength values, it is likely that the initial signal seen at ∼1690 cm^{-1} which begins to degrade as we sweep to ∼1560 cm^{-1}. It is likely that if we could measure the SECARS at ∼1690 cm^{-1} after the completion of the sweep, that the measured signal would now be smaller in magnitude. The smaller magnitude would result in a faster decay of the high energy tail, and the resonance would take on more Gaussian character. For Particle 26, resonance 1 deviates from our expectation. It is not clear why this nantenna strays from the general trend, and measurements on several more nantennas would be needed to say whether

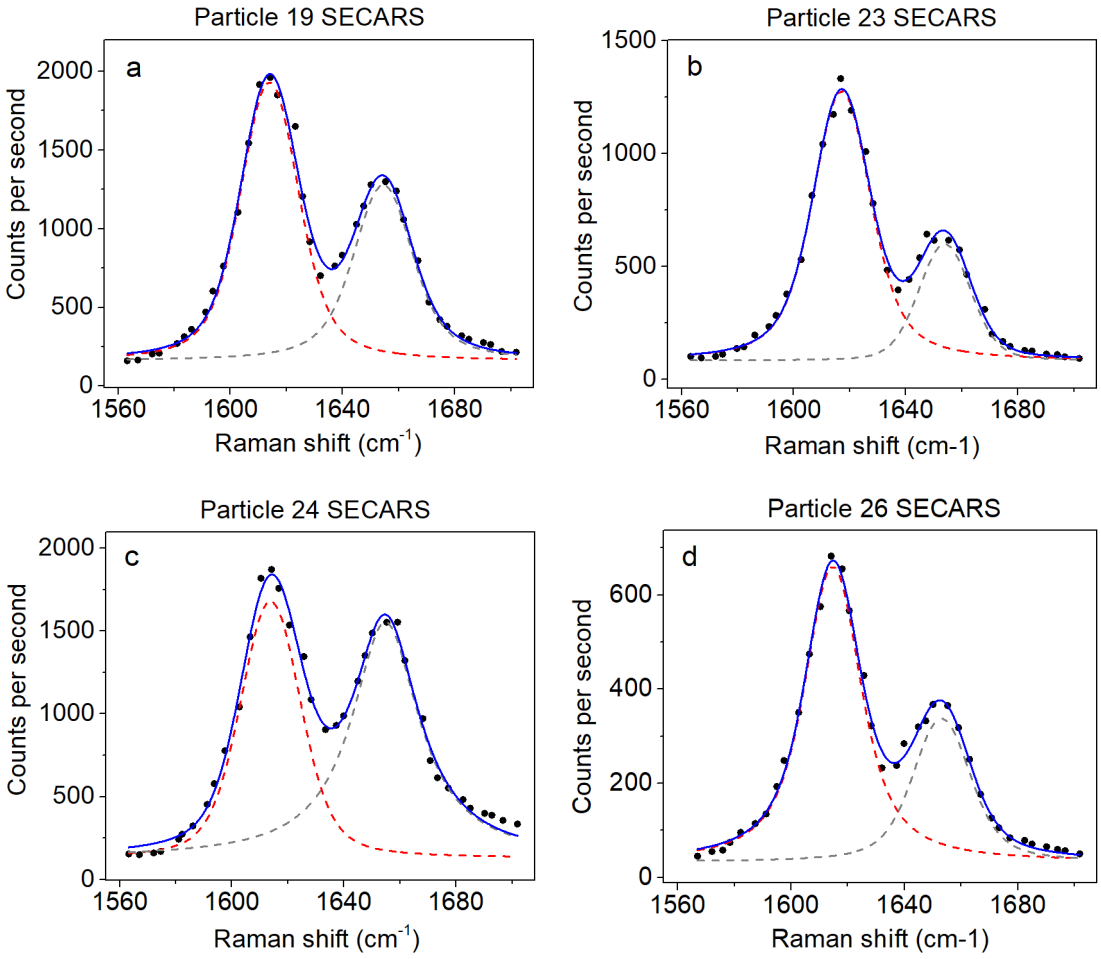

Figure 3.15: Experimental BPE SECARS spectra fit using a Voigt profile. The black points represent the measured results and the curves represent the fits. The blue curves are the best fit using a sum of Voigt profiles. The red and gray dashed curves represent the individual linewidth fits. The resonances are referred to as 1 and 2 and are centered at 1615 and 1655 cm^{-1}, respectively.

this observation is statistically significant. Discovering resonances that are predominantly Gaussian is contradictory to our initial assumption that the Gaussian portion should be about 8.4 cm^{-1}. This says that there are additional contributions to the SECARS which makes it appear Gaussian.

We show SECARS of BPE at a nanojunction using ps pulses. From the data, we see a dramatic enhancement of the AS signal, over spontaneous AS radiation, when introducing a stimulating Stokes pulse. This highlights the coherent enhancement and additional plasmonic

Table 3.4: Measured FWHM ($\Delta\tau$) values from the BPE SECARS using a Voigt distribution. The Gaussian (σ) and Lorentzian (γ) contributions to the line-shape are also given for each resonance.

Particle	σ_1 (cm^{-1})	γ_1 (cm^{-1})	$\Delta\tau_1$ (cm^{-1})	σ_2 (cm^{-1})	γ_2 (cm^{-1})	$\Delta\tau_2$ (cm^{-1})
19	18.6 ± 3.5	10.3 ± 4.9	24.7 ± 0.8	16.9 ± 6.5	13.4 ± 7.9	25.2 ± 1.7
23	17.4 ± 2.8	11.9 ± 3.7	24.6 ± 0.7	19.3 ± 5.5	4.7 ± 8.3	21.9 ± 1.5
24	20.5 ± 3.7	8.6 ± 5.4	25.5 ± 0.9	0.0 ± 0.0	29.2 ± 14.3	29.2 ± 9.4
26	12.8 ± 3.0	16.6 ± 3.1	23.8 ± 0.7	17.5 ± 5.5	11.2 ± 7.3	24.2 ± 1.5

enhancement offered by SECARS. We have showed at average powers as low as 5 μW, signal degradation occurs when continuously illuminating the nanojunction with both pump and Stokes pulses. CCD count rates of >2500 Hz are seen at these power levels which offer promise to data acquisition rates greater than previously reported. Our experiments show stable SECARS count rates for beam powers of 2 μW for both the pump and Stokes lasers. The stable SECARS count rates allow us to tune the pump beam wavelength to capture a SECARS spectrum for BPE at the nanojunction.

3.6 Estimate of the SECARS enhancement factor

SERS enhancement factors (EFs) are determined by comparing plasmonically enhanced Raman scattering to Raman scattering in the absence of a plasmonic substrate, normalized to the number of molecules contributing to each observed signal. We can determine the CARS cross section (γ) for the spontaneous Styrene CARS and BPE SECARS measurements. The ratio between the spontaneous CARS and SECARS cross sections yields the plasmonic enhancement factor. A more thorough comparison can be made when comparing BPE spontaneous CARS to BPE SECARS, but using Styrene CARS as a substitute will yield an acceptable result (i.e. SECARS enhancement factors within an order of magnitude).

Figure 3.16 gives Styrene CARS (left) and BPE SECARS (right). The experimental arrangement and detection scheme is the exact same for both spectra, with the only difference being the sample. Both measurements are made in a transmission geometry and either CARS or SECARS scattered light is detected in the forward direction using a PMT in photon counting mode. CARS scattering rates can be modeled using an effective cross section, γ [76],

$$R_{CARS}\left[\frac{\text{photons}}{\text{s}}\right] = N_0^2 * \gamma\left[\text{cm}^6 s^2\right] * I_s\left[\frac{\text{photons}}{\text{cm}^2\,\text{s}}\right] * I_p^2\left[\frac{\text{photons}^2}{\text{cm}^4\,\text{s}^2}\right] \tag{3.9}$$

where N_0 is the number of molecules contributing to a spontaneous CARS signal. CARS scattering rates are quadratic in the third order polarization; therefore in the number of molecules, N_0 [77], that coherently contribute to the signal. The pump and Stokes input intensities are I_p and I_s, respectively. The CARS cross section, γ, is a proportionality constant used to equate the left-hand side to the right-hand side, and also ensures the units on both sides agree.

For the enhancement factor calculations, it is necessary to convert intensity units using the relation below,

$$I_N\left[\frac{\text{photons}\,\text{s}^{-1}}{\text{cm}^2}\right] = I_L\left[\frac{\text{W}}{\text{cm}^2}\right] * \frac{\lambda}{hc} \tag{3.10}$$

where λ is the laser wavelength, h is Planck's constant, and c is the speed of light. To calculate the input intensity, the input power and the focused laser spot diameter, w_0, are used. The spot size diameter is calculated using the expression [78],

$$w_0 = 1.22 * \frac{\lambda}{NA} \tag{3.11}$$

where NA = 0.65 and NA = 1.25 are the numerical apertures for the oil-immersion lens used to illuminate the sample for CARS and SECARS, respectively. Pump and Stokes wavelengths of 884 and 1030 nm are used for both sets of measurements.

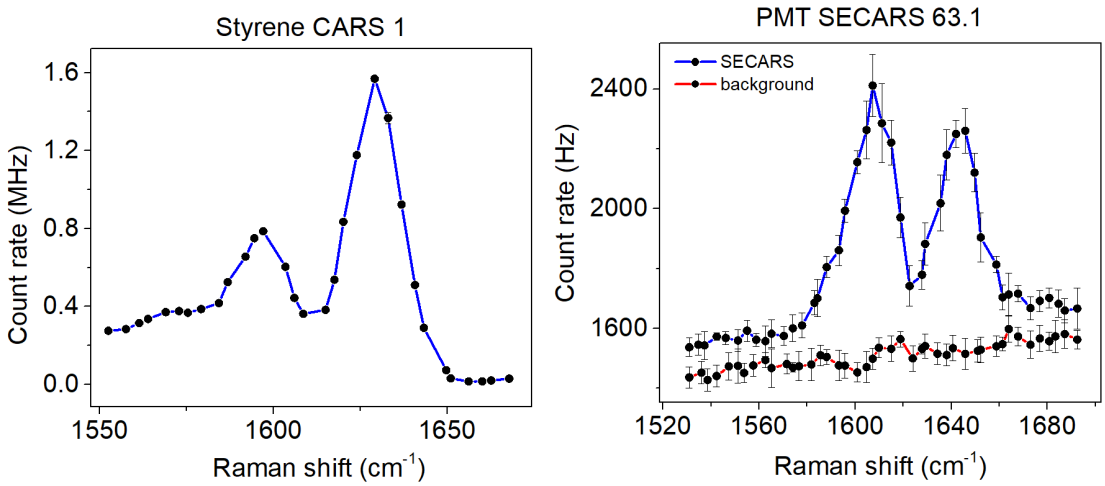

Figure 3.16: Measured spontaneous Styrene CARS (left) and BPE SECARS (right) detected in the forward direction detected using a PMT in photon counting mode. The background (red curve) for the SECARS plot is the signal obtained when the frequency sweep is performed with the Stokes beam blocked.

It is also necessary to determine the number of Styrene molecules illuminated for the CARS results. To calculate the number of molecules, we use the density (909 kg/m^3) and molecular mass (104.15 g/mol) of Styrene, and the illuminated focal volume. The focal volume is determined assuming a cylinder given by Gaussian optics. In linear excitation, $2w_0$ is used as the diameter of the cylinder, and two times the Rayleigh length, z_R (also known as the confocal parameter), as the cylinder's height, where the Rayleigh length is given as,

$$z_R = \frac{\pi w_0^2}{\lambda} \tag{3.12}$$

therefore, the volume of the cylinder is,

$$\begin{aligned} V &= 2\pi w_0^2 z_R \\ &= \frac{4.43\pi^2}{NA^4}\lambda^3 \end{aligned} \tag{3.13}$$

Table 3.5: Spontaneous CARS parameters needed to calculate spontaneous CARS cross section (γ) in Equation 3.9.

R_{CARS} [photons s^{-1}]	N_0[molecules]	I_s [photons s^{-1} cm^{-2}]	I_p [photons s^{-1} cm^{-2}]
$1.6 \cdot 10^6$	$8.9 \cdot 10^{11}$	$1.9 \cdot 10^{24}$	$1.2 \cdot 10^{24}$

For NA = 0.65 and λ = 884 nm, the excitation volume (V) is calculated to be, V = $1.69 \cdot 10^{-16}$ m^3. For a third order process, the effective beam waist is reduced,

$$I^3 = \left(I_0 \, \mathrm{Exp}\left[\frac{-2r^2}{w_0^2} \right] \right)^3 = I_0^3 \, \mathrm{Exp}\left[\frac{-6r^2}{w_0^2} \right] \tag{3.14}$$

Therefore, $w_0^{(3)} = \sqrt{3}\, w_0^{(1)}$. Also, the associated Rayleigh length is shortened, which is defined as the distance over which the beam waist expands by a factor of two. The Gaussian profile applies along the propagation direction at the focus, therefore another factor of $\sqrt{3}$ reduction appears along the length of the cylinder. Overall, the volume is reduced by a factor of three relative to a linear process.

$$V^{(3)} = \frac{1}{3} V^{(1)} \tag{3.15}$$

From the experimentally observed CARS count rate, known pump and Stokes incident powers of 5.9 and 11.0 mW, respectively, and a NA = 0.65 objective lens, the intensities and the number of molecules in the focal volume can be obtained (see Table 3.5) and used to extract a CARS cross section of $\gamma = 7.4 \cdot 10^{-91} \mathrm{cm}^6\mathrm{s}^2$ for Styrene in the liquid phase.

Enhancement factors (EFs) are necessary for plasmonically-enhanced Raman processes because one must rationalize the observed count rates considering the number of molecules being excited are several orders of magnitude smaller than the spontaneous case. As seen in Table 3.5, the number of molecules being illuminated for spontaneous CARS is about $10^{11} - 10^{12}$. In plasmonically-enhanced Raman, about a handful of molecules contribute the significant majority of Raman scattered light [49, 65, 79]. Therefore, for SECARS, γ in Equation 3.9 now becomes the SECARS cross section, γ^*.

Table 3.6: BPE SECARS parameters needed to calculate the SECARS cross section γ^* in Equation 3.9.

R_{SECARS} [photons s^{-1}]	I_s [photons s^{-1} cm^{-2}]	I_p [photons s^{-1} cm^{-2}]
10^3	$6.5 \cdot 10^{20}$	$7.6 \cdot 10^{20}$

For the SECARS results, an objective lens (NA = 1.25) is used, and the input pump and Stokes laser powers are each set to 1 μW. The SECARS cross section γ^* is then calculated using Equation 3.9 and the values reported in Table 3.6. The result is: $N_0^2\,\gamma^* = 2.7 \cdot 10^{-60}$, where the number of molecules is left in the result to keep it flexible. For example, $\gamma^* = 2.7 \cdot 10^{-60}$ for $N_0 = 1$, or $\gamma^* = 2.7 \cdot 10^{-64}$ for $N_0 = 100$. The enhancement factor (EF) can be defined as the ratio between the SECARS (γ^*) and CARS (γ) cross sections,

$$\text{EF} = \frac{\gamma^*}{\gamma} \tag{3.16}$$

Therefore, EF $= 3.6 \cdot 10^{30}$ for $N_0 = 1$ or EF $= 3.6 \cdot 10^{26}$ for $N_0 = 100$. The enhancement factor reported here is significantly greater than previously reported values [72]. EF is expressed using,

$$\text{EF} = \frac{W_{\text{CARS}}}{\left(N_0^2 \alpha^4 I_s I_p^2\right)_{\text{Styrene}}} \frac{\left(N_0^2 \alpha^4 I_s I_p^2\right)_{\text{BPE}}}{W_{\text{SECARS}}} \tag{3.17}$$

where α is the polarizability, and W are the observed count rates under the same collection geometry, therefore collection efficiency.

From our cw measurements, we found SERS EFs of $\sim 10^{11}$. In terms of β, the observed results give $\beta^4 = 10^{11}$; therefore, we anticipate SECARS to yield $\beta^8 = 10^{22}$. Instead, we observe results more readily described by $\beta^8 = 10^{30}$. We say 10^{30}, because we are confident the bulk of the SECARS is coming from a number of molecules that are on the order of unity. The large SERS EFs that we observe are representative of pico-cavity formation; therefore, most scattering is localized to a single molecule. This is because our nantennas are composed of nanocavities which yield results representative of pico-cavity scattering. We

are observing SECARS EFs which are 10^8 greater in magnitude than initially anticipated. SECARS is the result of four interactions; therefore, we can say that 10^2 enhancement comes from each of the interactions. When comparing to our cw AS results, we see the 10^2 agrees with our enhancement due to the anomaly. The anomaly coefficient, η_v, manifests itself in the SECARS results, much like it did for the cw measurements.

3.7 Simultaneously detected SECARS and anti-Stokes SERS

We have adequately proved the AS signal we see is indeed SECARS, but it is informative to show the signal dependence on input laser powers (i.e. intensities). Figure 3.17 shows the SECARS dependence on the pump (left) and Stokes (right) laser powers. Each data point in the graphs comes from integrating the SECARS signal at each power combination and the solid curves are best fits to either a quadratic (pump) or linear (Stokes) polynomials. As expected, the SECARS signal is second order in the input pump intensity and is proportional to the input Stokes intensity. A benefit to collecting the SECARS dependence on pump and Stokes intensity, is it gives an experimental measurement of the SECARS cross section, γ, according to Equation 3.9, when corrected for collection efficiency.

Two realizations of AS Raman scattering are recognized when using plasmonic nantennas. The Jablonski energy level diagrams for each process are given in Figure 3.18. For surface-enhanced anti-Stokes Raman (AS SERS), an AS photon is spontaneously emitted from the populated excited vibrational state to the ground vibrational state. This measurement probes the population from the excited state and can tell us the phenomena responsible for populating the state. Surface-enhanced coherent anti-Stokes Raman (SECARS) probes the time-dependent coherence between the ground and excited vibrational states, as observed

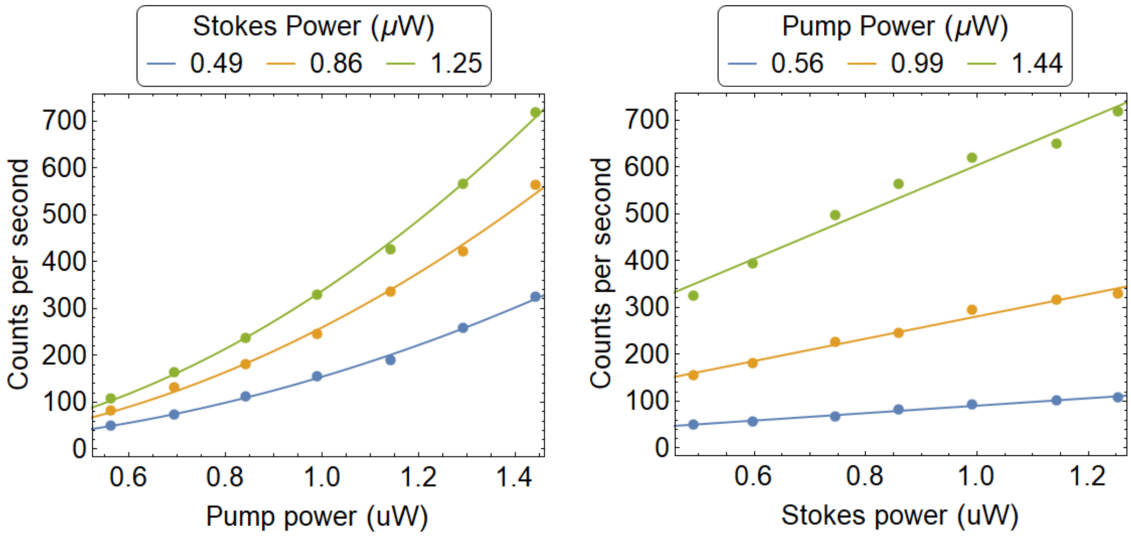

Figure 3.17: Power dependence curves for on resonant SECARS. The data points come from integrating the SECARS signal for each power combination and the solid curves are best fits using a quadratic (left) or linear (right) polynomial. As expected, the SECARS signal is quadratic versus the pump power and linear versus Stokes power.

by a spontaneously emitted AS photon. Coherent anti-Stokes Raman (CARS) requires a pump photon (ω_p), a stimulating Stokes photon (ω_{st}), and a probe photon (ω_{pr}). For our measurements, a second pump photon from the laser pulse is used as the probe photon. Generally, the spontaneously emitted photon is AS with respect to the probe photon frequency.

To emphasize the simultaneous SECARS and AS SERS, we record an AS spectrum with greater signal-to-noise (S:N) to highlight multiple AS SERS resonances, Figure 3.19. Resonance linewidths are artificially broadened by the 2 ps laser. The pump laser is detuned from resonance and the resulting SECARS signal appears at ~1750 cm^{-1}. The four additional resonances seen constitute the spontaneous emitted, single beam AS SERS. To confirm that we are seeing simultaneous SECARS and SERS, we can track the AS peak positions as we tune the pump wavelength. For SERS, the AS frequency (ω_{as}) is given by,

$$\omega_{as} = \omega_p + \omega_v \tag{3.18}$$

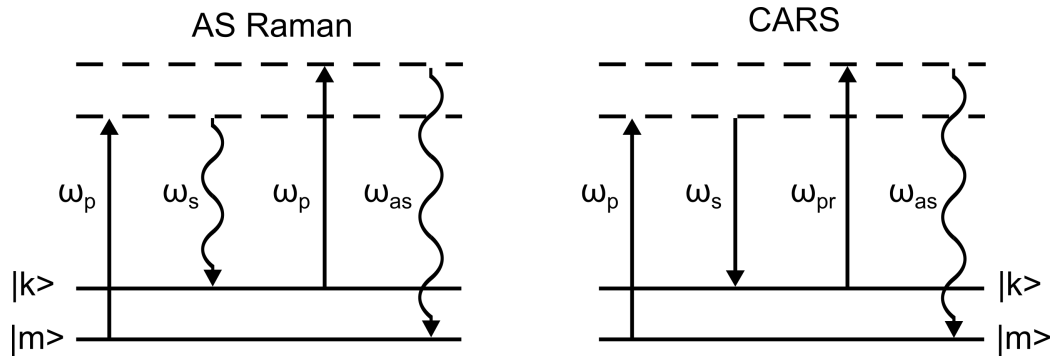

Figure 3.18: Jablonski energy diagrams for anti-Stokes (AS) Raman and coherent anti-Stokes Raman(CARS).

where ω_v and ω_p are the vibration and pump laser frequencies, respectively. The spontaneously emitted AS frequency (ω_{CARS}) is given by,

$$\omega_{CARS} = 2\omega_p - \omega_{st} \tag{3.19}$$

where ω_{st} is the Stokes frequency. From the above expression, we see the CARS photon frequency is independent of the vibrational frequency, and instead, depends on the Stokes frequency.

Now that we know the AS Raman and CARS anti-Stokes frequency dependencies, we can manipulate the relations to show how the AS wavelength depends on the pump wavelength. Using the relations $\lambda = 2\pi c\omega^{-1}$ and $\tilde{\nu}\lambda = 1$, where c is the speed of light and $\tilde{\nu}$ ($\tilde{\nu} = \nu/c$) is the Raman shift frequency, we find the AS Raman (λ_{AS}) and CARS (λ_{CARS}) AS wavelengths can be described by,

$$\begin{aligned} \lambda_{AS} &= \frac{\lambda_v}{\lambda_v + \lambda_p} \cdot \lambda_p \\ \lambda_{\text{CARS}} &= \frac{\lambda_{st}}{2\lambda_{st} - \lambda_p} \cdot \lambda_p \end{aligned} \tag{3.20}$$

where λ_v, λ_p, and λ_{st} are the vibrational, pump, and Stokes wavelengths, respectively. We choose to write the relations in this format to highlight the AS wavelengths for both processes

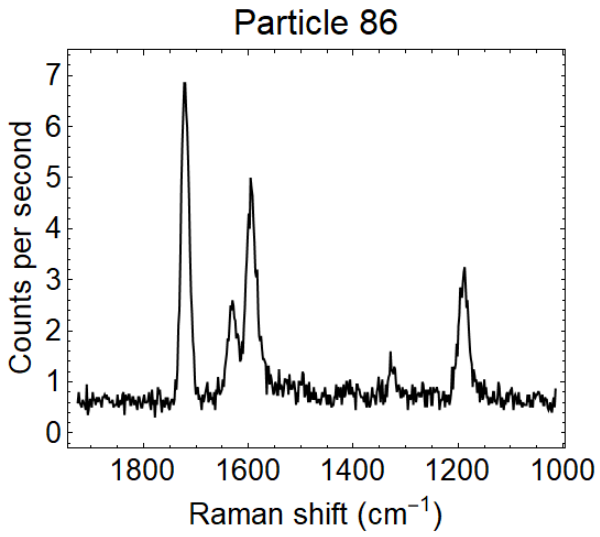

Figure 3.19: Plot showing simultaneous SECARS and AS SERS. The detuned SECARS appears at 1734 cm^{-1}. The improvement in S:N allows us to see multiple AS SERS resonances. Further confirming simultaneous SECARS and AS SERS detection.

are approximately linear in the pump wavelength, λ_p. This is because the first term on the right-hand side of both relations is approximately constant for the range of pump wavelengths used in the measurements. Therefore, the first term on the right-hand side acts as the slope when plotting the AS wavelength versus pump wavelength, Figure 3.20.

Figure 3.20 shows the AS Raman and CARS anti-Stokes wavelengths as a function of pump wavelength. The graph shows simulated results using the relations in Equation 3.20. As previously mentioned, the AS wavelengths for both processes are approximately linear in the pump wavelength. Interestingly, the CARS anti-Stokes wavelength spans a range of values which is greater than the AS Raman range of values. The two lines intersect at the AS wavelength where the CARS intensity is maximum. In other words, the intersection occurs when the difference between the pump and Stokes frequencies equal the vibration frequency, $\omega_v = \omega_p - \omega_{st}$. We note the simulation assumes a Stokes frequency corresponding to a wavelength of 1030 nm for CARS and a vibration frequency at 1620 cm^{-1} for the AS Raman.

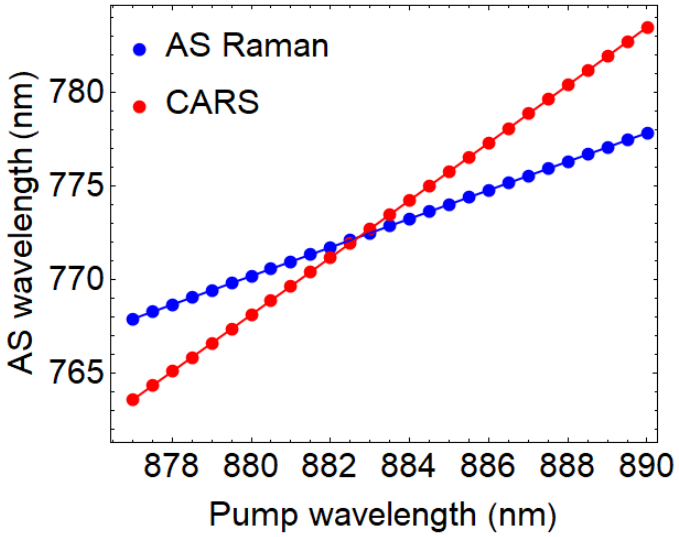

Figure 3.20: Plot showing the anti-Stokes wavelength for AS Raman and CARS as a function of the pump wavelength. The simulated curves assume a Stokes wavelength of 1030 nm for CARS and a vibration frequency at 1620 cm^{-1} for the AS Raman

Figure 3.21 shows experiment measurements for the simultaneously detected AS SERS and SECARS. The image plot shown in Figure 3.21a displays the SECARS and AS SERS anti-Stokes wavelengths as a function of pump wavelength, bounded by the white and black lines, respectively. As expected from the simulation, the SECARS anti-Stokes wavelengths span a greater range of values. The range of AS wavelengths for both SECARS and AS SERS match the simulation almost perfectly, confirming our statement that we are seeing simultaneous AS SERS and SECARS. Figure 3.21b shows stacked spectra from y-cuts in the image plot at the specified pump wavelength, λ_p. The middle panel in the stacked spectra shows λ_p for maximum CARS intensity. As previously mentioned, this pump wavelength is where the intersection between the SECARS and AS SERS anti-Stokes wavelengths occur. The image plot is on a Log10 scale to emphasize the AS SERS signal, while the stacked spectra is on a linear scale.

To aid in determining the mechanism for AS SERS, we collect simultaneous detuned SECARS and AS SERS intensity dependence curves. To visualize the detuned SECARS and AS SERS simultaneously, we tune the pump laser to 873.9 nm. This is necessary to ensure the SECARS

Table 3.7: Second-order coefficients from the quadratic fitting results. The coefficients from the detuned SECARS curves shows a clear increase due to SECARS proportionality to input Stokes power. The coefficients for the AS SERS do not show appreciable dependence on the Stokes laser power. Any differences are likely due to uncertainties in the measurement and a lack of significant dynamic range in the pump power values.

Stokes power (μW)	SECARS	1630 cm^{-1}	1596 cm^{-1}	1188 cm^{-1}
0.63	23.0 ± 1.1	19.5 ± 1.5	37.5 ± 1.7	21.3 ± 1.4
0.75	26.4 ± 0.9	20.3 ± 1.1	37.8 ± 1.4	22.3 ± 1.6
0.92	29.9 ± 2.0	21.0 ± 0.6	37.8 ± 1.8	23.5 ± 1.2

signal is spectrally resolved from the AS SERS; meaning, it does not mask the AS SERS C=C stretch at approximately 1620 cm^{-1}. The pump power dependent scattering rates are given in Figure 3.22. Interestingly, we see quadratic dependence on the pump power (i.e. the pump intensity) for both the detuned SECARS and AS SERS signal photons. For the detuned SECARS, Figure 3.22a shows an expected dependence on the input Stokes power. More importantly, the AS SERS curves show no meaningful dependence on the Stokes power, as most clearly evidenced by the 1596 cm^{-1} resonance, Figure 3.22c. This is fascinating because it tells us there is zero measurable laser heating in the nanojunction when increasing the Stokes power.

When comparing the detuned SECARS and AS SERS, we see the fitted quadratic coefficients for both cases are nearly identical, Table 3.7. To see how the resonant SECARS compares to the AS SERS, we use the ratio of resonant-to-detuned SECARS scattering. This ratio offers the scaling factor needed to accurately estimate the resonant SECARS intensity dependent behavior from the detuned measurements. To determine the necessary scaling factor, we collect a SECARS spectrum from the nantenna under investigation, Figure 3.21d. We find the scaling factors needed for the resonances at 1609 and 1645 are 14.4 and 13.4, respectively. After determining the scaling factors for resonant to detuned SECARS, the simultaneous resonant SECARS and AS SERS power sweeps are plotted, Figure 3.23.

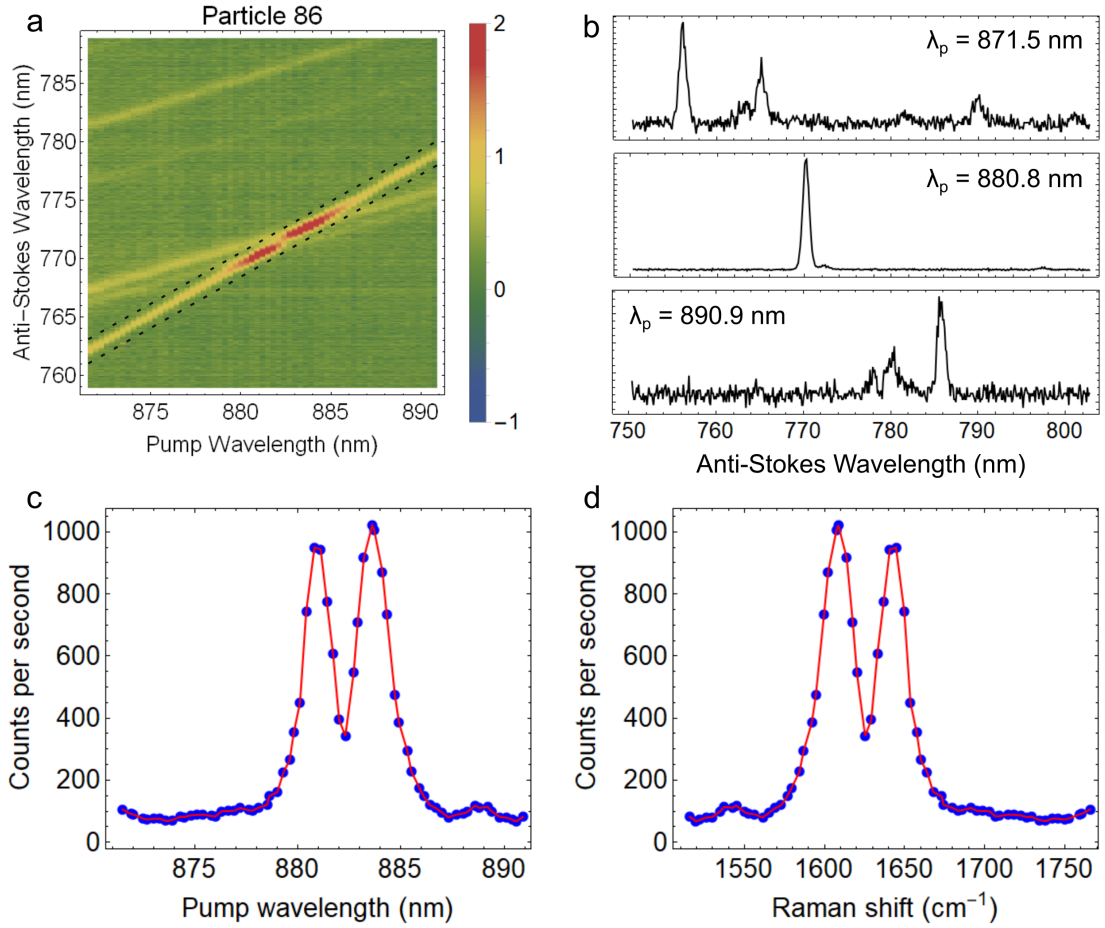

Figure 3.21: Graphs showing simultaneously measured SECARS and thermal anti-Stokes (AS). a) Image plot showing the SECARS and thermal AS. The SECARS signal is bounded by black dashed lines. b) Stacked plots showing the SECARS and thermal AS spectra from y-cuts in the image plot at specified pump wavelengths (λ_p). The image plot is on a Log10 scale to emphasize the AS SERS signal, while the stacked spectra is on a linear scale. c) BPE SECARS spectra plotted either on a pump wavelength (left) or Raman shift (right) axis. By sweeping the pump laser in approximately 0.3 nm increments, we measure the SECARS spectrum for the C=C stretching modes centered at 1609 and 1645 cm^{-1}. The SECARS count rates for the 1609 and 1645 cm^{-1} modes are 1021 and 950 counts per second (cps), respectively. The count rate at 1734 cm^{-1}, the Raman shift frequency corresponding to the pump wavelength for our simultaneous SECARS and AS SERS measurement, is 71 cps.

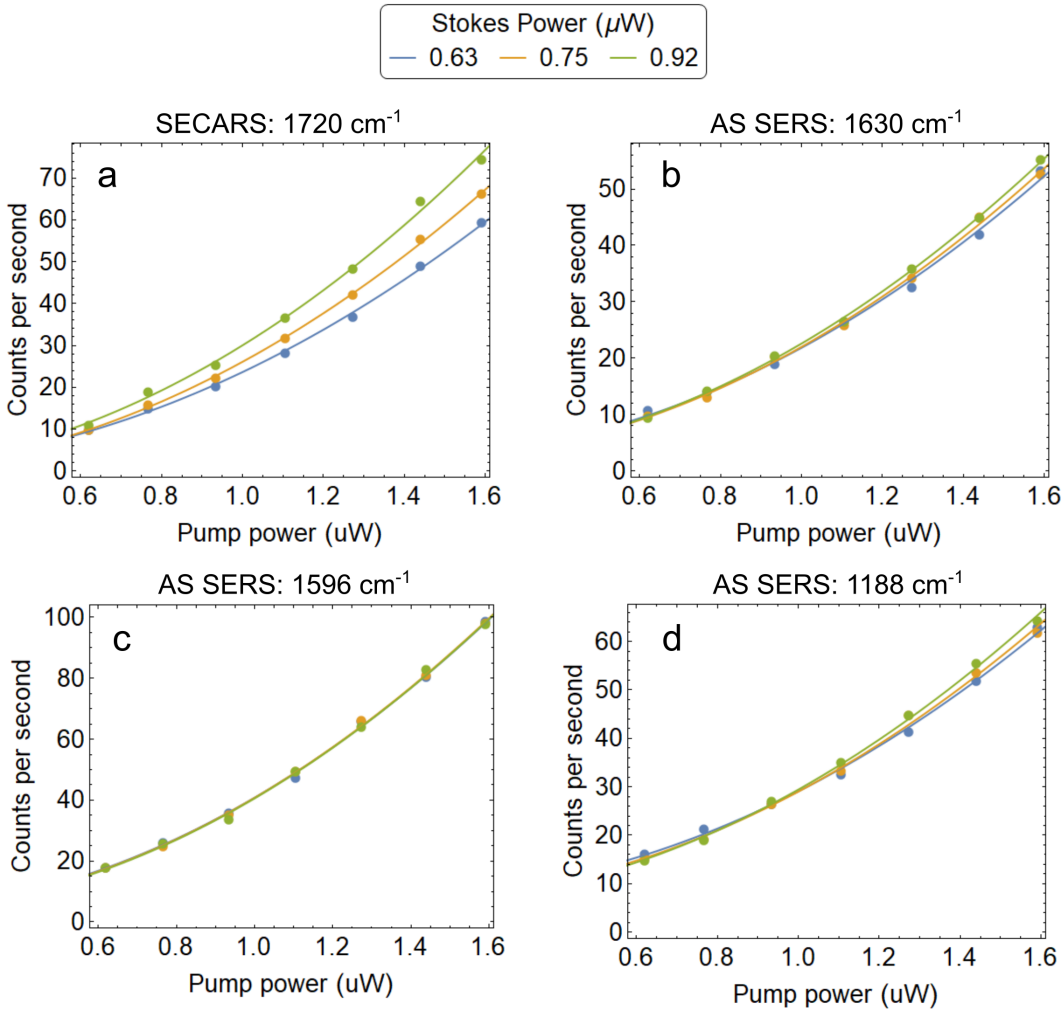

Figure 3.22: Power dependence curves for the simultaneously detected detuned SECARS and AS SERS signal. a) The curvature in the SECARS curves shows a dependence on the Stokes powers, which we expect due to the signal being proportional to the Stokes intensity. b-d) The AS SERS for the labeled resonances. As partially expected, the curvature is independent from the Stokes power. This says the AS SERS scattering rates are not enhanced do to laser heating from the 1030 nm laser beam.

Table 3.8: Second-order coefficients from the quadratic fitting results. The coefficients from the scaled on-resonant SECARS curves shows a clear increase due to SECARS proportionality to input Stokes power. The coefficients for the AS SERS does not show appreciable dependence on the Stokes laser power. Any differences are likely due to uncertainties in the measurement and a lack of significant dynamic range in the pump power values.

Stokes power (μW)	γ_{CARS} (cm^6s^2) 1645 cm^{-1}	γ_{AS} (cm^6s^2) 1630 cm^{-1}	γ_{CARS} (cm^6s^2) 1609 cm^{-1}	γ_{AS} (cm^6s^2) 1596 cm^{-1}
0.63	308 ± 14	19.5 ± 1.5	331 ± 15	37.5 ± 1.7
0.75	353 ± 12	20.3 ± 1.1	380 ± 13	37.8 ± 1.4
0.92	401 ± 27	21.0 ± 0.6	431 ± 29	37.8 ± 1.8

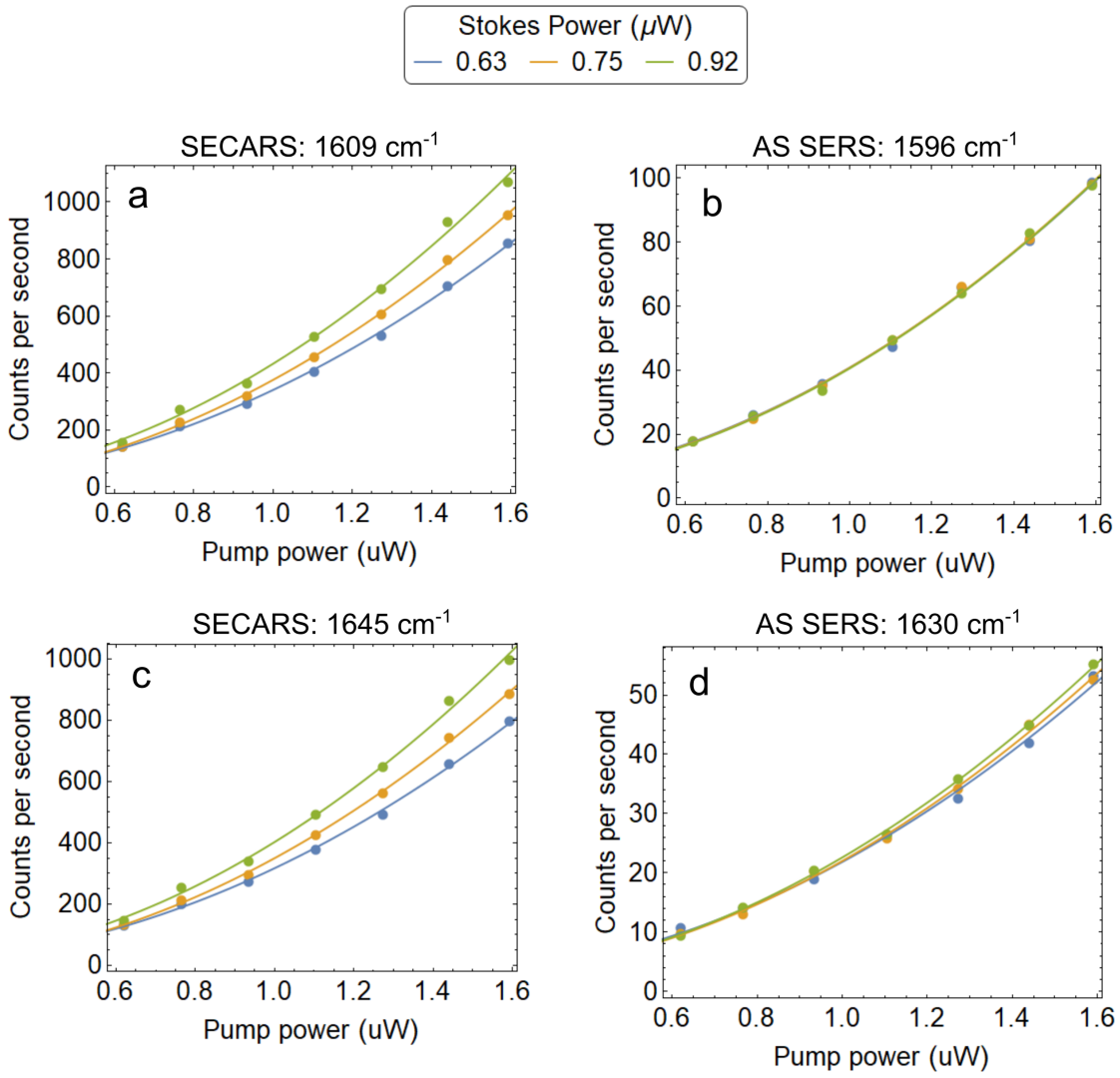

Figure 3.23: Power dependence curves for the on resonant SECARS and the associated AS SERS signal. a) and c) The curvature in the SECARS curves shows a dependence on the Stokes powers, which we expect due to the signal being proportional to the Stokes intensity. b) and d) The AS SERS for the labeled resonances. As partially expected, the curvature is independent from the Stokes power. This suggests the AS SERS scattering count rates are not enhanced do to laser heating from the 1030 nm laser beam. Therefore, the curvature in the AS SERS results is due to an optical pumping process (i.e. single-beam SECARS).

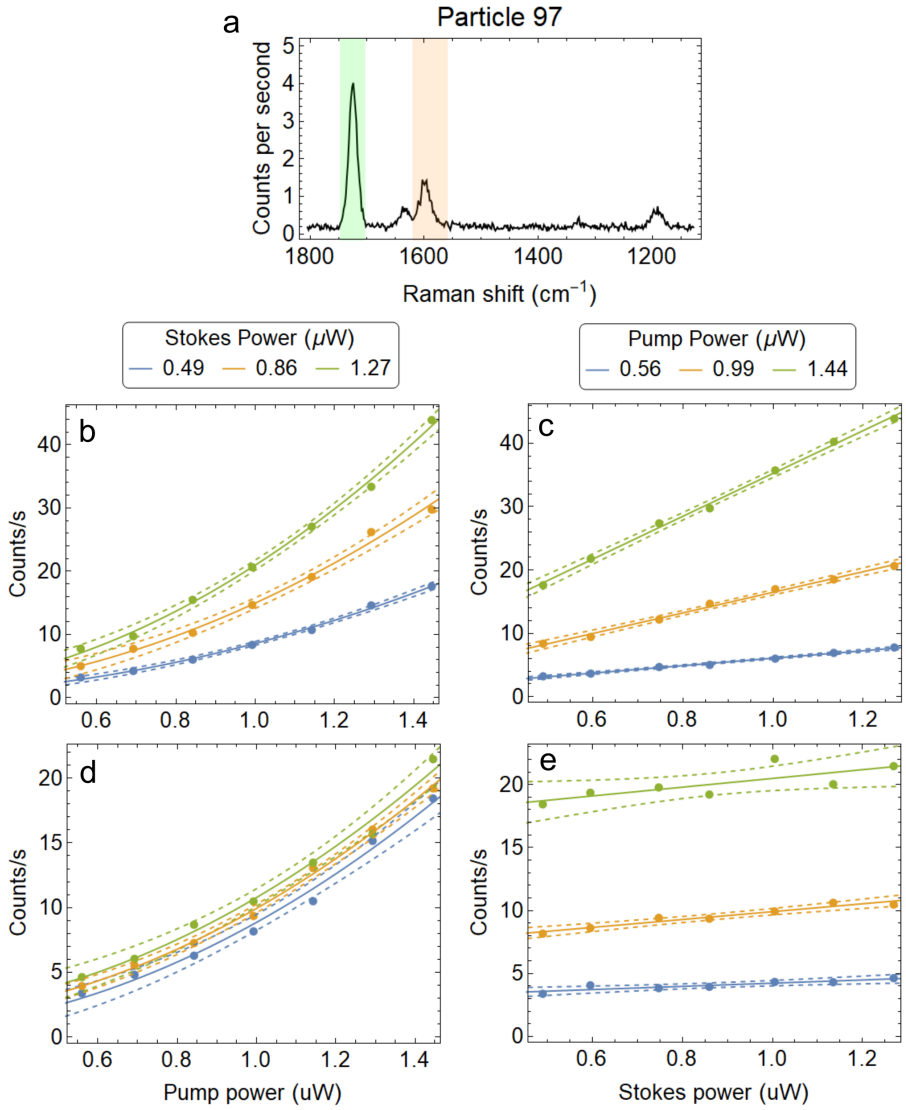

Figure 3.24: Simultaneous detuned SECARS and AS SERS power dependence curves comparison a) Anti-Stokes spectrum observed when illuminating a nantenna with both pump and Stokes beams. The green and orange shaded region correspond with the detuned SECARS and AS SERS, respectively. b-c) Detuned SECARS and d-e) AS SERS power dependence curves. The data points are obtained by integrating the shaded regions in a) for each of the power combinations, while the curves are the best fit using either a quadratic and or linear polynomial. A relatively large dependence on the Stokes power is observed in the SECARS results, as expected. A small dependence on the Stokes power is also observed in the AS SERS measurements.

3.8 Pulse characterization using time-correlation

CARS allows time-domain measurements of the prepared and interrogated coherences, by delaying the arrival time between pump, Stokes, and probe pulses. The vibrational coherence times at plasmonic junctions are on the order of picoseconds, therefore when using ps pulsed lasers, it is important to have accurately measured pulse durations and to establish the instrument response function.

Using optical autocorrelation to measure temporal profiles of optical pulses is well-established [80, 81]. A brief description of the common method follows, which relies on nonlinear process known as second-harmonic generation (SHG). The input pulsed beam is split into two paths using a beamsplitter and one of the beams placed on a path with an oscillating time-delay stage, effectively scanning one of the beams in time. The two beams are then focused onto a SHG crystal, noncollinearly, generating a new beam at twice the input frequency which is detected using a photomultiplier tube (PMT). Due to wave vector matching, the SHG signal has a unique propogation direction; therefore, it is unnecessary to filter the SHG from the input pulse. The resulting signal is a time-convolution of the two laser beams, also known as an autocorrelation function (ACF) trace. The trace is fit to a Gaussian and the resulting linewidth is multiplied by 0.707 to extract the pulse duration of the incident laser. The complete process is described as noncollinear intensity autocorrelation, which can be mathematically described.

The SHG signal, $I_{\mathrm{SHG}}(\tau)$, is second-order in the incident light intensity; therefore, with two pulses, one time delayed, the signal can be described by the second-order correlation function [80],

$$I_{\mathrm{SHG}}(\tau) = \int_{-\infty}^{\infty} \left| \left[\boldsymbol{E}(t) + \boldsymbol{E}(t-\tau) \right]^2 \right|^2 dt \tag{3.21}$$

where

$$\begin{aligned} \boldsymbol{E}(t) &= \varepsilon(t)\exp[i(\omega t + \Phi(t))] \\ \boldsymbol{E}(t-\tau) &= \varepsilon(t-\tau)\exp[i(\omega(t-\tau) + \Phi(t-\tau))] \end{aligned} \tag{3.22}$$

After performing the expansion and dropping the oscillatory terms, we obtain

$$I_{\mathrm{SHG}}(\tau) = \int_{-\infty}^{\infty} \left[2I^2(t) + 4I(t)I(t-\tau)\right] dt \tag{3.23}$$

where $I(t) = E^2(t)$. The oscillatory terms are dropped because the measurement scheme is too slow to measure the high frequency oscillatory terms, resulting in intensity autocorrelation and the averaging out of the phase components. The first term on the right-hand side of Equation 3.23 is a constant that does not affect the measured pulse duration; therefore, the pulse duration measured using intensity autocorrelation is given by,

$$I_{\mathrm{SHG}}(\tau) = \int_{-\infty}^{\infty} I(t)I(t-\tau)dt \tag{3.24}$$

where the factor of 4 has been dropped because it is an amplitude scaling factor that does not alter the pulse duration. As previously mentioned, the SHG must have an infinitely fast time response to use Equation 3.24. If the SHG signal is long lived, a model incorporating the lifetime would be necessary. This fact is mentioned here because the logic will be used for the time-domain SECARS response. Using a commercial autocorrelator with an oscillating delay stage, the pulse duration of the laser is measured for the pump and Stokes beams. The measured FWHM given by the autocorrelator is the time-delay difference between the 50% intensity points and is reported in Table 3.9. Lastly, the resulting FWHM is multiplied by a constant to retrieve the pulse duration of the laser (i.e. 0.707 for Gaussian or 0.647 for Sech^2-shaped pulses).

Table 3.9: FWHM for the ACF trace and the resulting pulse durations assuming a Gaussian or $Sech^2$-shaped laser pulse.

Beam	ACF (FWHM)	Gaussian	$Sech^2$
Pump (884 nm)	2.48 ps	1.75 ps	1.60 ps
Stokes (1031 nm)	3.36 ps	2.38 ps	2.17 ps

3.9 Time-domain SECARS

A Raman process is off-resonant when the input laser frequencies are detuned far from the electronic resonance of the molecule. This is the case for our spontaneous and coherent Raman experiments; therefore, the time-dependent CARS signal is calculated using Equation [82],

$$S_{\mathrm{CARS}}(\tau) = \left| \int_{-\infty}^{\infty} dt E_3(t) \int_{0}^{\infty} dt_2 E_2^* \left(t+\tau-t_2\right) E_1 \left(t+\tau-t_2\right) \exp\left[-t_2/\tau_v\right] \right|^2 \tag{3.25}$$

where the exponential term describes the response of the material (i.e. coherence time) and E_1, E_2, and E_3 are the envelope functions (Gaussians) representing the pump, Stokes, and probe pulses, respectively. Lasers with ps pulsed durations are not narrow enough in time to resolve the oscillatory molecular coherence; therefore, we can use a decaying exponential to describe the material response. Using ps lasers to measure a time-domain CARS process is analogous to measuring a high frequency signal using a circuit with a relatively large RC time; meaning, we can only detect relatively low frequency components. In this case, we can only hope to measure a signal which decays exponentially over time. The time constant τ_v is defined as the time taken for the excited population to reach $1/e$ of its initial value [63].

Figure 3.25 gives CARS simulation results for off molecular resonance (3.25a) and resonant using molecular lifetimes of 300, 500, and 1000 fs (3.25b-d). The blue data points are the simulated results and the red curve is the best fit using a Gaussian distribution. From the

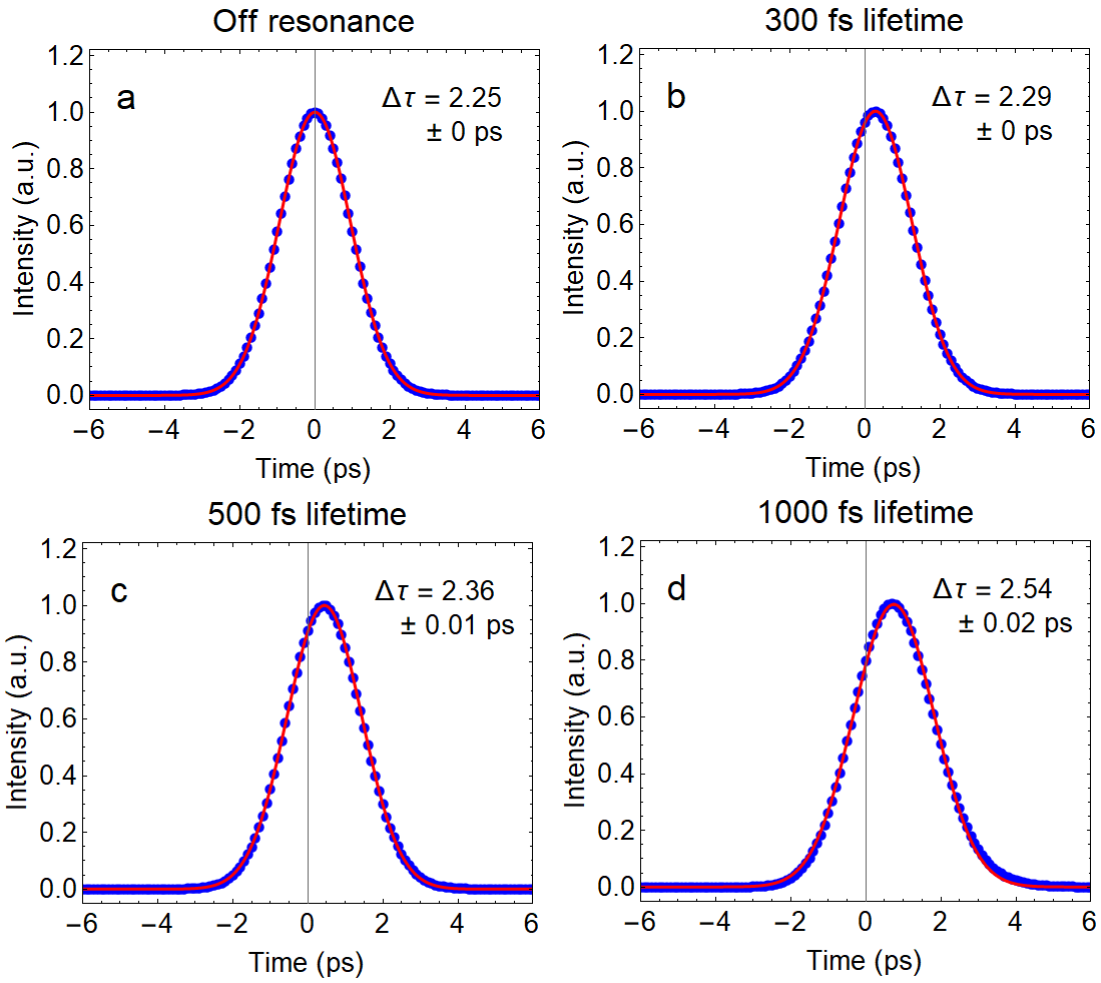

Figure 3.25: Simulating the CARS time-response using Equation 3.25 to model the experimental results. The blue data points are the simulated results and the red curve is the best fit using a Gaussian distribution. Time-domain results are shown for detuned (a) and resonant CARS with lifetimes of 300 fs (b), 500 fs (c), and 1000 fs (d). The FWHM ($\Delta\tau$) from the Gaussian fit is given for each case.

simulation results, we see time information can manifest in two ways. First, the FWHM for the best fit broadens as the molecular lifetime is made greater. Second, the mean for the Gaussian fit shifts to greater time values as the molecular lifetime is made greater. In this work, we use the broadened FWHM from our experimental curves to suggest the measured molecular lifetime.

Table 3.10 gives fitted FWHM values for the CARS simulations using Gaussian distributions. When using the experimental pulse widths determined using SHG autocorrelation (Table

Table 3.10: FWHM ($\Delta\tau$) values for the resonant (300, 500, and 1000 fs) and detuned (0 fs) simulated time-domain CARS sweeps. A lifetime of 0 fs is used for the detuned simulation because there is no molecule present to yield a coherence lifetime.

Lifetime (fs)	FWHM ($\Delta\tau$)	Relative difference
0	2.25 ps	—
300	2.29 ps	1.8 %
500	2.36 ps	4.9 %
1000	2.54 ps	13 %

3.9), we find the simulated detuned line-width is 2.25 ps. The third column gives the relative difference between the on and off resonance FWHM. This operation is performed because the experimental off resonance linewidth differs slightly from the simulated case. By using relative differences, simulated and experimental results can be compared to better approximate the molecular lifetimes observed in our measurements. For example, we see relative differences of 1.8 and 4.4% for simulated lifetimes of 300 and 500 fs, respectively. In the following section, the experimental relative differences will be presented, and lifetimes will be inferred. By comparing the results for the simulation and experiment, we can determine an approximate range of decay times for the molecular resonance being probed (i.e. 1615 cm^{-1}).

In Figure 3.26 we show 2D plots of SECARS spectra as a function of pump-probe delay, which can be regarded as frequency-resolved optical gating (FROG), and we will refer to them as such. The time sweeps are performed using a double pass technique, where the probe beam is first swept forward in time and then is immediately swept backwards in time. The top and bottom rows show the forward and reverse scans, respectively. Resonant double pass time scans have been performed on five nantennas, and off resonance scans have been collected for three of the five nantennas. From the FROG images, we observe a broadening in the time-domain resonant trace. When observing the FROG traces, we see a small chirp, namely, a skew in the image plot, Figures 3.26 and **??**a, b. A skew in the resonant FROG trace may imply broadening of the time response due to the finite lifetime of the vibrational coherence, while a skew in the detuned FROG is indicative of chirp in the laser pulses.

Table 3.11: FWHM ($\Delta\tau$) values for experimental resonant and detuned time-domain CARS sweeps. The values given are average values for the forward and reverse directions.

Particle	Resonant	Detuned	Relative difference
28	2.27 ± 0.13 ps	2.19 ± 0.15 ps	3.7 %
29	2.32 ± 0.13 ps	—	—
30	2.29 ± 0.14 ps	2.17 ± 0.26 ps	5.5 %
31	2.33 ± 0.19 ps	—	—
32	2.18 ± 0.15 ps	2.18 ± 0.13 ps	0.0 %

Before addressing the skew in the image plot, we project the FROG traces along the time axis, by integrating along the frequency axis. The projected data and their Gaussian fits are shown in Fig. 3.27. The FWHM of the Gaussian fits, averaged over forward and reverse scans is collected in Table 3.11. The differences in resonant versus detuned time-widths obtained by this method are within the error of the fits. The fitted time domain line-widths carry a significant uncertainty, but it is an initial result to suggest that the coherence time for BPE can be observed using ps lasers. In the following, we report additional evidence to verify the claim.

To see if there is a clear and significant difference in the skew for resonant and detuned image plots, we fit the SECARS signal to a Gaussian for each slice in time. To better depict the processing utilized to quantify the chirp, we provide Figure 3.28. We show a FROG trace with dashed, white lines to represent slices in time, Figure 3.28a. The 2-D profiles are then plotted to highlight the curves that are fitted to a Gaussian line-shape to retrieve the mean AS frequency, Figure 3.28b. The result after fitting each time slice to a Gaussian is given in Figures 3.29a and 3.29b, where we have also overlayed the detuned SECARS (blue) with the resonant (red) SECARS results. When observing the graphs, we see the signal frequency for both the resonant and detuned SECARS decreases linearly with time, also known as linear down-chirp. For there to be a linear chirp, the electric field for the Gaussian pulse will have the form [80],

$$E_y = \mathrm{Re}\left(E_0 \exp\left[-\Gamma t^2 + i\left(\omega_0 t - a t^2\right)\right]\right) \tag{3.26}$$

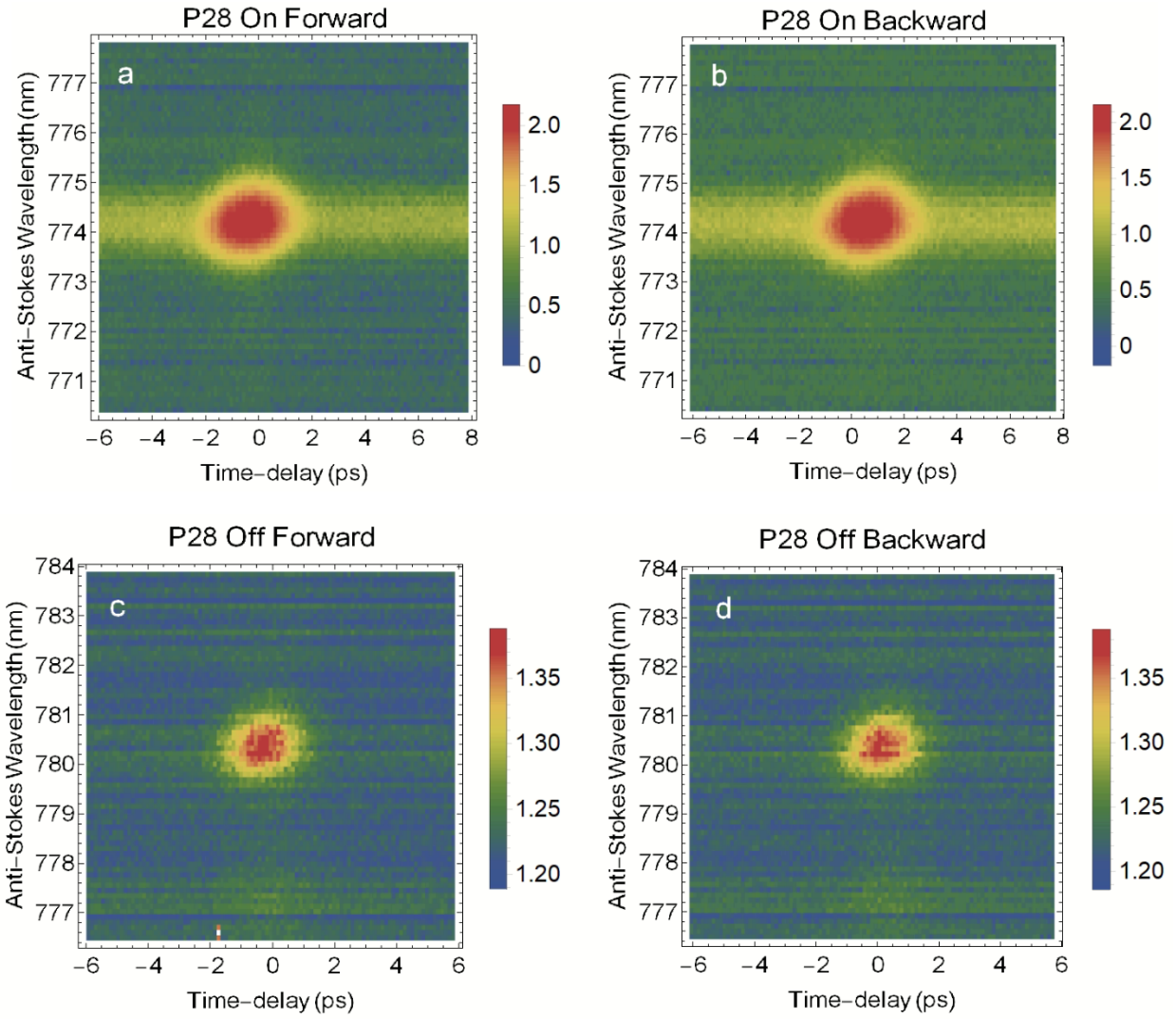

Figure 3.26: FROG traces for resonant (a, b) and detuned (c, d) SECARS time sweeps. Spectra are collected when sweeping forward (a, c) and backward (b, d) in time. The intensity is on a logarithmic scale to emphasize the tails.

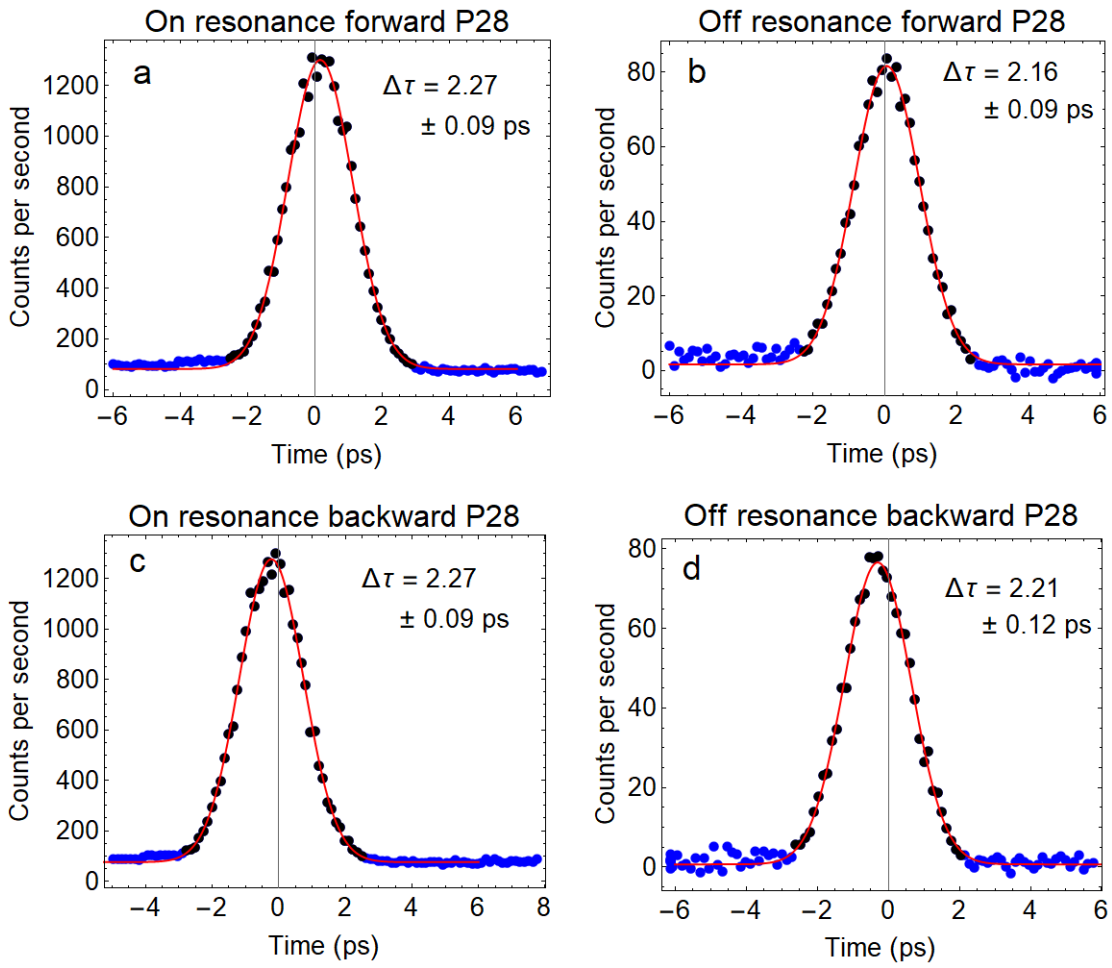

Figure 3.27: Experimental 2-D SECARS time-domain results. The FWHM ($\Delta\tau$) from the Gaussian fit is given for each case. There is a small, but measurable, difference between the resonant (a, c) and detuned (b, d) curves

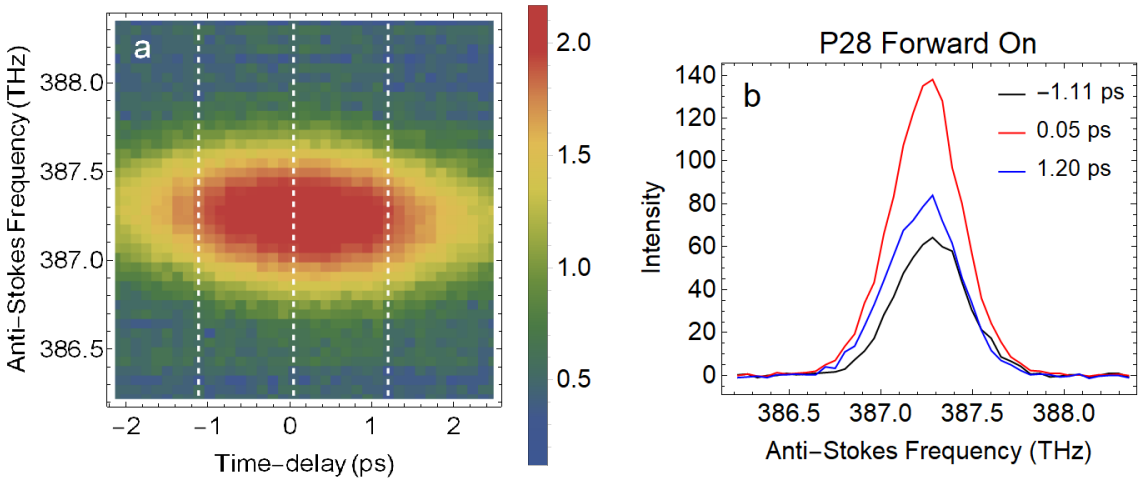

Figure 3.28: A magnified resonant SECARS FROG trace on a logarithmic scale with dashed, vertical white lines signifying slices in time (a). The slices in time are then plotted to show how then can be fitted accurately to a Gaussian to retrieve the mean frequency (b). The mean frequencies can then be plotted versus time to see the material dependent chirp it the ps pulse.

where the traveling pulse is quadratic in time. The instantaneous angular frequency becomes,

$$\omega = \partial\Phi/\partial t = \omega_0 + \alpha t \tag{3.27}$$

where $\alpha = -2a$ and $\alpha > 0$. When $\alpha > 0$, the instantaneous frequency is redder in the leading part of the pulse and bluer in the trailing part. When first observing the results, it looks like the linear down-chirp is equivalent for the resonant and detuned results, but when the data is fit to a line, a clear difference between the two is observed, Figure 3.29c, d. This observation is consistent across all measured nantennas, Table 3.12.

The results tell us that the decrease in the magnitude of the slope for resonant SECARS time sweeps is due to the molecule up-chirping the AS photons with respect to the detuned SECARS time sweeps. The electronic response (i.e. polarizability) of a material will induce a chirp in the laser beam, and the lifetime for the material response likely affects the amount of chirp. When detuned, any chirp in the AS signal is either due to the inherent chirp in the ps laser sources, or is a combination of the inherent chirp with the response of the plasmon.

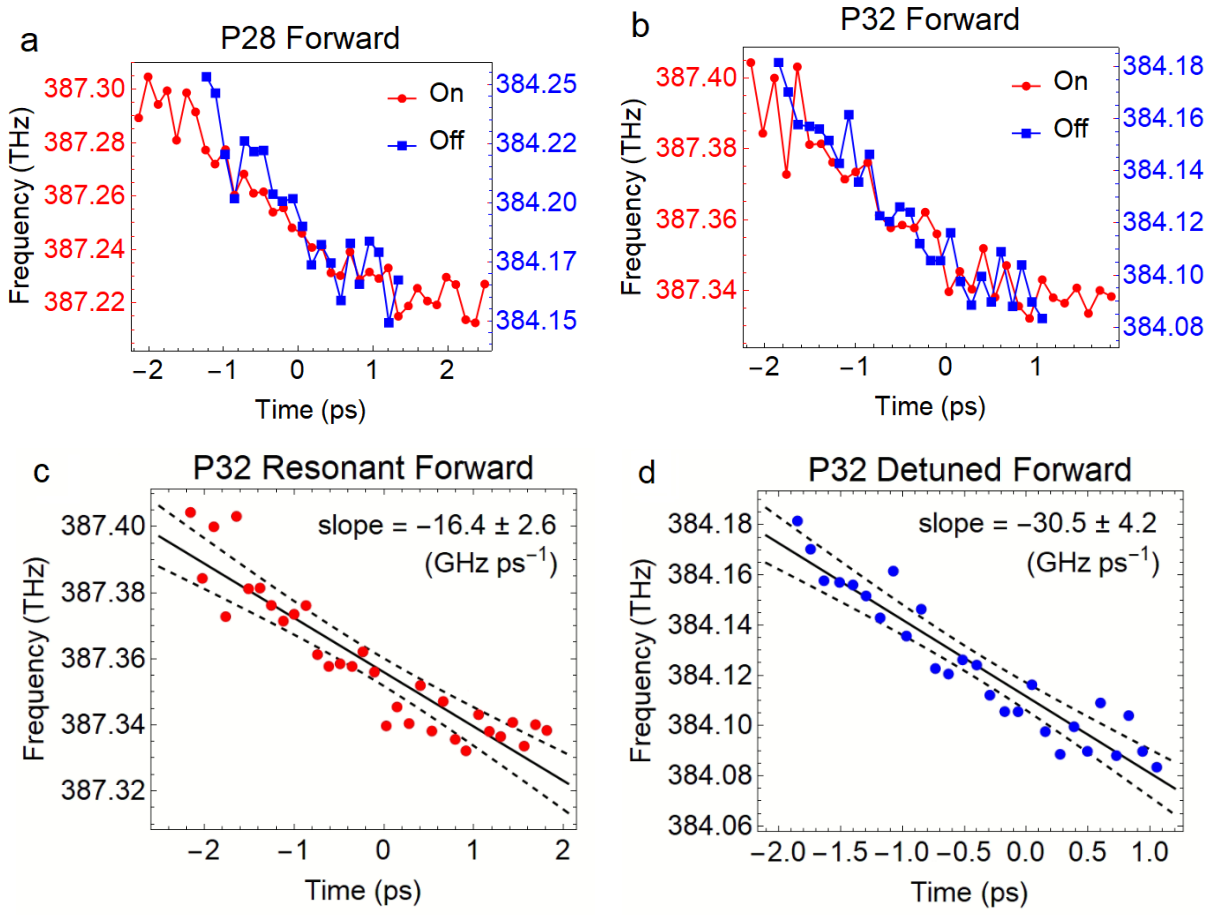

Figure 3.29: Overlayed line-plots showing the linear down-chirp in the SECARS time sweeps for two distinct nantennas (a, b). We plot the resonant (red) and detuned (blue) curves to show the presence of linear chirp for both measurements. The data points are then fitted to a line to show the unique slopes for the resonant and detuned curves (c, d). We see a clear and consistent increase in magnitude for the slope when detuned from the resonance.

Table 3.12: Fitted slope parameters for the measured linear down-chirp in the SECARS time sweeps. There is a clear and consistent increase in the magnitude of the slope for the detuned results. The values given are average values for the forward and reverse sweeps, and the reported error is the 95% confidence interval. The reported uncertainty is the root-mean-square of the individual forward and reverse sweep uncertainties.

Particle	Resonant (GHz ps^{-1})	Detuned (GHz ps^{-1})
28	-18.5 ± 4.1	-32.3 ± 14.9
29	-21.3 ± 4.3	—
30	-24.6 ± 5.2	-31.8 ± 13.6
31	-20.0 ± 3.7	—
32	-17.3 ± 3.8	-29.1 ± 7.7

The plasmon has a lifetime (∼15 fs) that is much shorter than the ps pulse duration (∼2 ps); therefore, the down-chirp we see when we are detuned is likely inherent in the ps source. When we tune the lasers to be on resonant, we see an up-chirp in the AS photons with respect to the detuned results. This tells us that we are detecting the molecular coherence time of BPE. This is additional evidence that goes with our 1-D fits using Gaussians to suggest that we are detecting the low-frequency component of the molecular coherence.

Now that we have presented the linear chirp in the SECARS results, we can examine the line-widths obtained from the Gaussian fits. Instead of plotting the center frequency obtained from the fits, we plot the obtained line-widths versus time delay, Figure 3.30. From the curves, we see a clear and reproducible compression in the line-width when resonant with the molecular vibration. From the time-bandwidth product, a compression in frequency accompanies an expansion in time. This is additional evidence demonstrating the coherence lifetime detection when probing BPE with ps laser sources. The results displayed in Figure 3.30 is representative for all the nantennas measured during these studies. From both displayed and non-displayed curves, there is no clear evidence to suggest a time dependence for the SECARS line-width.

We have shown that when our ps laser beams interact with the BPE molecule, we see both an up-chirp in the CARS temporal pulse and a narrowing in the frequency line-width. For the CARS pulse to up-chip temporally, the BPE broadened the pulse in time due to positive group velocity dispersion (GVD > 0) [80]. Interaction with BPE causes red components of the CARS pulse spectrum to travel faster than the blue components. Interaction with BPE causes the CARS pulse to up-chirp, which would typically cause the ultrafast laser pulse to become closer to transform limited [83]. This means the laser pulse should actually compress in time with respect to the detuned CARS pulse. This suggests to us that the BPE is working overtime to produce a time response in the SECARS temporal signal. The fact

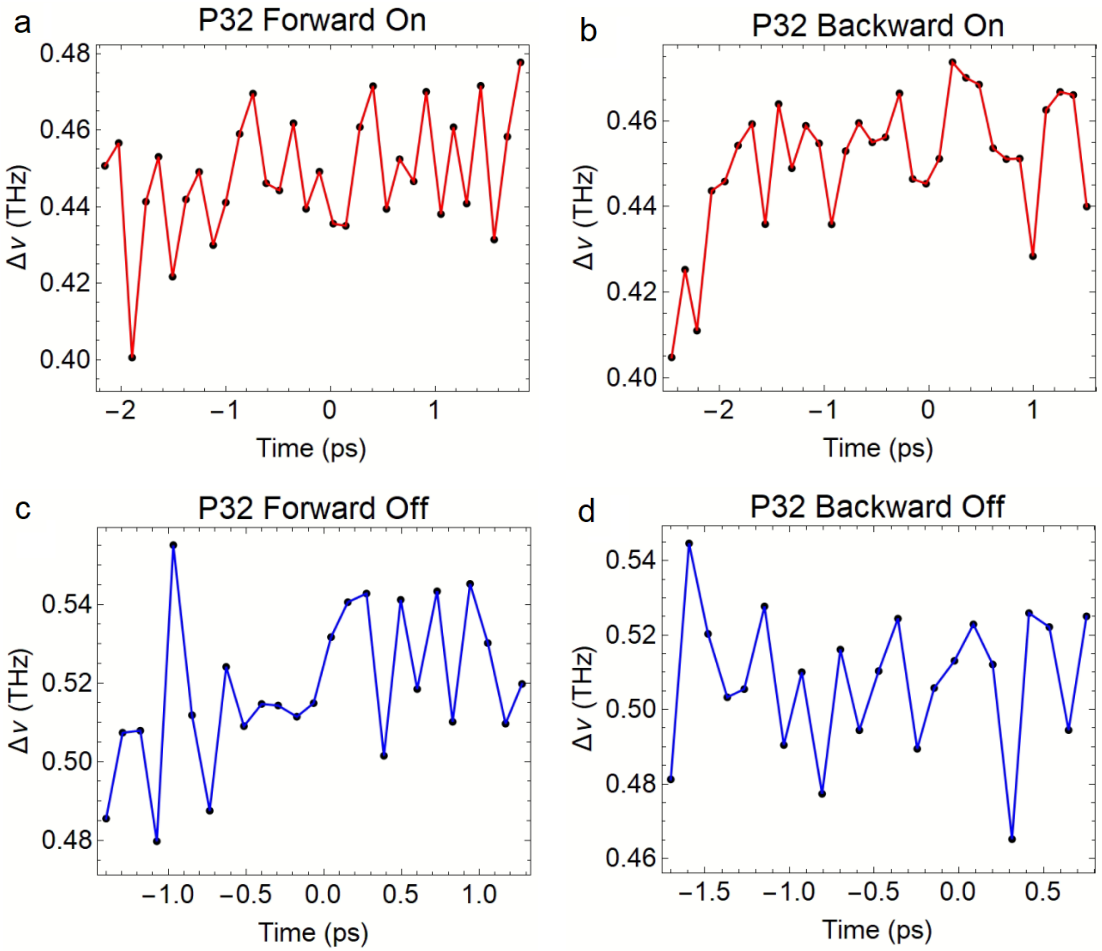

Figure 3.30: Measured SECARS line-width versus time delay when resonant (a, b) and detuned (c, d). Line-width values are obtained by fitting Y-slices from the FROG traces to a Gaussian. We see a clear line-width compression when resonant with the molecular vibration. From the time-bandwidth product, a compression in frequency accompanies an expansion in time. Further evidence to suggest a detectable BPE CARS coherence time.

that we are seeing a temporal broadening in the CARS pulse and not a temporal compression, is additional evidence to suggest a detected BPE time response.

Bibliography

[1] Na Liu, Ming L Tang, Mario Hentschel, Harald Giessen, and A Paul Alivisatos. Nanoantenna-enhanced gas sensing in a single tailored nanofocus. *Nature Materials*, 10 (8):631, 2011.

[2] Peter Muehlschlegel, H-J Eisler, Olivier JF Martin, B Hecht, and DW Pohl. Resonant optical antennas. *Science*, 308(5728):1607–1609, 2005.

[3] Laura Rodríguez-Lorenzo, Roberto de La Rica, Ramón A Álvarez-Puebla, Luis M Liz-Marzán, and Molly M Stevens. Plasmonic nanosensors with inverse sensitivity by means of enzyme-guided crystal growth. *Nature Materials*, 11(7):604, 2012.

[4] Seulki Lee, Eui-Joon Cha, Kyeongsoon Park, Seung-Young Lee, Jin-Ki Hong, In-Cheol Sun, Sang Yoon Kim, Kuiwon Choi, Ick Chan Kwon, Kwangmeyung Kim, et al. A near-infrared-fluorescence-quenched gold-nanoparticle imaging probe for in vivo drug screening and protease activity determination. *Angewandte Chemie International Edition*, 47(15):2804–2807, 2008.

[5] Stefan Alexander Maier. *Plasmonics: Fundamentals and Applications*. Springer Science & Business Media, 2007.

[6] Lukas Novotny and Niek Van Hulst. Antennas for light. *Nature Photonics*, 5(2):83, 2011.

[7] Nathan C Lindquist, Prashant Nagpal, Kevin M McPeak, David J Norris, and Sang-Hyun Oh. Engineering metallic nanostructures for plasmonics and nanophotonics. *Reports on Progress in Physics*, 75(3):036501, 2012.

[8] Wenshan Cai, Uday K Chettiar, Alexander V Kildishev, and Vladimir M Shalaev. Optical cloaking with metamaterials. *Nature Photonics*, 1(4):224, 2007.

[9] David R Smith, John B Pendry, and Mike CK Wiltshire. Metamaterials and negative refractive index. *Science*, 305(5685):788–792, 2004.

[10] Richard Osgood, Joel B Carlson, Brian R Kimball, David P Ziegler, James R Welch, Lauren E Belton, Gustavo E Fernandes, Zhijun Liu, and Jimmy Xu. Plasmonic nanorectennas for energy conversion. In *Plasmonics: Metallic Nanostructures and Their Optical Properties VII*, volume 7394, page 73941L. International Society for Optics and Photonics, 2009.

[11] T Junno, K Deppert, L Montelius, and L Samuelson. Controlled manipulation of nanoparticles with an atomic force microscope. *Applied Physics Letters*, 66(26):3627–3629, 1995.

[12] Farbod Shafiei, Francesco Monticone, Khai Q Le, Xing-Xiang Liu, Thomas Hartsfield, Andrea Alù, and Xiaoqin Li. A subwavelength plasmonic metamolecule exhibiting magnetic-based optical fano resonance. *Nature Nanotechnology*, 8(2):95, 2013.

[13] Hideki Miyazaki and Tomomasa Sato. Mechanical assembly of three-dimensional microstructures from fine particles. *Advanced Robotics*, 11(2):169–185, 1996.

[14] MinFeng Yu, Mark J Dyer, George D Skidmore, Henry W Rohrs, XueKun Lu, Kevin D Ausman, James R Von Ehr, and Rodney S Ruoff. Three-dimensional manipulation of carbon nanotubes under a scanning electron microscope. *Nanotechnology*, 10(3):244, 1999.

[15] Yong Lin, Qiming Li, Andrew Armstrong, and George T Wang. In situ scanning electron microscope electrical characterization of gan nanowire nanodiodes using tungsten and tungsten/gallium nanoprobes. *Solid State Communications*, 149(39-40):1608–1610, 2009.

[16] Kai Arstila, Thomas Hantschel, Andreas Schulze, Anne Vandooren, AS Verhulst, Rita Rooyackers, Pierre Eyben, and Wilfried Vandervorst. Nanoprober-based ebic measurements for nanowire transistor structures. *Microelectronic Engineering*, 105:99–102, 2013.

[17] Stephen S Sasaki, Shawn M Perdue, Alejandro Rodriguez Perez, Nicholas Tallarida, Julia H Majors, V Ara Apkarian, and Joonhee Lee. Note: Automated electrochemical etching and polishing of silver scanning tunneling microscope tips. *Review of Scientific Instruments*, 84(9):096109, 2013.

[18] Fritz London. The general theory of molecular forces. *Transactions of the Faraday Society*, 33:8b–26, 1937.

[19] Hugo C Hamaker. The london—van der waals attraction between spherical particles. *physica*, 4(10):1058–1072, 1937.

[20] AD McLachlan. Effect of the medium on dispersion forces in liquids. *Discussions of the Faraday Society*, 40:239–245, 1965.

[21] Jacob N Israelachvili. *Intermolecular and surface forces*. Academic press, 2011.

[22] V Adrian Parsegian. *Van der Waals forces: a handbook for biologists, chemists, engineers, and physicists*. Cambridge University Press, 2005.

[23] V Adrian Parsegian and George H Weiss. Spectroscopic parameters for computation of van der waals forces. *Journal of Colloid and Interface Science*, 81(1):285–289, 1981.

[24] Wolfgang SM Werner, Kathrin Glantschnig, and Claudia Ambrosch-Draxl. Optical constants and inelastic electron-scattering data for 17 elemental metals. *Journal of Physical and Chemical Reference Data*, 38(4):1013–1092, 2009.

[25] Tobias AF Konig, Petr A Ledin, Justin Kerszulis, Mahmoud A Mahmoud, Mostafa A El-Sayed, John R Reynolds, and Vladimir V Tsukruk. Electrically tunable plasmonic behavior of nanocube–polymer nanomaterials induced by a redox-active electrochromic polymer. *ACS nano*, 8(6):6182–6192, 2014.

[26] Mansour S Farhan, Erfan Zalnezhad, Abdul Razak Bushroa, and Ahmed Aly Diaa Sarhan. Electrical and optical properties of indium-tin oxide (ito) films by ion-assisted deposition (iad) at room temperature. *International Journal of Precision Engineering and Manufacturing*, 14(8):1465–1469, 2013.

[27] Enrico Clementi, DL Raimondi, and William P Reinhardt. Atomic screening constants from scf functions. ii. atoms with 37 to 86 electrons. *The Journal of Chemical Physics*, 47(4):1300–1307, 1967.

[28] Mayukh Banik, Kate Rodriguez, Eero Hulkko, and V Ara Apkarian. Orientation-dependent handedness of chiral plasmons on nanosphere dimers: How to turn a right hand into a left hand. *ACS Photonics*, 3(12):2482–2489, 2016.

[29] Steven Yampolsky, Dmitry A Fishman, Shirshendu Dey, Eero Hulkko, Mayukh Banik, Eric O Potma, and Vartkess A Apkarian. Seeing a single molecule vibrate through time-resolved coherent anti-stokes raman scattering. *Nature Photonics*, 8(8):650, 2014.

[30] Renee R Frontiera, Anne-Isabelle Henry, Natalie L Gruenke, and Richard P Van Duyne. Surface-enhanced femtosecond stimulated raman spectroscopy. *The journal of physical chemistry letters*, 2(10):1199–1203, 2011.

[31] IH Malitson. Interspecimen comparison of the refractive index of fused silica. *Josa*, 55 (10):1205–1209, 1965.

[32] ZA Weinberg, GW Rubloff, and E Bassous. Transmission, photoconductivity, and the experimental band gap of thermally grown si o 2 films. *Physical Review B*, 19(6):3107, 1979.

[33] Charles Kittel, Paul McEuen, and Paul McEuen. *Introduction to solid state physics*, volume 8. Wiley New York, 1996.

[34] Donald L Hildenbrand and Edmond Murad. Dissociation energy and ionization potential of silicon monoxide. *The Journal of Chemical Physics*, 51(2):807–811, 1969.

[35] Sheldon Schultz, David R Smith, Jack J Mock, and David A Schultz. Single-target molecule detection with nonbleaching multicolor optical immunolabels. *Proceedings of the National Academy of Sciences*, 97(3):996–1001, 2000.

[36] C Sönnichsen, S Geier, NE Hecker, G Von Plessen, J Feldmann, H Ditlbacher, B Lamprecht, JR Krenn, FR Aussenegg, V ZH Chan, et al. Spectroscopy of single metallic nanoparticles using total internal reflection microscopy. *Applied Physics Letters*, 77(19): 2949–2951, 2000.

[37] JJ Mock, M Barbic, DR Smith, DA Schultz, and S Schultz. Shape effects in plasmon resonance of individual colloidal silver nanoparticles. *The Journal of Chemical Physics*, 116(15):6755–6759, 2002.

[38] Emil Prodan, Corey Radloff, Naomi J Halas, and Peter Nordlander. A hybridization model for the plasmon response of complex nanostructures. *Science*, 302(5644):419–422, 2003.

[39] Peter Nordlander, C Oubre, E Prodan, K Li, and MI Stockman. Plasmon hybridization in nanoparticle dimers. *Nano Letters*, 4(5):899–903, 2004.

[40] Naomi J Halas, Surbhi Lal, Wei-Shun Chang, Stephan Link, and Peter Nordlander. Plasmons in strongly coupled metallic nanostructures. *Chemical Reviews*, 111(6):3913–3961, 2011.

[41] Prashant K Jain, Wenyu Huang, and Mostafa A El-Sayed. On the universal scaling behavior of the distance decay of plasmon coupling in metal nanoparticle pairs: a plasmon ruler equation. *Nano Letters*, 7(7):2080–2088, 2007.

[42] Martin Fleischmann, Patrick J Hendra, and A James McQuillan. Raman spectra of pyridine adsorbed at a silver electrode. *Chemical physics letters*, 26(2):163–166, 1974.

[43] David L Jeanmaire and Richard P Van Duyne. Surface raman spectroelectrochemistry: Part i. heterocyclic, aromatic, and aliphatic amines adsorbed on the anodized silver electrode. *Journal of electroanalytical chemistry and interfacial electrochemistry*, 84(1): 1–20, 1977.

[44] M Grant Albrecht and J Alan Creighton. Anomalously intense raman spectra of pyridine at a silver electrode. *Journal of the american chemical society*, 99(15):5215–5217, 1977.

[45] Katrin Kneipp, Yang Wang, Harald Kneipp, Lev T Perelman, Irving Itzkan, Ramachandra R Dasari, and Michael S Feld. Single molecule detection using surface-enhanced raman scattering (sers). *Physical review letters*, 78(9):1667, 1997.

[46] Katrin Kneipp, Harald Kneipp, Geurt Deinum, Irving Itzkan, Ramachandra R Dasari, and Michael S Feld. Single-molecule detection of a cyanine dye in silver colloidal solution using near-infrared surface-enhanced raman scattering. *Applied spectroscopy*, 52(2): 175–178, 1998.

[47] Katrin Kneipp, Harald Kneipp, V Bhaskaran Kartha, Ramasamy Manoharan, Geurt Deinum, Irving Itzkan, Ramachandra R Dasari, and Michael S Feld. Detection and identification of a single dna base molecule using surface-enhanced raman scattering (sers). *Physical Review E*, 57(6):R6281, 1998.

[48] Kevin T Crampton, Alexander Fast, Eric O Potma, and V Ara Apkarian. Junction plasmon driven population inversion of molecular vibrations: a picosecond surface-enhanced raman spectroscopy study. *Nano letters*, 18(9):5791–5796, 2018.

[49] Felix Benz, Mikolaj K Schmidt, Alexander Dreismann, Rohit Chikkaraddy, Yao Zhang, Angela Demetriadou, Cloudy Carnegie, Hamid Ohadi, Bart De Nijs, Ruben Esteban, et al. Single-molecule optomechanics in "picocavities". *Science*, 354(6313):726–729, 2016.

[50] Katrin Kneipp, Yang Wang, Harald Kneipp, Irving Itzkan, Ramachandra R Dasari, and Michael S Feld. Population pumping of excited vibrational states by spontaneous surface-enhanced raman scattering. *Physical review letters*, 76(14):2444, 1996.

[51] RC Maher, LF Cohen, P Etchegoin, HJN Hartigan, RJC Brown, and MJT Milton. Stokes/anti-stokes anomalies under surface enhanced raman scattering conditions. *The Journal of chemical physics*, 120(24):11746–11753, 2004.

[52] RC Maher, LF Cohen, JC Gallop, EC Le Ru, and PG Etchegoin. Temperature-dependent anti-stokes/stokes ratios under surface-enhanced raman scattering conditions. *The Journal of Physical Chemistry B*, 110(13):6797–6803, 2006.

[53] RC Maher, PG Etchegoin, EC Le Ru, and LF Cohen. A conclusive demonstration of vibrational pumping under surface enhanced raman scattering conditions. *The Journal of Physical Chemistry B*, 110(24):11757–11760, 2006.

[54] TL Haslett, L Tay, and M Moskovits. Can surface-enhanced raman scattering serve as a channel for strong optical pumping? *The Journal of Chemical Physics*, 113(4): 1641–1646, 2000.

[55] Bert J Kip and Robert J Meier. Determination of the local temperature at a sample during raman experiments using stokes and anti-stokes raman bands. *Applied spectroscopy*, 44 (4):707–711, 1990.

[56] George C Schatz and Mark A Ratner. *Quantum mechanics in chemistry*. Courier Corporation, 2002.

[57] Richard L McCreery. *Raman spectroscopy for chemical analysis*, volume 225. John Wiley & Sons, 2005.

[58] Eric A Pozzi, Alyssa B Zrimsek, Clotilde M Lethiec, George C Schatz, Mark C Hersam, and Richard P Van Duyne. Evaluating single-molecule stokes and anti-stokes sers for nanoscale thermometry. *The Journal of Physical Chemistry C*, 119(36):21116–21124, 2015.

[59] RC Maher, J Hou, LF Cohen, EC Le Ru, JM Hadfield, JE Harvey, PG Etchegoin, FM Liu, M Green, RJC Brown, et al. Resonance contributions to anti-stokes/stokes ratios under surface enhanced raman scattering conditions. *The Journal of chemical physics*, 123(8):084702, 2005.

[60] Emily L Keller and Renee R Frontiera. Ultrafast nanoscale raman thermometry proves heating is not a primary mechanism for plasmon-driven photocatalysis. *ACS nano*, 12 (6):5848–5855, 2018.

[61] Mihaela Baibarac, Ioan Baltog, and Serge Lefrant. Abnormal anti-stokes raman emission as single beam coherent anti-stokes raman scattering like process in linbo3 and cds powder. *Journal of Applied Physics*, 110(5):053106, 2011.

[62] Derek Albert Long. The raman effect: a unified treatment of the theory of raman scattering by molecules. 2002.

[63] Paul L Houston. *Chemical kinetics and reaction dynamics*. Courier Corporation, 2012.

[64] Evan J Blackie, Eric C Le Ru, and Pablo G Etchegoin. Single-molecule surface-enhanced raman spectroscopy of nonresonant molecules. *Journal of the American Chemical Society*, 131(40):14466–14472, 2009.

[65] Joonhee Lee, Kevin T Crampton, Nicholas Tallarida, and V Ara Apkarian. Visualizing vibrational normal modes of a single molecule with atomically confined light. *Nature*, 568(7750):78–82, 2019.

[66] S Dey, M Banik, E Hulkko, K Rodriguez, VA Apkarian, M Galperin, and A Nitzan. Observation and analysis of fano-like lineshapes in the raman spectra of molecules adsorbed at metal interfaces. *Physical Review B*, 93(3):035411, 2016.

[67] James T Hugall and Jeremy J Baumberg. Demonstrating photoluminescence from au is electronic inelastic light scattering of a plasmonic metal: the origin of sers backgrounds. *Nano letters*, 15(4):2600–2604, 2015.

[68] RC Maher, LF Cohen, P Lohsoontorn, DJL Brett, and NP Brandon. Raman spectroscopy as a probe of temperature and oxidation state for gadolinium-doped ceria used in solid oxide fuel cells. *The Journal of Physical Chemistry A*, 112(7):1497–1501, 2008.

[69] TP Purdy, P-L Yu, NS Kampel, RW Peterson, K Cicak, RW Simmonds, and CA Regal. Optomechanical raman-ratio thermometry. *Physical Review A*, 92(3):031802, 2015.

[70] Taro Ichimura, Norihiko Hayazawa, Mamoru Hashimoto, Yasushi Inouye, and Satoshi Kawata. Local enhancement of coherent anti-stokes raman scattering by isolated gold nanoparticles. *Journal of Raman Spectroscopy*, 34(9):651–654, 2003.

[71] Taro Ichimura, Norihiko Hayazawa, Mamoru Hashimoto, Yasushi Inouye, and Satoshi Kawata. Tip-enhanced coherent anti-stokes raman scattering for vibrational nanoimaging. *Physical review letters*, 92(22):220801, 2004.

[72] Christian Steuwe, Clemens F Kaminski, Jeremy J Baumberg, and Sumeet Mahajan. Surface enhanced coherent anti-stokes raman scattering on nanostructured gold surfaces. *Nano letters*, 11(12):5339–5343, 2011.

[73] Yu Zhang, Yu-Rong Zhen, Oara Neumann, Jared K Day, Peter Nordlander, and Naomi J Halas. Coherent anti-stokes raman scattering with single-molecule sensitivity using a plasmonic fano resonance. *Nature communications*, 5(1):1–7, 2014.

[74] Tae-Woong Koo, Selena Chan, and Andrew A Berlin. Single-molecule detection of biomolecules by surface-enhanced coherent anti-stokes raman scattering. *Optics letters*, 30(9):1024–1026, 2005.

[75] Cheng Zong and Ji-Xin Cheng. Origin of dispersive line shapes in plasmon-enhanced stimulated raman scattering microscopy. *Nanophotonics*, 10(1):617–625, 2020.

[76] Xia Hua, Dmitri V Voronine, Charles W Ballmann, Alexander M Sinyukov, Alexei V Sokolov, and Marlan O Scully. Nature of surface-enhanced coherent raman scattering. *Physical Review A*, 89(4):043841, 2014.

[77] Arthur Dogariu, Alexander Goltsov, Hui Xia, and Marlan O Scully. Concentration dependence in coherent raman scattering. *Journal of Modern Optics*, 55(19-20):3255–3261, 2008.

[78] Lukas Novotny and Bert Hecht. *Principles of nano-optics*. Cambridge university press, 2012.

[79] Ying Fang, Nak-Hyun Seong, and Dana D Dlott. Measurement of the distribution of site enhancements in surface-enhanced raman scattering. *Science*, 321(5887):388–392, 2008.

[80] Claude Rulliere et al. *Femtosecond laser pulses*. Springer, 2005.

[81] Andrew Weiner. *Ultrafast optics*, volume 72. John Wiley & Sons, 2011.

[82] Shaul Mukamel. *Principles of nonlinear optical spectroscopy*, volume 6. Oxford university press New York, 1995.

[83] Rick Trebino. *Frequency-Resolved Optical Gating: The Measurement of Ultrashort Laser Pulses: The Measurement of Ultrashort Laser Pulses*. Springer Science & Business Media, 2000.